Incorporation of the effects of accelerating flow in the design of granular bed protections

MSc Thesis

Author: R.S. Steenstra
Institute: Delft University of Technology

Date: 12th March 2014

Incorporation of the effects of accelerating flow in the design of granular bed protections

Author:	Remco Stefan Steenstra
Phone number:	+316 33 92 97 98
E-mail address:	rssteenstra@gmail.com
Master:	Civil Engineering
Track:	Hydraulic Engineering
Specialisation:	Environmental Fluid Mechanics
Institute:	Delft University of Technology

Graduation committee

prof. dr. ir. W.S.J. Uijttewaal	Delft University of Technology
ir. J.P. van den Bos	Delft University of Technology / Boskalis
dr. ir. B. Hofland	Delft University of Technology / Deltares
dr. ir. A.J. Paarlberg	HKV Consultants
ir. A.J. Smale	Deltares

Preface

This reports contains the results of my graduation research as conclusion of the master Hydraulic Engineering at the faculty of Civil Engineering and Geosciences at the Delft University of Technology. The work for this research was done at the consulting company HKV Consultants and in cooperation with Deltares. The study began with the desire of HKV to gain more knowledge of the open source numerical software package OpenFOAM. A subject had to be found in which OpenFOAM was used as a modelling tool, but that also fulfilled the requirements set by the TU Delft. This means that a scientifically relevant practical civil engineering problem was investigated. Eventually this resulted to the topic researched in this thesis, which in my opinion combines the above mentioned criteria together with a variety of subjects that have been treated in the courses that I followed during my study.

During my research, i received help from a lot of people. I would like to thank my graduation committee, prof. dr. ir. W.S.J. Uijttewaal, dr. ir. A.J. Paarlberg, ir. A.J. Smale, dr. ir. B. Hofland and ir. J.P. van den Bos for the guidance they have given me during this research. The comments, advice and help I received while I was doing the research and writing of this report was very valuable to me. I am also grateful to any other person that could be of any help to me: Jos Vilier for introducing me at HKV, Freek Huthoff from HKV for the guidance, Niels Jacobsen for helping me with OpenFOAM, Manfred Jellesma for the fun times working together at HKV, my family for the support and finally my friends for the all good times and the necessary distraction from the hard work.

12th March 2014

Summary

Hydraulic structures like groins, breakwaters or bridge piers are often built on a subsoil of sand. The hydraulic loads on the bed are increased by the presence of these structures. A frequently used method of preventing erosion around structures is the use of granular bed protections. A layer of stones or rock covers the sand en prevents it from being transported. The weight of the stones has to be chosen such that the stones can withstand the forces exerted on them by the flow. Only than the bed protection can maintain its function.

Current design practice is to use a stability parameter that represents all the forces on the stone. This stability parameter is used to predict the response of the bed to the forces. Existing stability parameters are often derived for a limited range of application. When the stability parameters are used outside their range of application the bed response is not predicted sufficiently accurate. This leads to inefficient design ant therefore large costs.

The Shields [1936] parameter only uses the bed shear stress and is derived for uniform flow. The stability parameters of Jongeling et al. [2003], Hofland [2005] and Hoan [2008] are focused on incorporating the effects of turbulence properly. And Dessens [2004], Tromp [2004] and Huijsmans [2006] looked at the effects of acceleration on stability based on depth-averaged flow quantities. They found that in accelerating flow there is an extra force exerted on the stone due to the pressure gradient.

In this thesis a stability parameter is proposed that:

- incorporates the effect of turbulence correctly;
- incorporates the effect of advective acceleration;
- can be applied to non-uniform flows

And a relation of this stability parameter and the bed response is established. The bed response is defined by the dimensionless entrainment rate.

Data that contains simultaneous measurements of the flow characteristics and the bed response are collected. A wide range of measurement data is used, to make the stability parameter as general as possible. The data that is used is:

- Measurements in a contraction, from Dessens [2004] and Huijsmans [2006]
- Measurements in an expansion, from Hoan [2008]
- Measurements over a flat bed, from Jongeling et al. [2003]
- Measurements over a short sill, from Jongeling et al. [2003]
- Measurements over a long sill, from Jongeling et al. [2003]

The proposed stability parameter is the one of Hofland [2005] with an extra term that accounts for the force due to the acceleration:

$$\Psi_{\text{RS}} \equiv \frac{\left(\max\left[\left\langle \overline{u} + \alpha\sqrt{k}\right\rangle_{Lm} \frac{L_m}{z}\right]^2\right) + C_{\text{m:b}}\left(\overline{u}\frac{\partial \overline{u}}{\partial x}\right)_{h_a} d}{K(\beta)\cdot \Delta g d}$$

The constants $C_{\text{m:b}}$, α and h_a in this stability parameter are determined with a correlation analysis. The constants that lead to the highest correlation (R^2 = 0.80) are:

$C_{m:b}$	23.0
α	3.75
h_a	9.0 $\cdot d_{n50}$

The relation of this stability parameter with the dimensionless entrainment rate is given by:

$$\Phi_E \equiv 3.95 \cdot 10^{-9} \Psi_{RS}^{5.89} \qquad \text{for } 0.9 < \Psi_{RS} < 4.3 \tag{0-1}$$

The proposed stability parameter performs considerably better than the existing stability parameters for the data sets that are used in this thesis. The new stability assessment method can be used in the design of granular bed protections to recognize and design the parts of the bed protections that are loaded the most by the flow. The input for the stability parameter can be obtained from numerical flow models. Care should be taken with these models because the stability relation derived in this thesis is sensitive to errors in the input variables.

Contents

1 Introduction

Hydraulic structures like groins, breakwaters, bridge piers or pipeline protections are often built on a subsoil of sand. The hydraulic loads on the bed are increased by the presence of these structures which can be the cause of erosion. The erosion of sand endangers the stability and the functioning of these structures and therefore scour needs to be prevented. A frequently used method to do this is the use of granular bed protections. The sand is covered with layers of stone or rock to prevent the sand from being transported. The weight of the stones that are used in the bed protections has to be large enough to withstand the forces that are exerted on them by the flow in order to maintain its function as bed protection.

The dimensions of hydraulic structures are often quite large which subsequently can lead to large surface areas that need to be covered by bed protections. A large amount of stones is required to cover these areas. Also stones are not always available close to the construction site or easy to place. Because of this the costs of bed protections are quite substantial. Accurate methods of predicting the stability or damage to granular bed protections are desired.

In engineering practice, a number of methods exist to predict the stability of granular bed protections. In the first formulations for uniform flows the depth-averaged flow characteristics are written in form of a stability parameter. A critical stability parameter is defined above which the bed becomes unstable. Phenomena like turbulence or non-uniformity are included by means of empirical correction factors. These factors are determined empirically from measurements for specific situations and can certainly not be applied for every situation. Since these formulations do not predict the damage to bed protections sufficiently accurate, the current design practice is to do scale model tests to determine the stone size that has to be used.

Later stability parameters are developed that are based on local flow characteristics and that take into account the effects of turbulence explicitly. These formulations use flow characteristics of the entire water column, obtained from numerical flow computations for example.

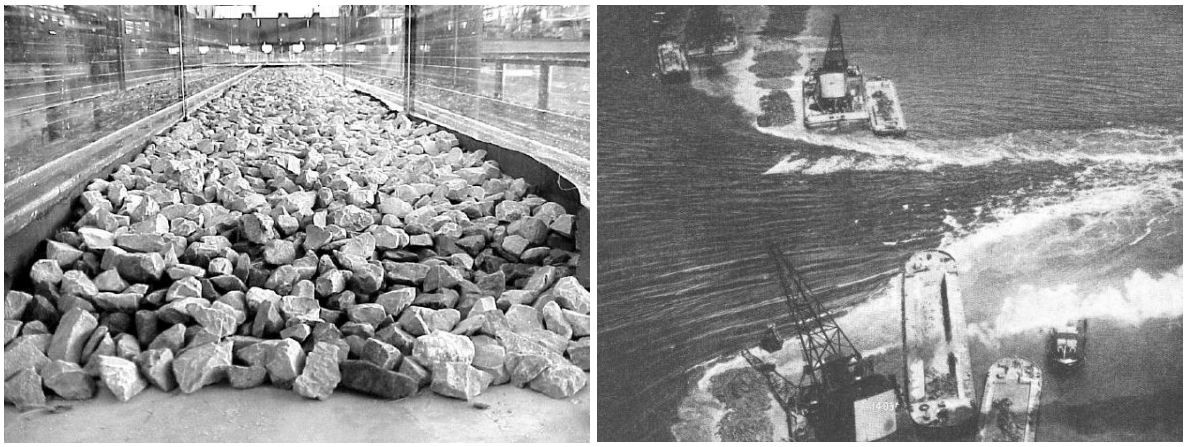

Figure 1-1 A laboratory model of a bed protection (from Hofland [2005]) and a picture of accelerating flow through a closure gap (from www.engwonders.byethost9.com)

Acceleration of flow is a common phenomenon in civil engineering practice, examples are:

- flow over weirs;
- flow through closure gaps;
- flow over pipeline covers;
- flow through locks;
- flow around piers;

- flow around groins;
- flow through spillways
- flow around wind turbines;
- waves;
- turbulence.

Experiments and practice have shown that there is movement of the stones in accelerating flow before the critical velocity is reached. In experiments on the effect of acceleration on stone stability, two identical velocities below the critical velocity were found, one with small and one with large acceleration. In turned out that stones started to move in the latter, while in the former the stones did not move. Examples like these indicate that acceleration influences the start of motion of stones.

1.1 Problem definition and scope

Problem definition

In the existing methods of calculating the response of bed protections to flow forces, a stability parameter describing the forces on the stone is related to a measure for the damage. These forces are loads caused by the flow but also the strength because of the weight of the stone. The existing stability parameters are often derived for a limited range of application. Stability parameters have been derived that focus on the explicit incorporation of turbulence (Jongeling et al. [2003], Hofland [2005] and Hoan [2008]) or that specifically look at the effects of the depth-averaged acceleration of the flow (Dessens [2004], Huijsmans [2006] and Tromp [2004]). When these parameters are applied outside their range of application the scatter of the data points is large and the prediction of the damage is inaccurate. Because of the inaccuracy in these design methods, in practice scale models are used to design bed protections.

The fact that none of the existing stability parameters predicts the damage to the bed accurately enough indicates that not yet all the effects are taken into account correctly. The existing stability parameters that are focused on incorporating the turbulence in non-uniform flow do not take into account the effects of acceleration and deceleration of flow. The stability relations that are found in investigations on acceleration only take into account the depth averaged velocity and turbulence characteristics. As a consequence of this neither of the stability relations predicts the damage to bed protections accurately outside their range of application.

An improvement in the design of bed protections is to formulate a stability parameter in which both the turbulence and the acceleration are taken into account. Both effects should be incorporated based on local flow characteristic and not on depth-averaged quantities. Also, the turbulence should be incorporated explicitly. In this way the stability parameter is applicable for a wide range of non-uniform flow situations.

A conventional method of predicting flow characteristics is the use of Computational Fluid Dynamics (CFD). Examples are Large Eddy Simulation (LES) models or Reynolds-averaged Navier-Stokes (RANS) models. It should be possible to calculate the stability parameter with the output of these kind of models. The improved stability parameter is a step closer to an efficient and accurate design method for granular bed protections in which no physical scale models are necessary. Also the new stability parameter can give more insight in the physical mechanisms that cause the movement of the stones, resulting in more efficient design and therefore reduction of the costs of bed protections.

Scope

Two types of acceleration can be distinguished, i.e. acceleration in time and acceleration in space. For reasons that will be explained in chapter 2, this thesis only deals with the acceleration in space. To avoid ambiguities, a number of terms used in this thesis are defined below.

Material derivative of the velocity:	$a = \frac{Du_i}{Dt} = \frac{\partial u_i}{\partial t} + u_x \frac{\partial u_i}{\partial x} + u_y \frac{\partial u_i}{\partial y} + u_z \frac{\partial u_i}{\partial z}$
Local acceleration, temporal acceleration or acceleration in time	The change of velocity over a certain period of time. This is the term $\partial u_i / \partial t$ in the material derivative of the velocity.
Advective acceleration, spatial acceleration or acceleration in space	The change of velocity over a certain distance in space The terms $u_x \partial u_i / \partial x + u_y \partial u_i / \partial y + u_z \partial u_i / \partial z$ in the material derivative of the velocity.
Uniform flow:	Flow that does not change in the direction of the flow. In this case is $du/dx = 0$ and $du/dy = 0$ but $du/dz \neq 0$
Non-uniform flow:	Flow that does change in the direction of the flow. In this case is $du/dx \neq 0$ or $du/dy \neq 0$ and $du/dz \neq 0$
Bed response	the response of the stones on the bed to the flow forces exerted on them
Damage	the loss of stones from granular bed protections due to flow forces
Acceleration force	the force on a stone due to the acceleration of flow
x direction	The dominant flow direction
y direction	The direction lateral to the dominant flow direction
z direction	The vertical direction

Advective acceleration, spatial acceleration and acceleration in space are all used in this thesis to describe the acceleration over a certain distance in space. Local acceleration, temporal acceleration and acceleration in time are used to describe the acceleration over a certain period of time. Because of the frequency in which the first type of acceleration is referred to, this type of acceleration will often just be called acceleration in the remainder of this report. So, the term 'acceleration' is used when acceleration in space is meant. When acceleration in time is the subject this will be indicated explicitly

1.2 Objectives and research questions

The main objective of this thesis is:

Improving the methods that are used in stability and damage calculations for granular bed protections by including the effects of advective acceleration to the formulations.

This objective can be subdivided in:

1. Design a stability parameter that:
   - incorporates the effect of turbulence explicitly;
   - incorporates the effect of advective acceleration;
   - is based on local flow characteristics and can therefore be applied to non-uniform flows;
   - can be calculated using the output of CFD models;
2. Establish a relation between the proposed stability parameter and the bed response.

To achieve these objectives a number of research questions are formulated:

Q1 What are the forces that are exerted on the stones by the flow?
   a. Which mechanisms cause forces on the stones?
   b. Which expressions can be used to describe the flow forces?
   c. Which flow variables are needed to calculate the flow forces?

Q2 Which data sets that contain simultaneous measurements of the required flow variables and the bed response are available?

Q3 Which flow forces can be included in the stability parameter?

Q4 Can the missing data be reconstructed with the use of numerical models?

Q5 Which methods are available to describe the bed response of granular bed protections?

Q6 What mathematical description can be used for the relation between a stability parameter and the bed response?

Q7 What is the relation between the derived stability parameter and the bed response?

Q8 What is the practical relevance of the stability relation and what uncertainties remain in the prediction of the bed response?

1.3 Thesis outline and approach

In figure 1-2 the approach of this thesis is displayed graphically. Walking through the figure in order of appearance in this report explains how the desired stability assessment method is found in this thesis.

The reports starts with providing a theoretical background on stone stability in chapter 2.1. All the information that is required to understand the stability of the stones in granular bed protections is given. Theory on flow, forces on a stone and the bed response are given. The result of sections 2.1 to 2.3 is the answer to research question Q1. At this point it is clear what flow forces influence the bed response and what data is needed to improve the methods of stone stability assessment.

Data sets that contain the necessary flow variables together with simultaneous measurements of the bed response are required. Section 2.4 gives the data sets that fulfill these requirements. Some of the data sets turned out to be incomplete for the purposes of this thesis. The missing information is reconstructed by modelling the concerning flow configurations numerically in the open source software package OpenFOAM. The numerical modelling is elaborated in chapter 3. The result is the a set of raw measurement data that is used to find the improved stability relation. Research questions Q2, Q3 and Q4 are answered by the combination of required variables, available data sets and the possibility to model the missing data. At this point it is clear that the stability parameter will contain the effects caused by the velocity, turbulence and the advective

acceleration and that the data sets contain information on all of them.

The data sets are used to find a relation between the newly proposed stability parameter and the bed response. But before this can be done the raw measurement data sets must be processed. The data from the measurement instruments should be processed equally for each of the data sets to decrease the errors. The methods of data processing are described in chapter 4. The result is a number of consistent data is used to determine a relation between the improved stability parameter that contains the effects of velocity, turbulence and advective acceleration. In chapter 5 the proposed stability parameter is given. This stability contains a couple of unknown constants. The velocity, turbulence and acceleration from the data sets from chapter 4 are used as input of the stability parameter and the constants that describe the bed response the best are searched for by means of a correlation analysis. In the sections described above, research questions Q5, Q6 and Q7 will be answered.

The answer to research question Q7 is given spread out over chapter 6 and the discussion, conclusions and recommendations in chapters 7 and 8 respectively.

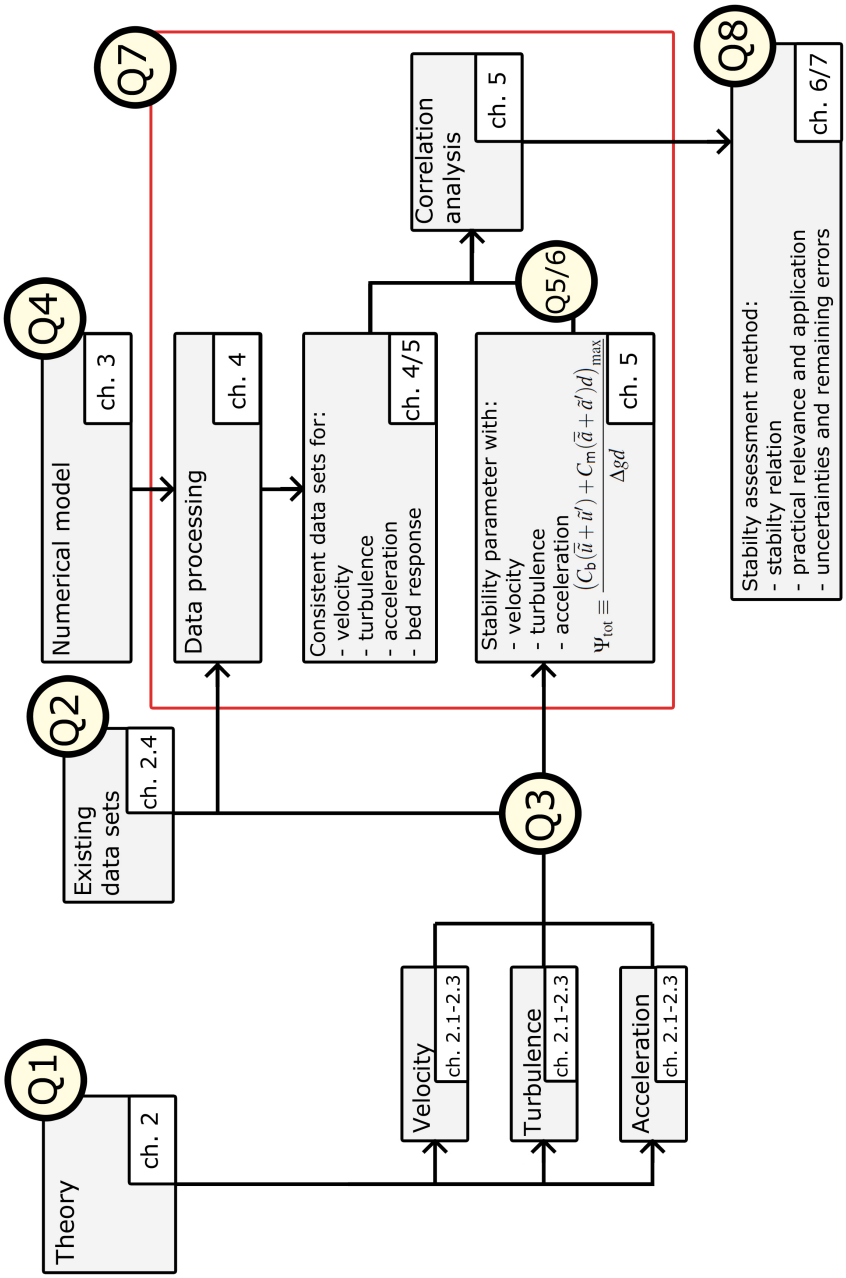

Figure 1-2 Flow chart of the thesis outline

2 Background on Stone Stability

To understand the concepts of stone stability, information is required on the flow and the way the stones are affected by the flow. To obtain a better understanding of the physical aspects of stone stability, first the characteristics of flow are discussed in section 2.1. This information is then used in section 2.2 to assess the forces that are induced by the flow on a single stone. In section 2.3 a number of existing formulas is given that relate flow characteristics to the bulk movement of stones on the bed. Finally, in section 2.4 a summary is given on a number of experiments that are executed concerning the stability of stones.

2.1 Flow

This section will discuss some of the basic aspects of turbulent open channel flow. First the basicc equations governing flow will be given and the physical meaning of the terms will be discussed. After a short explanation of turbulence the Reynolds-averaged equations are given after which the turbulent closure problem is addressed. To understand the flow better, the case of uniform open channel flow is elaborated. Since this is a well-known situation, this can be used to get a basic understanding of open channel flow. Subjects that are considered to be of importance in the understanding of stone stability are discussed (e.g. boundary layers, turbulent intensities, turbulent kinetic energy and shear stresses). When the uniform open channel flow case is given, some theory is given on the characteristics of accelerating and decelerating flow.

2.1.1 Basic equations

Navier-Stokes equations

The equations that govern the evolution of any fluid can be derived using Newton's second law (force equals mass times acceleration) together with the principles of conservation of mass and energy. This derivation can be found in almost every textbook on the subject, therefore it will not be given here. It should be noted that the flow is considered to be incompressible from now, which is a reasonable assumption in the case of open channel flow (Battjes [2002]). Conservation of mass with the assumption of incompressibility leads to the continuity equation for incompressible flow:

$$\frac{\partial u_x}{\partial x} + \frac{\partial u_y}{\partial y} + \frac{\partial u_z}{\partial z} = \nabla_i (u_i) = 0 \tag{2-1}$$

With:

u_i	the velocity [m s^{-1}]
∇_i	the nabla operator [s^{-1}]
i	the directions x, y and z [-]

Newton's second law prescribes that the change of momentum in a fluid element is equal to the sum of forces on the fluid element. Generally, two types of forces on fluid particles can be distinguished (see also Pietrzak [2011]):

Surface forces:	pressure forces and viscous forces;
Body forces:	gravity force and Coriolis force.

The Coriolis force can be neglected since the length scale of interest is too small to be affected by Coriolis. The balance of momentum and forces leads to equation 2-2. This set of equations is

called the Navier-Stokes (NS) equations for incompressible flow.

$$\frac{\partial u_j}{\partial t} + \underbrace{\nabla_i (u_i u_j)}_{\text{convective}} = \underbrace{-\frac{1}{\rho}\nabla_j p + \nu \nabla_i^2 u_j}_{\text{diffusive}} + \underbrace{k_j}_{\text{source}} \tag{2-2}$$

In which:

p	the pressure [kg m^{-1}s^{-2}]
ν	the molecular kinematic viscosity [m^2 s^{-1}]
i, j	the directions x, y and z [-]

Four different terms are recognized in equation 2-2. It should be noted that the viscous shear stresses τ_{ij} are written as $\rho\nu\nabla_i u_j$ in this thesis (see also Battjes [2002]).

1. A local acceleration term $\frac{\partial u_j}{\partial t}$;
2. A convective (or inertia) term $\nabla_i(u_i u_j)$;
3. A diffusive term $-\frac{1}{\rho}\nabla_j p + \nu\nabla_i^2 u_j$, containing pressure related nomal stresses and viscous shear stresses acting on the elementary volume;
4. A source term k_j, which in this case is the gravity term g = 9.81 m s^{-2} for $j = z$.

The Navier-Stokes equations can theoretically, together with the continuity equation and the proper boundary conditions for pressure and velocities, describe all flows. However, due to the non-linearity of the equation it is very hard to find an analytical solution for the equations. Only in configurations where viscosity dominates (e.g. Poiseuille and Couette flows) simple analytical solutions can be found (see also Uijttewaal [2011]). However, for real-life flows with moderate and high Reynolds numbers this is not possible.
A way to come to a proper approximation of the solution is to solve the equation numerically by taking into account all time and length scales. Considering the fact that the smallest length and time scales (the Kolmogorov time and length scales, see appendix A) are in the order of tenths of a millimeter, this is not an option because this would require very large amounts of computational power. A crude estimation on the required number of grid cells leads to $N_{cells} \sim Re^{\frac{9}{4}}$. With the Reynolds numbers occuring in the civil engineering practice that are in the order of 10^6 this would lead to a huge amount of grid cells, making this impossible to solve with the computer power available in the near future. Simplification are required to approximate the solutions of the Navier-Stokes equations and thus reduce computation times.

Reynolds averaging and turbulence closure

To approximate the solution of the Navier-Stokes equations, assumptions are required since it is not possible to calculate all turbulence scales. In appendix A, a background on some concepts of turbulence are given that should be understood before reading this section. A traditional engineering approach to the turbulence, described in Nezu [2005], relies on the Reynolds decomposition of flow variables into mean and fluctuating components ($u = \overline{u} + u'$) and averaging the governing equations resulting in the Reynolds averaged Navier-Stokes (RANS) equations, as shown in equation 2-3.

$$\frac{\partial \overline{u}_j}{\partial t} + \underbrace{\nabla_i (\overline{u}_i \overline{u}_j)}_{\text{convective}} + \underbrace{\nabla_i \left(\overline{u_i' u_j'}\right)}_{\text{Reynolds stresses}} = \underbrace{-\frac{1}{\rho}\nabla_j \overline{p} + \nu \nabla_i^2 \overline{u}_j}_{\text{diffusive}} + \underbrace{\overline{k}_j}_{\text{source}} \tag{2-3}$$

Because of the averaging of non-linear terms. second-order correlations $-\overline{u_i' u_j'}$ arise. These

terms are called Reynolds stresses and they lead to 9 additional unknowns in the equations (of which 6 are independent because of the symmetry). The Reynolds shear stress can be written analogously to the viscous shear stress $\rho\nu\nabla\overline{u_j}$ by introducing a turbulent kinematic viscosity ν_t. Relating the Reynold stresses to the mean stresses using a turbulent kinematic viscosity ν_t is often referred to as the Boussinesq eddy visocosity assumption. In this way, the Reynolds stresses are written as $\rho\nu_t\nabla\overline{u_j}$. This turbulent viscosity ν_t can be seen as a variable that accounts for the effects of turbulence on the viscosity.

To solve the RANS equations, additional equations are necessary to approximate the Reynold stresses. These Reynolds stresses must be related to the mean flow variables to solve the RANS equations. This is referred to as the classical turbulence problem or closure problem. A number of methods exist to close the equations:

1. Constant eddy viscosity models;
2. Mixing length models;
3. The k-ε model;
4. The k-ω SST model;
5. Reynolds stress modelling;
6. Large Eddy Simulation (LES).

All of the methods have their own benefits and flaws and it depends on the situation which model is the best. Detailed descriptions of these model can be found in, amongst others, Rodi [1980], Nezu [2005] or Uijttewaal [2011]. The k-ω SST model is elaborated in chapter 3 on numerical modelling.

Here, only the mixing length model of Prandtl is discussed because this model is very convenient to illustrate some typical flow features. It is already mentioned that the Reynolds stresses can be expressed analogously to the viscous shear stresses. The resulting eddy viscosity can be seen as the product of a velocity and a length scale. Prandtl [1925] stated, as a rough estimation, that the velocity that characterizes the turbulent fluctuations is proportional to the velocity difference in the mean flow over a distance l_m over which the mixing or transport of momentum takes place ($u'_x = -l_m\frac{\partial u_x}{\partial z}$). This leads to and expression for the turbulent viscosity ν_t as in equation 2-4.

$$\nu_t = l_m^2\left|\frac{\partial u_x}{\partial z}\right| \tag{2-4}$$

This is called Prandtl's mixing length hypothesis. and is used for the closure of the RANS equations (i.e. relating $-\overline{u'_iu'_j}$ to u_j) as in equation 2-5.

$$-\overline{u'_xu'_y} = -\nu_t\frac{\partial u_x}{\partial z} = l_m^2\left(\frac{\mathrm{d}u_x}{\mathrm{d}z}\right)^2 \tag{2-5}$$

With:

l_m the Prandtl mixing length [m]

For this mixing length, Prandtl proposed the relation in equation 2-6.

$$l_m^2 = \kappa z \tag{2-6}$$

In which

z the height in z direction[m]
l_m the Prandtl mixing length [m]
κ the von Karman constant ($\kappa \approx 0.41$) [-]

At the wall, the effects of the viscosity is not negligible anymore and also has its effects on the mixing length in the Prandtl mixing length model. Van Driest [1956] expanded the relation from equation 2-6 to include the effects of the viscosity near walls. In this equation the governing variables are made dimensionless.

$$l_m^{+2} = \kappa z^+ \Gamma(z^+) \qquad \text{and} \qquad \Gamma(z^+) = 1 - \exp\left(-\frac{z^+}{B_{vD}}\right) \tag{2-7}$$

Here is:

z^+ the dimensionless height above the bed ($z^+ = z/(\nu/u_\tau)$) [-]
l_m^+ the dimensionless mixing length ($l_m^+ = l_m/(\nu/u_\tau)$) [-]
$\Gamma(z^+)$ the van Driest damping function
B_{vD} the damping factor (often taken as 26)

2.1.2 Uniform open channel flow

The case of uniform open channel flow has been investigated intensively and is therefore an excellent situation to get a feeling about open channel flow. Nezu [2005] gave an overview on the turbulence research that is done until that time. Nezu [2005] also describes the open channel case and this description is followed here for the lragest part.

In the idealized case of uniform open channel flow over a smooth bed all the forces are in equilibrium, see figure 2-1, meaning that the shear stresses is equal to the effect of the gravitation. The momentum balance for a volume of water for this 2D flow situation is given in 2-8.

$$\tau_b = \rho\nu \frac{\partial u}{\partial z}\bigg|_{z=0} = \rho u_\tau^2 = \rho g h i \tag{2-8}$$

With:

τ_b the bed shear stress per unit of width [N m^{-2}]
h the water depth [m]
u_τ the shear velocity [m s^{-1}]
i the energy slope (equal to the bed slope in uniform flow) [-]

The variable u_τ is the shear velocity and is a measure for the shear stress at the bed, rewritten in the units of velocity. The shear velocity is commonly used in practice and the definition of u_τ is given in equation 2-9. The location of the velocity fluctuations is near the bed, but outside of he influence of roughness and viscosity.

$$u_\tau = \sqrt{\tau_b/\rho} = \sqrt{\overline{u'_{x,b} u'_{z,b}}} \tag{2-9}$$

With:

$u'_{x,b}$, $u'_{z,b}$ the fluctuating part of the velocity in x and z direction near the bed

The Reynolds-averaged Navier-Stokes momentum equation in x direction can be simplified for 2D uniform open channel flow (see Villanueva [2010] for the whole derivation). Under the

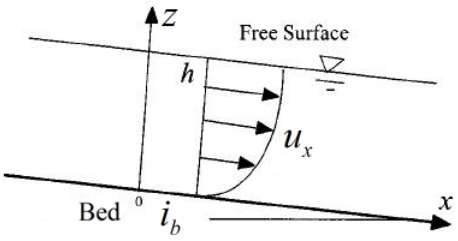

Figure 2-1 Definition sketch for steady 2D uniform open channel flow (adapted from Nezu [2005])

assumption of a two-dimensional steady state situation with constant shear stress (Uijttewaal [2011]), equation 2-3 can be simplified to equation 2-10 for the momentum equation in x direction.

$$\frac{\partial}{\partial z}\left[(\nu+\nu_t)\frac{\partial u_x}{\partial z}\right]=\frac{1}{\rho}\frac{\mathrm{d}p}{\mathrm{d}x} \tag{2-10}$$

Integrating equation 2-10 over the water depth, using the definition for u_τ and the simplified Navier-Stokes equation gives equation 2-11.

$$(\nu+\nu_t)\frac{\partial u_x}{\partial z}=-\overline{u_x'u_z'}+\nu\frac{du_x}{dz}=u_\tau^2(1+\gamma) \tag{2-11}$$

With:

γ height relative to the water depth ($\gamma=z/h$) [-]

Equation 2-11 can be combined with the Prandtl mixing length model (see equation 2-5). This gives equation 2-12. This equation is written as function of the dimensionless wall variables u_x^+, z^+ and l_m^+. These values can be obtained by dividing u_x by u_τ and z and l_m by ν/u_τ respectively.

$$\frac{du^+}{dz^+}=\frac{2(1-\gamma)}{1+\sqrt{1+4l_m^{+2}(1-\gamma)}} \tag{2-12}$$

Where:

u_x^+ the dimensionless velocity ($u_x^+=u_x/u_\tau$) [-]

Close to the wall, where $\gamma \ll 1$, the above leads to the well-known law of the wall and applies to almost to every turbulent flow near a solid boundary. The law of the wall is given in equation 2-13.

$$\frac{du_x^+}{dz^+}=\frac{2}{1+\sqrt{1+4l_m^{+2}}} \tag{2-13}$$

The law of the wall is examined for different levels (z^+) above the bed, these are shown in table 2-1.

Region	Layer	Velocity	Description
$0 > z^+ < 5$	Viscous sublayer	$u^+ = z^+$	Viscous effects are dominant in this layer. Using that $z^+ \to 0$ and the no-slip condition at the wall leads to this linear relation.
$5 > z^+ < 30$	Buffer layer	-	An analyitical solution for the buffer layer is not available. The buffer layer is usually approximated by extrapolation between the viscous sublayer and the log-law layer
$30 > z^+ < 300$	Log-law layer	$u^+ = \frac{1}{\kappa}\ln z^+ + B$	The effects of viscous effects diminish such that the Van Driest [1956] damping function is 1 and turbulent stresses are dominant. This gives to the well-known log-law.
$z^+ > 300$	Outer layer	$u^+ = \frac{1}{\kappa}\ln z^+ + B + w(\gamma)$	The turbulent shear stresses are still dominant but cannot be considered constant anymore. Coles [1956] proposed a modification with the so-called wake function $w(\gamma) = \frac{2\Pi}{\kappa}\sin^2\left(\frac{\pi}{2}\gamma\right)$ with Π Cole's wake strength parameter. Also, a critical wall distance ($z_c \approx 0.2 \cdot$ the boundary layer thickness) is defined above which the modification should be applied.

Table 2-1 Wall regions in open channel flow

Although flow, as can be seen above, is divided into different regions, the log-law layer is often used to describe the velocity profile over the whole depth of open channel flows (Keulegan [1938]). In Nezu and Rodi [1986] the values for κ and the integration constant B are given as 0.41 and 5.29 respectively.

Turbulent kinetic energy

In Nezu [1977] proposed the universal functions for the turbulence intensities u', v' and w' shown equation 2-14.

$$\frac{u'_x}{u_\tau} = D_x \exp(-C_k\gamma) \qquad \frac{u'_y}{u_\tau} = D_y \exp(-C_k\gamma) \qquad \frac{u'_z}{u_\tau} = D_z \exp(-C_k\gamma) \tag{2-14}$$

With D and C empirical constants independent of the Reynolds number and the Froude number. HFA[1] and LDA[2] measurements for a number of open channel flows (Nezu and Rodi [1986]) showed that:

D_x = 2.30
D_y = 1.63
D_z = 1.27
C_k = 1.00

Equation 2-14 in combination with the constants given above is applicable in the region $< 0.1\gamma <$

[1] Measurement intstrument: Hot Film Anemometer
[2] Measurement intstrument: Laser Doppler Anemometer

0.9, where the generation of the turbulent kinetic energy k is equilibirum with the dissipation of k. The turbulent kinetic energy can be described by equation 2-15.

$$k = \xi \cdot (\overline{u_x'^2} + \overline{u_y'^2} + \overline{u_z'^2}) = \xi \cdot (\sigma_{ux}^2 + \sigma_{uy}^2 + \sigma_{uz}^2) \tag{2-15}$$

Where:

- k the turbulent kinetic energy [m^2 s^{-2}]
- ξ an integration constant
- σ the standard deviation

Substituting the empirical equations for the turbulence intensities in this equations gives the empirical formulation of the turbulent kinetic energy. This relation, given in equation 2-16, can be used to estimate the turbulent kinetic energy profile in unform flow.

$$\frac{k'}{u_\tau^2} = \frac{\overline{u'^2} + \overline{v'^2} + \overline{w'^2}}{2u_\tau^2} = 4.78\exp(-2\gamma) \tag{2-16}$$

Turbulent viscosity

Equation 2-8 is used to obtain a definition for ν_t in uniform open channel flow. The term $\partial\overline{u_x}/\partial z$ is calculated using the derivative of the log law and τ is obtained from equation 2-9. Equation 2-17 shows the result. This profile follows a parabolic curve. This states that the turbulent viscosity is zero at the bed as well as at the free surface. This can be explained by the fact that due to the density jump from water to air turbulent fluctuations can hardly penetrate the free surface. However, in strongly turbulent flows the free surface can exhibit small vertical fluctuations, indicating that the turbulent viscosity is larger than zero here.

$$\nu_t = -\frac{\tau}{\rho\frac{\partial\overline{u_x}}{\partial z}} = \frac{\frac{h-z}{h}\frac{\tau_b}{\rho}}{\frac{u_\tau}{\kappa z}} = \kappa u_\tau h\gamma(1-\gamma) \tag{2-17}$$

With:

- h the waterdepth [m]

Bed roughness

The above derived log-law for boundary layers $u^+ = \frac{1}{\kappa}\ln z^+ + B$ is derived for a smooth wall. However, the majority of flows in practice are rough flows and the influence of the roughness should be included. Rewriting the integration constant B by writing in in the form of an equivalent roughness height gives equation 2-18.

$$u^+ = \frac{1}{\kappa}\ln\frac{z^+}{z_0} \tag{2-18}$$

With: z_0^+ the equivalent roughness height [-]

The flow can now be divided into three roughness regimes (i.e. smooth, intermediate and rough). The bed is considered smooth when the roughness elements are submerged within the viscous sublayer, while the wall is considered rough when the roughness elements penetrate into the buffer layer or log-law layer. An overview is given in table 2-2. Note that the expression for

smooth walls is no different from what is stated before, only the notation has changed.

Region	Regime	z_0^+
$k_s^+ < 5$	Smooth	$0.11\frac{\nu}{\lvert u_\tau \rvert}$
$5 < k_s^+ < 70$	Intermediate	$0.11\frac{\nu}{\lvert u_\tau \rvert} + \frac{k_s}{30}$
$k_s^+ > 70$	Rough	$\frac{k_s}{30}$

Table 2-2 Different wall regions

With:

k_s^+ dimensionless equivalent roughness ($k_s^+ = \frac{k_s u_\tau}{\nu}$) [-]
k_s the equivalent sand roughness by Nikuradse [m]

Nikuradse [1933] found that for flow over a bed with a single layer of glued sand grains the value of $z_0 = k_s/30$, with k_s the sand diameter. Later research (Hofland [2005]) showed that z_0 could vary to $z_0 \approx d_{n50}/10$ for a bed of randomly placed stones. The value of k_s is thus found as 1 to 3 times the nominal stone diameter d_{n50}. On a rough bed, it is also not straightforward where the position $z = 0$ is, because of the random character if the stones. The level of the theoretical bed varies from $0.35k_s$ to $0.15k_s$ under the tops of the roughness elements. The flow near the rough bed is influenced considerably by the shape of the bed and represents the so-called roughness sublayer (Hofland [2005]). The average velocity profile is approximately linear between the roughness elements.

Turbulent structures

Although turbulent flows are highly variable and chaotic, still certain similar flow patterns can be observed repeatedly. These patterns are called 'coherent structures'. Hofland [2005] mentions a number of phenomena that are summarized here. The bursting process is a well-known generation mechanism near smooth walls. Irregularities of the viscous sublayer grow into hairpin vortices that become unstable and get bursted into the outer layer. These hairpins form counter-rotating streamwise vortices near the wall. However, for rough beds this is difference because the scale of this phenomenon is smaller than the stones on a rough bed. Raupach [1981] performed a quadrant analysis to a point measurement of a rough-bed flow. He found that the event in which $u_x' > 0$ and $u_z' < 0$ is the most important contribution to the Reynolds stress near the bed where the event in which $u_x' < 0$ and $u_z' > 0$ is dominant in smooth wall flow. Further from the wall the contribution of both of these events is equal to smooth wall flow. So, in rough flow, a downward movement of an increased horizontal velocity is the main contributor to the Reynolds stress.

In amongst others Grass [1971], Nezu [1977] and Buffin-Bélanger et al. [2000] it is stated that the outerflow contains coherent structures, roughly consisting of wedge-shaped areas with uniform momentum bordered by small-scale hairpin vortices. These hairpin vortices are quite common in near wall flow and can originate from the instability of the viscous sublayer or from the shedding of hairpin vortices from the roughness elements on the bed.

Turbulent wall pressures

Turbulent wall pressures (TWP) are the pressure fluctuations on the bed that are caused by turbulent eddies. These pressures are solely a result of the turbulence and also act on smooth walls (so they are not dependent on the bed roughness). In Hofland [2005] it is stated that TWP in an incompressible fluid are caused by the velocity fluctuation gradients in the entire fluid domain at a certain moment, although the contribution of a single source decreases with its distance from the wall. Lower-frequency TWP are generally caused by larger-scale fluctuations further away.

Windtunnel tests (Schewe [1983]) showed that pressure fluctuations of four times the standard deviation of the TWP exist.

2.1.3 Accelerating open channel flow

Acceleration of flows is caused by a pressure gradient in the flow direction. This pressure gradient causes a difference from the boundary layer thickness in uniform flow. A negative pressure gradient in streamwise direction (i.e. acceleration) causes a reduction of the boundary layer thickness. The term $\partial u_x/\partial z$ becomes larger and, according to equation 2-5 and so do the shear stresses. A positive pressure gradient (i.e. deceleration of the flow), however, results in an increase of the boundary layer thickness. The deceleration of the flow can even get to the point where the smallest velocities (i.e. the ones near the bed) become negative. This phenomenon is called flow separation and is associated with a large production of turbulent kinetic energy. Figure 2-2 shows these phenomena.

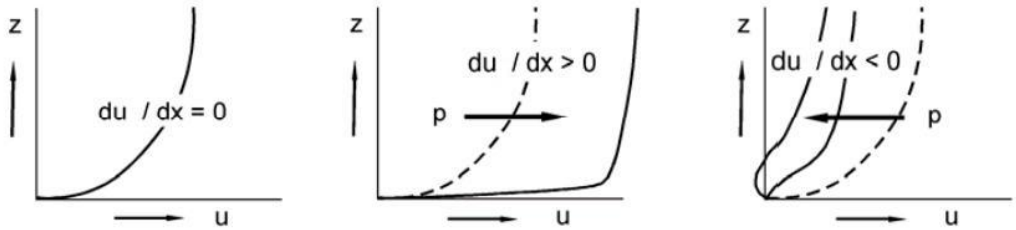

*Figure 2-2 The influence of pressure gradients on velocity profiles (from **?**)*

Figure 2-3 shows the results are shown from an experiment in which turbulence characteristics are measured in accelerating and decelerating flow (by using different slopes of the bed). In this figure the parameter β is a measure for the pressure gradient (see Song and Chiew [2001], with $\beta = -1$ for uniform flow, $\beta < -1$ for accelerating flow and $\beta > -1$ for decelerating flow.

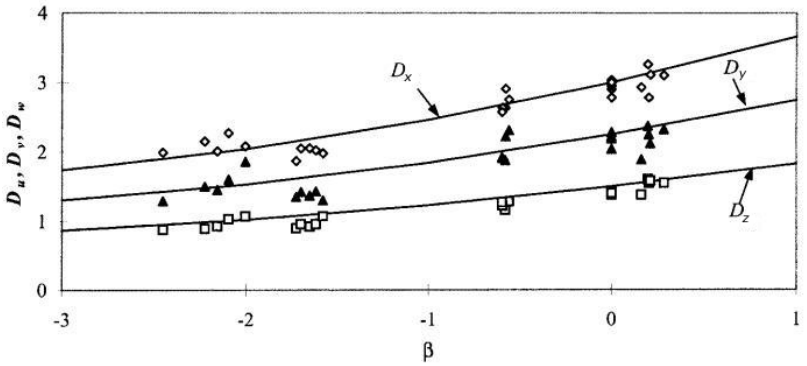

Figure 2-3 Releation between the constants in equation 2-14 and the pressure gradient parameter β from Song and Chiew [2001]

It is clear that for accelerating flow the value of D_x, D_y and D_z decreases for all directions. In decelerating flow to opposite happens and the values of D_x, D_y and D_z increase. The fact that D changes, indicates that the ratio u'/u_τ but says nothing on the actual increase or decrease of u'. It has already been mentioned before that in accelerating flow the velocity profile deviates from a uniform flow profile and that the bed shear stress, and thus u_τ, is usually larger. Song and Chiew [2001] is not clear about this ratio, but a quick analysis of the measurement data can give more information. Song and Chiew [2001] gives the u_τ derived from the measurements for a number of different configurations. This value can be used to calculate how the relative value

of u_x' (= $u_\tau \cdot D_x$) changes as a consequence of different values of the pressure gradient, expressed as β. Figure 2-4 shows the results of this calculation for the streamwise direction.

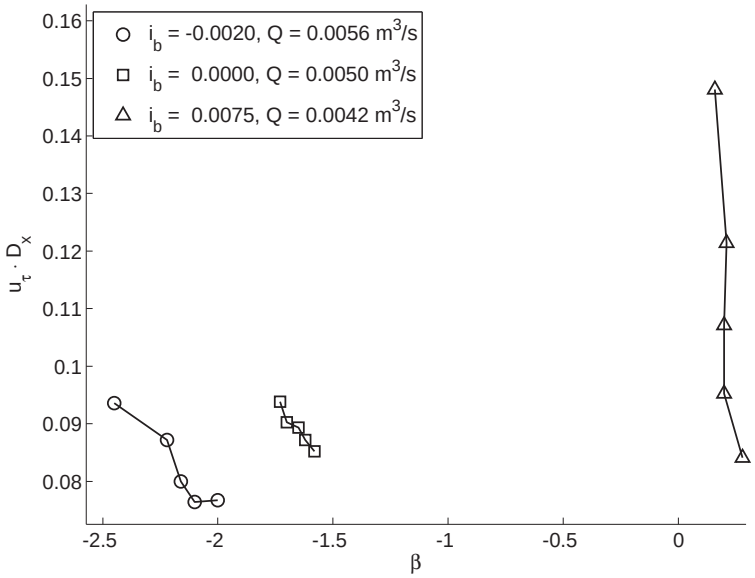

Figure 2-4 Change of turbulence intensities in accelerating flow from, calculated with values of Song and Chiew [2001]

In figure 2-4 it is visible that for comparable flow conditions in the experiments of Song and Chiew [2001] relative value of u_x' increases when β gets smaller. The difference in β is obtained by changing the width of the flume, which could explain the increase in the relative value of u_x'. Looking at the different situations separately the relative value of the turbulence intensity u_x' is decreases for different values of β. It should be mentioned that the slope of the bed is the reason of the acceleration in the experiment by Song and Chiew [2001]. In other accelerating type of flows (e.g. the flow in a contraction or over and around structures) these characteristics can be different again. In Schiereck [2001] the results from a wind tunnel test with a local contraction are given. Figure 2-5 shows these results and it can be seen that the turbulence intensity in streamwise direction decreases because the flow got more concentrated in that direction. The turbulence intensity in vertical direction increased in this geometry.

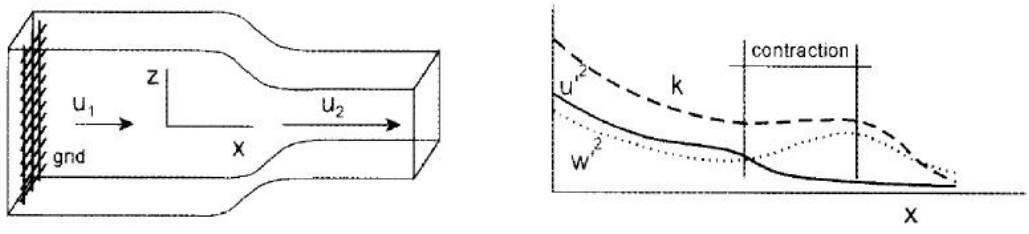

Figure 2-5 Turbulence in a local contraction Schiereck [2001]

The most important conclusion that can be made from the above is that the turbulence characteristics in non-uniform flow are far from trivial. The relation between velocities, acceleration and turbulence is different for different types of acceleration (due to e.g. a change in slope, a constriction in the vertical or a constriction in the horizontal). No general formulation is available to describe the turbulence intensity in non-uniform flow.

2.2 Forces on a single stone

When a bed exists of randomly places stone, water that flows over this bed exposes the stones to several forces. To understand the mechanism of stone stability better, first the forces on a single stone will be examined. In section 2.2.1 the forces caused by the fact that water flows with a certain velocity will be discussed. In section 2.2.2 some information is given on the mechanism that causes forces on the stone in an accelerating flow.

2.2.1 Forces caused by velocity

There are several mechanisms that generate forces on a stone when water is flowing above it with a certain velocity. In this section, these mechanisms causing forces on a stone will be given for uniform flow.

Drag and Lift forces

In figure 2-6 an overview is given of the forces on a stone. The stones are exposed to a fluid flow, which results in different forces on the stone. First there is a shear force (indicated as F_1 in figure 2-6) present on the rough surface of the stone. Secondly there is a force (indicated as F_2 in figure 2-6), caused by the occurrence of a small wake behind the stone, creating a pressure difference between the front and the back of the stone. The resultant force of F_1 and F_2 together is called the drag force F_D. The relative importance of each of these forces is determined by the value of the particle Reynolds number in equation 2-19. This number indicates whether the stone protrudes into the buffer layer or further or if it stays within he viscous sub layer.

$$Re_* = \frac{u_\tau d}{\nu} \tag{2-19}$$

In which d is the stone diameter. According to Hoan [2008] if Re_* is smaller than 3.5, the viscous stresses dominate and the shear force is dominant. When Re_* becomes larger, flow separation will occur behind the stones creating a small wake with vortex shedding behind it. If this is the case, the force caused by the flow separation becomes dominant over the shear force. At a value of $Re*$ that is larger than approximately 500, the shear force becomes negligible.

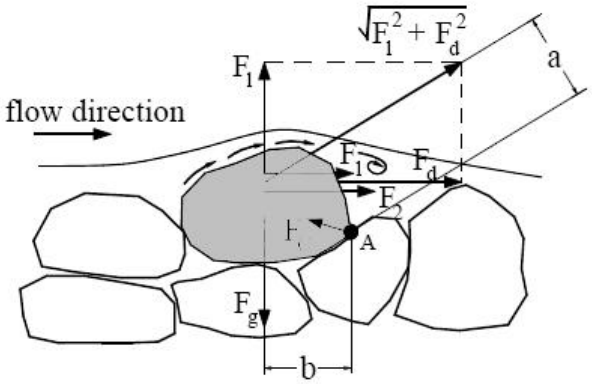

Figure 2-6 Forces acting on particles resting on a bed surface from Hoan [2008]

Next to the drag force F_D there also is a lift force F_L. The lift force is caused by the velocity difference between the top and the bottom of the particle. Since both the drag force as well as the lift force are a result of pressure differences at all sides of the particle. Applying the law of Bernoulli (see Battjes [2002]) shows that these forces are proportional to the velocities in the vicinity of the stone. Therefore, the drag and lift forces can be expressed in general form as in

equation 2-20b and 2-20b.

$$F_D = \frac{1}{2} C_D A_D \rho u |u| \tag{2-20a}$$

$$F_L = \frac{1}{2} C_L A_L \rho u |u| \tag{2-20b}$$

With:

- C_D the drag coefficient [-]
- C_L the lift coefficient [-]
- A_D the surface area exposed to the drag force ($A_D \propto d_{n50}^2$) [m^2]
- A_L the surface area exposed to the lift force($A_l \propto d_{n50}^2$) [m^2]
- u the velocity in the vicinity of the stone [m^{-2}]

The drag and lift coefficients depend on the flow pattern around the bed particle and the method of estimating u. The definition of u is rather vague and therefore multiple definitions are available (e.g. $\overline{u}$, u at $0.15d$ or u_τ) that all lead to different values of the coefficients.

Quasi-steady forces (QSF)

In the previous section a constant velocity above the bed is assumed. However, as already discussed in section 2.1 the flow over a rough bed is turbulent. The velocity exists of a mean and a fluctuating part (e.g.$u = \overline{u} + u'$) and because on these large scale turbulence fluctuations the forces acting on a particle also fluctuate. Coherent structures can cause that a fluid package from higher up the water column (with a certain velocity) is transported downwards to the bed, resulting in a fluctuating force at the bed. An other cause of a fluctuating force of the particle is the unsteady separation of the flow from the particle. Because it is basically the same flow mechanism that causes the forces on the stone, these forces are referred to as the quasi-steady forces (QSF)

Generally, the fluctuating parts of the velocity are much smaller than the mean velocity. However, Hofland [2005] states that close to the bed the extreme values of $|u'|$ can have the same order of magnitude as $\overline{u}$ itself. This means that their contribution to the forces on the stone is considerable. Substituting $u = \overline{u} + u'$ in equation 2-20b and 2-20b gives equation 2-21a and 2-21b for the drag force and the lift force respectively

$$F'_D \propto 2\overline{u}u' + u'^2 - \overline{u'^2} \tag{2-21a}$$

$$F'_L \propto 2\overline{u}u' + u'^2 - \overline{u'^2} \tag{2-21b}$$

Not many measurements are available to validate these equations. In Hofland [2005] a number of references are mentioned (amongst others Radecke and Schulz-DuBois [1988]) that propose a relation for the fluctuating part of the drag and lift force. The relations in these references suggest that the magnitude of the fluctuating part of the drag force is in the same order of magnitude as the time-averaged force, meaning that they have a considerable influence on the total force on the stone.

Hofland [2005] found that the drag caused by longitudinal velocity fluctuations u'_x is probably the source for the largest and most important force fluctuations. When a positive movement of the

horizontal velocity u_x coincides with a negative vertical velocity u_z', the horizontal velocity penetrates deeper into the bed, increasing the exposed area of the stone and therefore also the drag force. Also, the higher velocity on the top of the stone because of u_x' causes the pressure difference between the top and the bottom to increase, temporarily increasing the lift force also. On the other hand, the negative vertical velocity has a stabilizing effect again, since it has a negative contribution to the lift force. Summarizing, during extreme values of u_x near the bed the drag force is increased, while the lift force is decreased due to the vertical velocity component. From the above, it can be concluded that the origin of the quasi-steady force lies both on the influence of the bed as well as in the existence of turbulent structures higher in the water column. In Hofland [2005] it is stated that the duration of the largest quasi-steady forces is long enough to make the stone roll away and therefore it is expected that the fluctuating part of the drag and lift forces play an important role in the stability of the stones on the bed.

2.2.2 Forces caused by acceleration

Next to the velocity, the acceleration of a flow itself also exerts a force on the stones. Again, one can distinguish a time-averaged acceleration $\bar{a}$ and a fluctuating part of the acceleration a'. The spatial acceleration can be caused by structures while the fluctuation can be caused by for example waves or turbulent structures. In this section, only the forces caused by spatial acceleration of flow and turbulent structures will be discussed. For more information on accelerations in waves one is referred to Tromp [2004].

In figure 2-7 the acceleration of flow around a stone is shown in a simplified way.

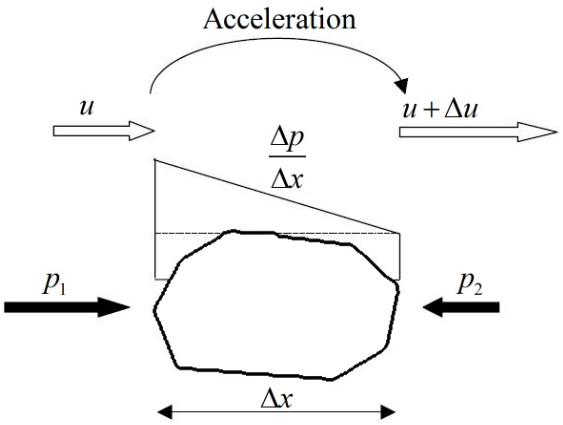

Figure 2-7 The pressure difference due to acceleration from Dessens [2004]

In Hofland [2005] and Dessens [2004] the net force on a particle caused by a pressure gradient is mentioned. Hofland [2005] made the comparison with the buoyancy force on a sphere due to the hydrostatic pressure gradient. Also, when a the sphere is accelerating relative to the flow, an extra force is exerted on the sphere in consequence of the acceleration of the fluid surround the sphere, called the added mass. This is investigated in Maxey and Riley [1983] and both forces are shown in equation 2-22.

$$F_a = \rho V \frac{\mathrm{D}\overline{U}}{\mathrm{D}t} + \rho V C_\mathrm{m} \left(\frac{\mathrm{D}\overline{U}}{\mathrm{D}t} - \frac{\mathrm{d}v_p}{\mathrm{d}t} \right) \tag{2-22}$$

With:

C_m the added mass coefficient [-]
v_p the velocity of the particle [m^s−1]

In Dessens [2004] the formulation in equation 2-23 is used to account for the acceleration in the stability parameter. The derivation of this formulation is found in appendix B.

$$F_a = -C_m V \frac{\partial p}{\partial x} = C_m \rho V \frac{Du}{Dt} = C_m \rho V \left(\frac{\partial u}{\partial t} + u \frac{\partial u}{\partial x} \right) \tag{2-23}$$

Often, the total force is calculated by adding up the force caused by the velocity and the force caused by the acceleration. This method is often referred to as the Morison approach (see Morison et al. [1950]). Equation 2-24 gives the Morison equation

$$F_{tot} = F_u + F_a = \frac{1}{2} C_b \rho A u_x |u_x| + C_m \rho V \frac{Du_x}{Dx} \tag{2-24}$$

with:

C_b the bulk coefficient that accounts for the drag and lift forces
C_m the coefficient that accounts for the effects the acceleration

The added mass coefficient C_m accounts for the additional extra pressure force that occurs when the neighbouring fluid around the stone is accelerated. The value of C_m is relatively unknown in theory. A simple relation for C_m is given by Dean and Dalrymple [1991] (see figure 2-8):

$$C_m = 1 + k_m \tag{2-25}$$

With:

1 the part of the force caused by the pressure gradient [-]
k_m the part of the force caused by the 'added mass' [-]

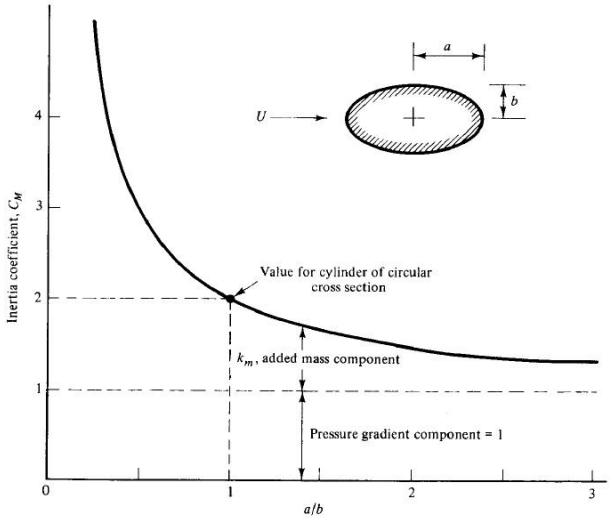

Figure 2-8 Relation added mass coefficient k_m and the particle shape from Dean and Dalrymple [1991]

In Dessens [2004], Huijsmans [2006] and Tromp [2004] the effect of acceleration on stone stability is investigated further. Dessens [2004] did measurements in a flume with a local contrac-

tion. The depth-averaged mean velocity is coupled with the peak velocity in accelerating flow (which deviates from the logarithmic profile in uniform flow). The acceleration is calculated using the measured velocity profiles at different locations in the dominant flow direction. Dessens [2004] used combinations with equal velocities but different accelerations to find the effect of acceleration on stability. C_b and C_m are found using the Morison formula together with the threshold of motion. The values of the constants depend on the pivoting angle, which is the most common angle of initiation of movement. In Tromp [2004] the stability of stones under waves is investigated. Table 2-3 gives the values of C_b and C_m that are found in the research of Dessens [2004] and Tromp [2004] respectively.

Pivoting angle	**C_b**	**C_m**	**C_b / C_m**
Dean and Dalrymple [1991]			
-	-	0.3 - 3.0	-
Dessens [2004]			
30°	0.10	3.92	39.2
45°	0.14	5.55	39.6
Tromp [2004]			
-	0.40 - 0.55	2.67 - 3.75	4.85 - 9.375

Table 2-3 Values of C_b and C_m found by Dean and Dalrymple [1991], Dessens [2004] and Tromp [2004]

In practice and in experiments it is observed that stones start to move in accelerating flow before the critical velocity is reached, which confirms the idea that acceleration exerts a force on the stone. Hofland [2005] and Hoan [2008] both mention that the effect of acceleration could be of importance, although they did not investigate this. In Dessens [2004], Huijsmans [2006] and Tromp [2004] it is demonstrated that the acceleration had an important influence on the stability of stones.

It should be mentioned that the acceleration of the flow, next the the force in exerts on the stone, also influence other flow characteristics like the velocity and the turbulence, as is discussed in section 2.1.3. It appears that in accelerating flow the turbulence intensities decrease, while the velocities near the bottom become larger. So, next to the direct influence of the resulting pressure gradient on the stone, the forces on the stones are also indirectly influenced by the acceleration of the flow due to its influence on other flow variables. In decelerating, the opposite of the above happens. The positive pressure gradient in flow direction causes an opposite pressure difference on the stone, resulting in a net force in the direction contrary to the flow. This could have a stabilizing effect on the stones. However, decelerating flow shows an increase in turbulence. From the above it follows that the velocity, the turbulence and the acceleration (and deceleration) interact with each other. The above has also been observed by Huijsmans [2006]. Here, the effect of turbulence is not included and for some of the measurements it is found that stones became more stable when the acceleration is larger. This indicate that the decrease of turbulence intensities in accelerating flow also has an effect on stone stability.

Turbulence Wall Pressure

Another force-generating mechanism is assumed to act in addition to the quasi-steady forces and the force caused by spatial acceleration, are the turbulence wall pressures (TWP). In section 2.1.2 it is already discussed that the turbulent wall pressures are directly induced by the turbulent flow itself. The fluctuating pressure is associated with the effects of the fluctuating accelerations (Newton's second law). Integrated over a stone, the TWP result in net forces on the stone and they therefore contribute to the fluctuating forces on a stone. The idea of the effect of a vortex passing a stone is shown in figure 2-9.

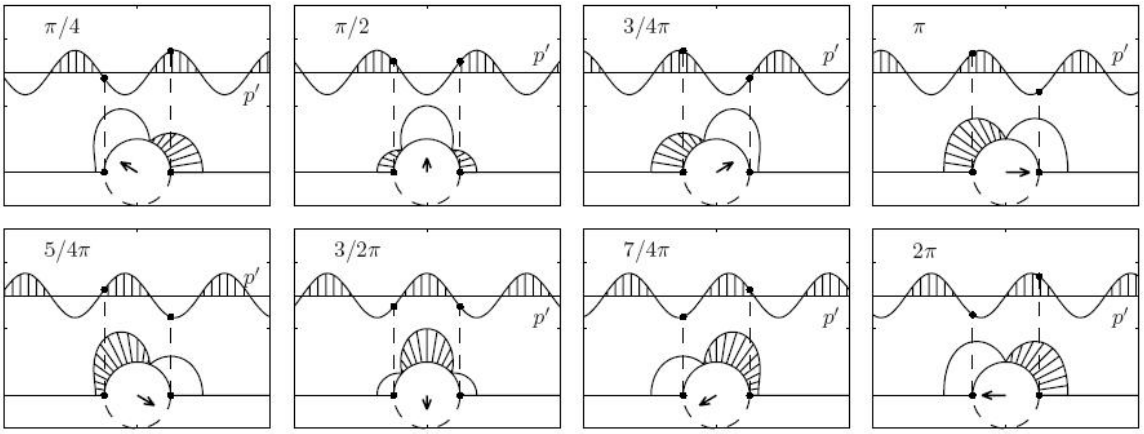

Figure 2-9 Change of integrated forces on a stone. The vectors represent the resulting forces. From Hofland [2005]

In Hofland [2005] it is concluded that TWP are of importance for the movement of stones, especially for stones that are shielded by other stones. The relative influence of TWP seems to be larger on the lift force than on the drag force. The flow structures causing TWP are small with a short duration. According to Hofland [2005] the TWP are especially important for the movement of stones despite of the fact that these forces by themselves will merely lead to a upward-downward motion of the stone. Often the stone gets an initial lift (or rotation) by an intense, small-scale fluctuation of the vertical velocity, related to the TWP. This increases the exposed area of the stone such that it is moved more easily by the increased streamwise velocity reaching the stone, connected to the QSF. From this it can be concluded that stones are generally moved by an exceptional combination of the TWP and the QSF above. The stone is given an initial vertical movement by the TWP after which the QSF can carry it away. So at least one of the phenomena has to have an exceptionally high magnitude.

2.2.3 Forces caused by stone placement

Next to flow forces, the placement of the stones also is a cause of forces exerted on the stone. An important influence is the effect of the slope of the bed. In upward sloping beds (with respect to the flow direction) the gravity of the stones imposes a force counteracting the direction of the flow, and vice versa for downward sloping beds in which the flow force is enhanced by the gravity. For a slope in the direction of the flow, Schiereck [2001] gives a factor that accounts for the increase or reduction of the strength relative to a horizontal bed. The stabilizing force caused by the gravity on the stone ($\Delta g d^3$) can be multiplied with the factor to account for the effect of the slope, this factor is given in equation 2-26a for an upward slope and in 2-26b for a downward slope.

$$K(\beta_{up}) = \frac{\sin(\phi + \beta)}{\sin\phi} \tag{2-26a}$$

$$K(\beta_{down}) = \frac{\sin(\phi - \beta)}{\sin\phi} \tag{2-26b}$$

in which:

- β the angle of the bed in the direction of the flow [°]
- ϕ the angle of repose of a material [°]

The angle of repose is defined as the steepest angle relative to the horizontal plane to which a

material can be piled without sliding down.The value of the angle of repose for non-cohesive materials with different diameter d can be seen in figure 2-10.

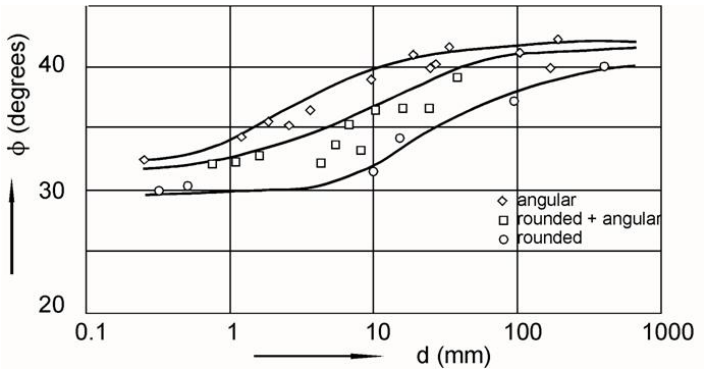

Figure 2-10 Angle of repose for non-cohesive materials (from Schiereck [2001])

2.3 Stone stability

In this section, the stability of stones covered with stones is discussed. The effect of certain flow conditions on the movement of stones is elaborated. In section 2.3.1 a number of existing stability parameters are discussed. In section 2.3.2 two methods on how to relate these parameters to the stability of stones will be explained. Finally, in section 2.3.3 a number of existing stability relations will be given.

2.3.1 Stability parameters

In engineering practice, the stability of a stone bed is examined using a stability parameter. The dimensionless stability parameter is the ratio between the destabilizing forces due to the flow and the resisting forces due to gravity or due to surrounding stones. The destabilizing forces are usually written in terms of the velocity. Equation 2-27 gives the most general form of the stability parameter (see Hofland [2005]).

$$\Psi_{tot} \equiv \frac{\left(C_b(\bar{\tilde{u}}+\tilde{u}')+C_m(\bar{\tilde{a}}+\tilde{a}')d\right)_{max}}{\Delta g d} \tag{2-27}$$

With:

- C_b the combined drag and lift coefficient [-]
- C_m the added mass coefficient [-]
- $\tilde{u}$ the velocity in the vicinity of the stone [m s^{-1}]
- $\tilde{a}$ the acceleration in the vicinity of the stone [m s^{-2}]
- d the stone diameter

One of the first relations for stability is expressed by Izbash (see Schiereck [2001]). Izbash used some critical velocity above the bed to express the force on the stones, although he is not clear in his description of this velocity The probably most well-known stability parameter is developed by Shields [1936], in which the bed shear stress is used as the indicator of the force that is exerted on the bed by the flow. Later, stability parameters with a more plausible physical background have been developed by Jongeling et al. [2003], Hofland [2005] and Hoan [2008]. In these stability parameters, the effect of turbulence is incorporated more explicitly.

In the next sections the following stability parameters are discussed to get an idea about the applicability and disadvantages of each of them:

- The Shields stability parameter Ψ_S;
- The Dessens stability parameter Ψ_{MS};
- The Jongeling et al. stability parameter Ψ_{WL};
- The Hofland stability parameter Ψ_{Lm};
- The Hoan stability parameter $\Psi_{u-\sigma[u]}$.

Shields parameter

The Shields parameter is based on the assumption that the stability of a stone on the bed is determined by the bed shear stress τ_b as the load and the submerged weight as the resisting force. The Shields parameter is formulated as:

$$\Psi_S = \frac{\tau_b}{(\rho_s - \rho_w)gd} = \frac{u_{\tau c}^2}{\Delta g d} = f(Re_*) = f\left(\frac{u_{\tau c} d}{\upsilon}\right) \tag{2-28}$$

With:

τ_b the bed stress [N m^{-1}]
$u_{\tau c}$ a critical friction velocity [m s^{-1}
Δ the relative density ($\Delta = (\rho_s - \rho_w)/\rho_s$) [-]

It has been shown in both practice and experiments (see Hofland [2005]) that turbulence plays an important role in the stability of stones. Increased turbulence is generally taken into account by means of an influence factor K_v. For many different structures and situations the increased turbulence can be calculated (with emperical relations), resulting in a wide range of influence factors for turbulence, lacking general validity. The K_v factor acts as a multiplier of the current velocity u. When the mean velocity u is zero, this indicates that there can be no damage in this case. However, there are situations with a mean velocity of zero but with large turbulence intensities (e.g. the reattachement point behind a sill of backward-facing step). It is evident that the damage here could be severe and that this factor does not include the nature of turbulence correctly. Other non-uniform phenomena are also included by means of influence factors. Because the factors are determined for a specific flow case, they are not generally applicable. Therefore, for every new scenario the factor has to be derived again.

The Dessens stability parameter

Dessens [2004] gives a stability parameter for the entrainment in which the depth-averaged velocity and the depth-averaged acceleration are included (see also section 2.4.2 further in this report). Equation 2-29 gives the definition of the stability parameter.

$$\Psi_{MS} = \frac{\frac{1}{2}C_{\text{b}}\overline{u}_{da}^2 + C_{\text{m}} d \overline{a}_{da}}{\Delta g d} \tag{2-29}$$

With:

C_{b} = 0.10
C_{m} = 3.92

The C_{b} and C_{m} are found by investigating different combinations of velocities and accelerations. Combinations with approximately equalt velocity but different acceleration are used to find the influence of acceleration on the movement of stones. The effect of the turbulence is included by correction factors just like with in the Shields parameter.

The Jongeling stability parameter

In Jongeling et al. [2003] a method is developed that takes the turbulence into account more explicitly, using the turbulent kinetic energy. In this way, the output of a numerical RANS model can be used to estimate the stability of stones on the bed. The flow force that causes movement of stones is a combination of velocity and turbulence in this method. In this way the peak values of the velocities are used. The formulation of the stability parameter is given in equation 2-30

$$\Psi_{WL} = \frac{\left\langle \left(\overline{u} + \alpha\sqrt{k} \right)^2 \right\rangle_{hm}}{\Delta g d} \tag{2-30}$$

With:

α	an emperical turbulence magnification factor [-]
$\langle \ldots \rangle_{hm}$	the spatial average over a distance h_m above the bed
hm	a certain height above the bed that has influence in the bed ($hm = 5d + 0.2h$) [-]

α and hm are determined, together with the critical value of Ψ_{WL}, based on the threshold of motion concept. Experiments are done at incipient conditions for different flow configurations (e.g. flow over a short and long sill or under a gate). The measured velocity and turbulence intensities are measured and used to calculate the stability parameter with varying α and hm. The values of α and hm that gave approximately equal Ψ_{WL} for incipient motion in all geometries is used, which resulted in $\alpha = 6.0$ and $hm = 5d + 0.2h$.

Hoan [2008] states that the method of choosing α and hm is questionable because there is no proof that the critical stability parameter has to be a constant value (in other words, there is no specific situation above which movement suddenly occurs). Also, Jongeling et al. [2003] used a rather subjective definition of incipient motion, which will not lead to consistent design criteria. However, in Hoan [2008] the parameters α and hm again are determined, using very detailed measurements and this time with the stone transport instead of the incipient motion. This led to an estimated value of $\alpha = 3.5$ instead of $\alpha = 6.0$. In Hoan [2008] it is concluded that the Jongeling parameter quantified the forces on a bed sufficiently well.

The Hofland stability parameter

In Hofland [2005], a stability parameter is proposed based on his findings about the physical mechanisms governing the entrainment of coarse particles. The properties of turbulence that are responsible for instabilities of the bed protection are tried to be incorporated in the formulation stability parameter. Again, the velocity and the turbulent kinetic energy are used in this parameter. Therefore, the output of numerical RANS models can again be used to calculate the stability parameter.

The basic assumption behind the Hofland stability parameter is that the large-scale velocity fluctuations can reach the bottom via an eddying motion, as shown in figure 2-11. Here, the large-scale velocity fluctuations at height z are proportional to the square root of the turbulent kinetic energy $\sqrt{k}$ and have a horizontal length scale L_H. The fluctuations are part of a large rolling structure so that the 'maximum velocity' at the bed can be determined from the velocities from the entire water column above the bed.

The maximum of the local instantaneous velocity $(\overline{u} + \alpha\sqrt{k})$ is weighted with the relative mixing length Lm/z, since it is likely that the turbulent sources higher in water column have less influence on the bed. Further, Hofland [2005] argues that if a large-scale structure exists at a certain

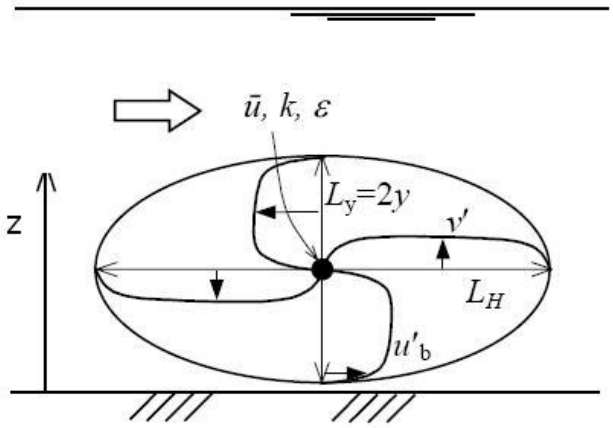

Figure 2-11 Model of a large-scale eddy that causes forces on the stones on the bed. From Hofland [2005]

height z, it will influence the turbulence intensities at all places surrounding this point between a distance with a maximum of half its length scale away. To estimate the large-scale intensity at z the moving average with varying filter length L_m is taken, denoted as $\langle \ldots \rangle_{L_m}$. The length scale L_m is the well known Bahkmetev mixing length distribution (see Uijttewaal [2011]). This is defined as $L_m = \kappa z\sqrt{1-z/h}$. The method is shown schematically in figure 2-12 and the stability parameter is given in equation 2-31.

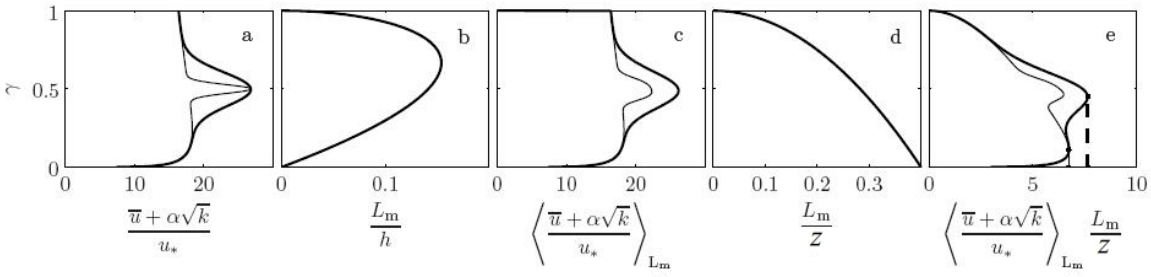

Figure 2-12 Distribution of key parameters in the Hofland stability parameter: vertical 'maximum velocity' distributing (a), Bahkmetev mixing length (b), estimate of the large-scale 'maximum' velocity (c), the weighting function L_m/y (d) and the estimated influence of large scale turbulence on the bed with the vertical line indicating the two maximum values (e)

$$\Psi_{\mathrm{Lm}} = \frac{\max\left[\left\langle \overline{u}+\alpha\sqrt{k}\right\rangle_{l_m}\frac{l_m}{z}\right]^2}{\Delta g d} \tag{2-31}$$

Hofland [2005] found a correlation between the Hofland stability parameter and the bed damage, in form of an entrainment rate, based on the data of Jongeling et al. [2006] and De Gunst [1999]. This also led to the conclusion that the best collapse of the data is obtained with $\alpha = 6.0$. However, Hoan [2008] applied the Hofland stability parameter to his own data measured in a local contraction and found a value for α of 3.0.

The use of information from the entire water column seems strange, since the stability of stones is caused by the near-bed velocities. However, Hofland [2005] gives some important arguments in favor of this approach. RANS models usually use wall functions in which the near bed value is $k \propto u_\tau^2$ (see also 3.1.3). Using this value in the stability parameter would effectively lead to

the Shields parameter. The value of k in the grid point nearest to the bed leads to a trivial answer and would not lead to the explicitly modelling of turbulence. In this case situations with low velocity but high turbulence intensity lead to underestimation of the damage. Hofland [2005] also states that from k, the exact shape of a probability distribution for the velocity fluctuations is unknown since k only describes the second order moment (statistical quantity describing the shape of a probability distribution) of the velocity fluctuations. Velocities from higher up in the water column can give rise to higher-order moments of the near-bed velocity fluctuations. A large length-scale at a certain elevation implies that turbulent structures from that level have a larger chance of reaching the bed sporadically. Although these fluctuations only happen once in a while, they do increase the probability of extreme forces although they do not change the intensity (which is the second order moment of u'). Velocities at higher levels can thus be used to determine the higher order moments of the near-bed velocity fluctuations. A disadvantage that could not be avoided by using this method is the fact that when k is known, the ratios $\sigma(u_x)^2$: $\sigma(u_y)^2$: $\sigma(u_z)^2$ are still unknown. However, from the it is still decided that using values from higher in the water column is a plausible approach.

The Hoan stability parameter

Hoan [2008] proposed a new stability parameter, dependent on the velocity and the standard deviation of the velocity $\sigma_u x$. Therefore, this relation can not be estimated with the output of a RANS model but only with the output from LES models. In this stability parameter, the maximum extreme force on the bed is estimated by:

$$F_{max} \propto \rho[\overline{u} + \alpha\sigma(u)]^2 d^2 \tag{2-32}$$

where $\sigma(u) = \sqrt{\overline{u'^2}}$ and α is a turbulence magnification factory (comparable the one in Jongeling et al. [2003] and Hofland [2005]). Just like in the Hofland stability parameter it is assumed that the turbulence sources near the bed have a larger influence than the sources higher up in the water column. Therefore, again a weighting function (depending on z) over a water column of height H is used. Finally. the force acting to move the stone is averaged, which leads (after dividing by the resisting force) to the following stability parameter:

$$\Psi_{u-\sigma(u)} = \frac{\left\langle \left[u + \alpha\sigma(u) \times \left(1 - \frac{z}{H}\right)^{\beta} \right] \right\rangle_H}{\Delta g d} \tag{2-33}$$

α, β and H are determined using a correlation analysis with the experiments of Hoan [2008]. The best correlation with the measurement data is reached when $\alpha = 3.0$, $\beta = 0.7$ and $H = 0.7h$ are used. The above is summarized in figure 2-13.

2.3.2 Methods for stone stability assessment

In section 2.3.1 different stability parameters are evaluated. To use them for stability calculations, they should be related to the bed response. Two methods that are used in practice will be discussed. First, there is the so-called threshold of motion in which it is assumed that there is a certain value of the stability parameter above which movement occurs. Next to this, there is the stone transport approach. Here, a certain value of the stability parameter is coupled to the bulk transport of stones from the bed.

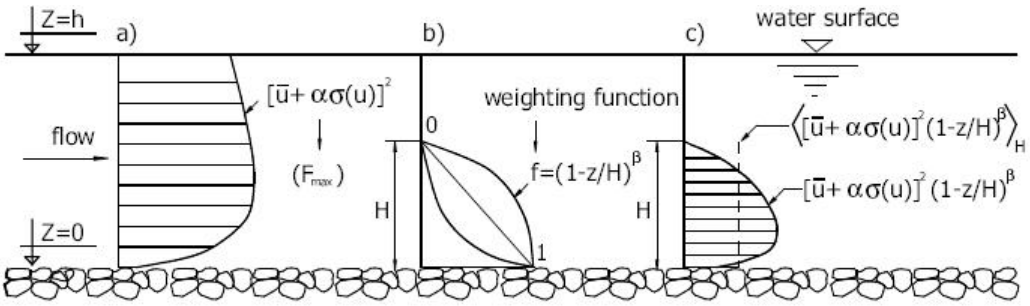

Figure 2-13 Distribution of key parameters in the Hoan stability parameter: extreme force distribution (a), a weighting function (b) and the weighted average of the extreme forces (c)

The threshold of motion concept

In the threshold of motion concept it is assumed that there is a condition where incipient motion occurs. When this condition is exceeded, stones start to move. This most famous stability relations that used the threshold of motion concept are Shields [1936] and Izbash [1935]. Here, a critical value of the stability parameter is derived from measurements. In the design in practice the nominal stone diameter is chosen such that this critical stability parameter is not exceeded. The condition at which the threshold of motion occurs, is rather subjective since the movement of stones can be interpreted in different ways. To give a more objective definition of the threshold of motion, DHL [1969] defined 7 transport stages:

0. no movement at all
1. occasional movement at some locations
2. frequent movement at some locations
3. frequent movement at several locations
4. frequent movement at many locations
5. frequent movement at all locations
6. continuous movement at all locations
7. general transport of the grains

The criterion that Shields [1936] used appeared to fit stage 6 from DHL [1969]. In Schiereck [2001] it is stated that there does not exist such thing as a critical condition. Due to the irregularities of natural stones the position, the protrusion and hence the exposure and stability is different for every stone in the bed. Next to this is there a irregular deviation from the mean value of the velocities because of the turbulence. Therefore, it can be said that one threshold of motion for the entire bed does not exist. The threshold of motion concept gives no information about the damage to the bed when the critical stability parameter is exceeded.

The stone transport concept

Next to the threshold of motion concept that is discussed in the previous section, the bed response can also be expressed in terms of stone transport. Here, the flow forces acting on the bed (as a stability parameter Ψ) are linked to the bed response (as the dimensionless transport indicator Φ). The main advantage of the stone transport concept is that it gives information on how the bed behaves after the stones become unstable (i.e. a transport rate). This method is applied widely for sediment transport and the general form can be written as in equation 2-34.

$$\Phi = f(\Psi) \tag{2-34}$$

With:

Φ the dimensionless transport parameter[-]
Ψ the dimensionless stability parameter [-]

The dimensionless transport parameter Φ should represent the damage to the bed properly. In Mosselman [1998] two ways of defining the transport of particles are distinguished:

1. The (volume) entrainment rate: the number of pick-ups per unit time and area (see equation 2-35).
2. The number of particles that is transported through a cross-section per unit time (see equation 2-36).

The time dependence is included because due to turbulent fluctuations a stone is moved sporadically and thus more stone are entrained during a longer time period. The (volume) entrainment rate is described by:

$$E = \frac{nd^3}{AT} \tag{2-35}$$

In which:

E the entrainment rate [ms^{-1}]
n the number of stones picked up [-]
d the stone diameter [m]
A the surface area [m^2]
T the time [s]

The bed load transport is described as:

$$q_s = \frac{nd^3}{BT} \tag{2-36}$$

With:

n the number of stones passing a cross-section[-]
B the width of the cross-section [m]

The dimensionless entrainment rate Φ_E and bed load transport Φ_q can be obtained as in equation 2-37a and 2-37b respectively.

$$\Phi_E = \frac{E}{\sqrt{\Delta g d}} \tag{2-37a}$$

$$\Phi_q = \frac{q_s}{\sqrt{\Delta g d^3}} \tag{2-37b}$$

Both of the damage indicators mentioned above can be used to describe the bed response of bed protections of stone. However, Hoan [2008] states that because of the dependence of the bed load transport on upstream hydraulics (the stones passing a certain cross-section is a function of all the entrained stones upstream) the bed load transport is a non-local parameter. The stability parameter Ψ, however, is a local parameter (solely depending on local flow characteristics). If q_s is used, the relation between Ψ and Φ would be of local and non-local parameters which is only valid for uniform flow where the flow conditions do not change along the channel.

In Hofland [2005] it is stated that the entrainment rate is completely depended on local hydrodynamic parameters. Following this, it can be stated that the relation between Ψ and Φ is also valid for non-uniform flow.

In practice often an exponential relation is used to describe the relation between the dimensionless transport parameter Φ and the stability parameter Ψ. Mosselman [1998] describes the two types of relations which both will be discussed below.

Type 1 formula The type 1 formula is an exponential relation without the use of a critical stability parameter and has the form as in equation 2-39. The most well-known formula in this form is the one by Paintal [1971].

$$\Phi = a\Psi^b \tag{2-38}$$

Type 2 formula The type 2 relation does have a critical stability parameter, as shown in equation 2-39. Well-known formulas from this type are the ones from Meyer-Peter and Muller [1948] and van Rijn [1984].

$$\Phi = a(\Psi - \Psi_c)^b \tag{2-39}$$

In which:

Ψ_c a critical stability parameter defining the incipient motion state [-]

The second type is especially applicable when sediment transport levels are high and the stability parameter large. When this is the case, the advantage of the type 2 formula is that the transport parameter is less sensitive to the stability parameter than in the type 1 formula. However, stone transport (in contrast to sediment transport) is characterized by low mobility and thus a small stability parameter that is close to the critical stability parameter. Therefore, this type of formula is not physically applicable. By fitting a curve through data Hofland [2005] found a tentative relation between Φ and Ψ that had the form of the type 2 formula though.

2.3.3 Stabilty relations

In section 2.3.2 two ways of the assessment of stone stability will be discussed. In this section, a number of stability relations that have been derived in the past will be discussed. Respectively, the relations derived by Shields [1936], Paintal [1971], Dessens [2004] ,Jongeling et al. [2003], Hofland [2005] and Hoan [2008] will be given.

Shields

Shields developed a relation between his stability parameter Ψ_S (described in 2.3.1) and the bed response using the threshold of motion concept. In his experiment he searched for the value of the Shields parameter $\Psi_{S,c}$ at which stones started to move. When this critical value exceeded, the stones become unstable. In figure 2-14 two presentations of the critical Shields parameter are given, one in the classical form and the other after replacing Re_* by a dimensionless particle diameter d_* that is defined by $d_* = (\Delta g/\nu^2)^{1/3}$. For more information one is referred to Schiereck [2001].

In figure 2-14 it can be seen that the critical Shields parameter is dependent of the particle Reynolds number Re_*. Shields [1936] stated that when the Shields parameter exceeds the critical Shields parameter in the graph, the stones start to move. Van den Bos [2006] gives the three most prominent shortcomings of the Shields approach:

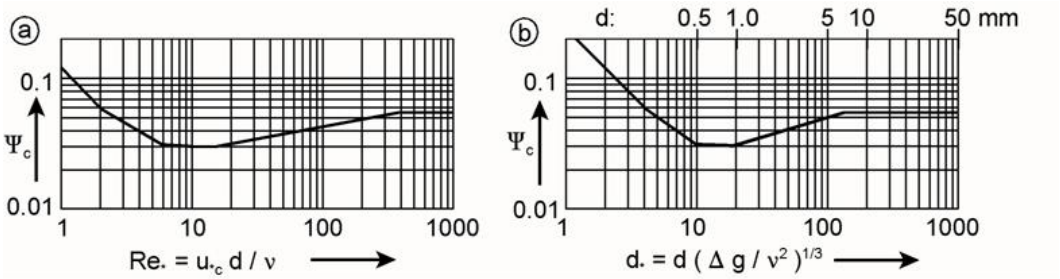

Figure 2-14 Critical shear stress according to Shields (a) and van Rijn (b) respectively

- The results of Shields are based on experiments with uniform flows. In this situation the flow is fully developed with a logarithmic velocity profile. These results are therefore not directly applicable to non-uniform situations like waves and accelerating or decelerating flow.
- An important assumption of Shields is the existence of a so called 'threshold of motion'. For stability parameters below a certain critical value the stones in the bed would not move at all. In reality stones do not show this kind of behaviour. Stones have been shown to move at any value of the Shields parameter, even when this is below the critical value. However, the mobility does increase with increasing Shields parameter, indicating that it is really a mobility parameter rather than a stability parameter.
- Shields set the forces that are proportional to the bottom shear stress as the mechanism that determines stone stability (including shear, drag and lift forces on the stones). This choice for the destabilizing mechanism is rather arbitrary since several other mechanisms that could have influence on the stability are omitted. There are indications that mechanisms such as inertia forces and turbulent flow structures do play an important role in destabilizing stones in a bed protection. This would suggest that the Shields theory is not based on a complete understanding of the destabilizing mechanisms.

Paintal

Paintal [1971] also defined a relation using the Shields parameter Ψ_S. However, he did not use the concept of the threshold of motion but he related the Shields parameter to the bed load transport q_s. In this way, he found the relation given in equation 2-40a. Because the smallest stones that are used in Paintal [1971] are not completely hydraulically rough, Mosselman [1998] adapted the relation to come to equation 2-40b.

$$\Phi_q = 6.56 \times 10^{18} \Psi_S^{16} \qquad \text{for } 0.02 < \Psi_S < 0.05 \qquad \text{(2-40a)}$$

$$\Phi_q = 3 \times 10^{7} \Psi_S^{8.9} \qquad \text{for } 0.02 < \Psi_S < 0.05 \qquad \text{(2-40b)}$$

In figure 2-15 the measurements from Paintal [1971] are shown together with equation 2-40a (dashed line) and 2-40a (solid line).

As already described in section 2.3.2, this relation is only valid for uniform flow because of the non-local character of the dimensionless bed load transport.

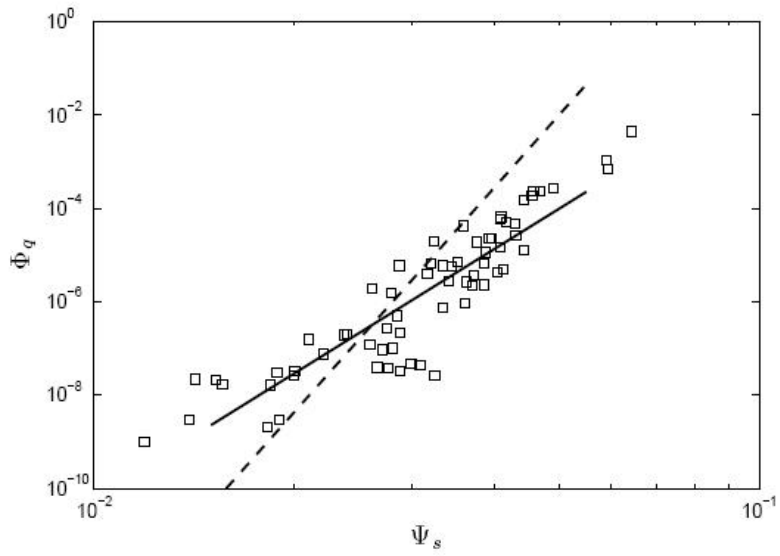

Figure 2-15 The relation between Φ_q and Ψ_S as given by Paintal [1971] (dashed line) and Mosselman [1998] (solid line)

Dessens

Equation 2-41 gives the relation between the stability parameter Ψ_{MS} found by Dessens [2004] and the dimensionless entrainment rate Φ_E.

$$\Phi_E = 6.0 \cdot 10^{-6} \Psi_{MS}^{4.73} \qquad 0.2 \leq \Psi_{MS} \leq 1.4 \tag{2-41}$$

This relation uses depth-averaged flow properties and the turbulence can be included by using correction factors. Figure 2-15 shows the relation and the measurement points from Dessens [2004].

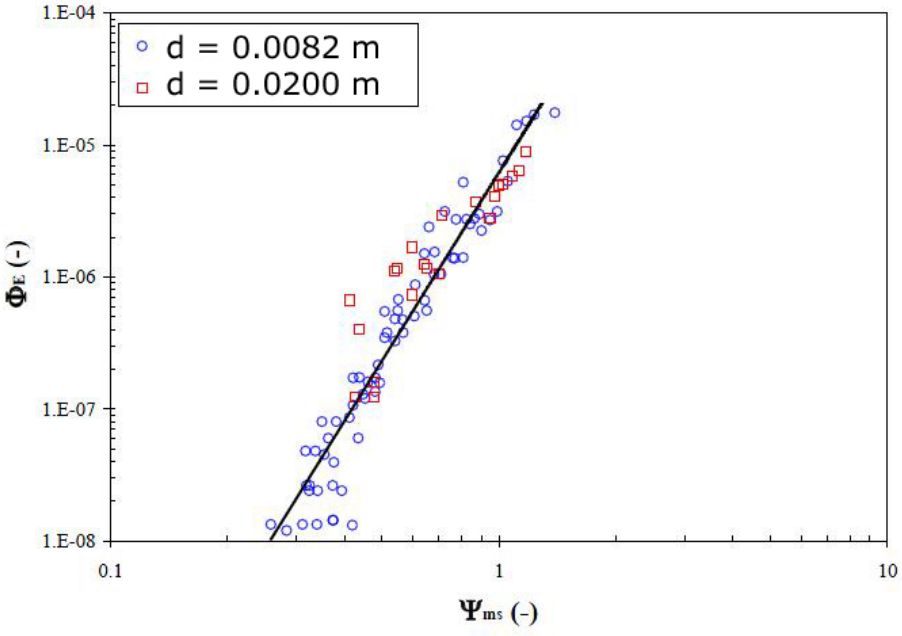

Figure 2-16 The relation between Φ_E and Ψ_{MS} as given by Dessens [2004]

Jongeling

Jongeling et al. [2003] related the Jongeling stability parameter Ψ_{WL} to the stability of stones using the concept of the threshold of motion. Again, a critical value of the stability parameter $\Psi_{WL,c}$ is defined. When this value is exceeded, the stones become unstable. Based on the output of a RANS model using a $k-\varepsilon$ turbulence model, Jongeling et al. [2003] found a value of $\Psi_{WL,c}$ ranging from 9 to 14. Jongeling et al. [2003] recommends a value of $\Psi_{WL,c} = 8$ in practice for designing bed protections.

Hofland

The Hofland stability parameter Ψ_{Lm} is related to the dimensionless entrainment rate Φ_E in Hofland [2005]. This is done by drawing a tentative power law as an upper envelope of the data points derived from the measurements of Jongeling et al. [2003] and De Gunst [1999]. This is shown in figure 2-17 and the relation is given in equation 2-42.

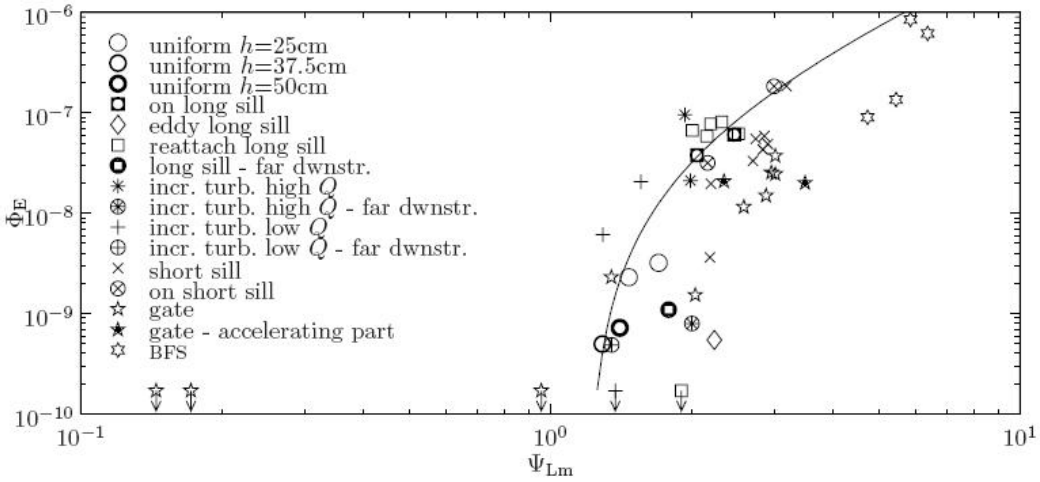

Figure 2-17 The relation between Φ_E and Ψ_{Lm} as given by Hofland [2005]

$$\Phi_E = \Phi_{E,0}\,(\Psi_{\text{Lm}} - \Psi_{Lm,c})^p \qquad \text{for } \Psi_{Lm,c} < \Psi_{\text{Lm}} < 7 \tag{2-42}$$

With:

$\Phi_{E,0}$	a coefficient [-]
$\Psi_{Lm,c}$	a threshold value [-]
p	a threshold value [-]

The data fitting with the Jongeling et al. [2003] data yielded the following values for the variables above:

$$\begin{aligned} \Phi_{E,0} &\approx 5 \cdot 10^{-8} \\ \Psi_{Lm,c} &\approx 1.2 \\ p &\approx 2 \end{aligned}$$

Hoan

Hoan [2008] used his measurements of a number of turbulence and velocity combinations to establish a relation between his stability parameter $\Psi_{u-\sigma[u]}$ and the dimensionless entrainment

rate Φ_E. This led to equation 2-43.

$$\Phi_E = 9.6 \times 10^{-12} \Psi_{u-\sigma[u]}^{4.25} \qquad \text{for } 7.5 < \Psi_{u-\sigma[u]} > 18 \tag{2-43}$$

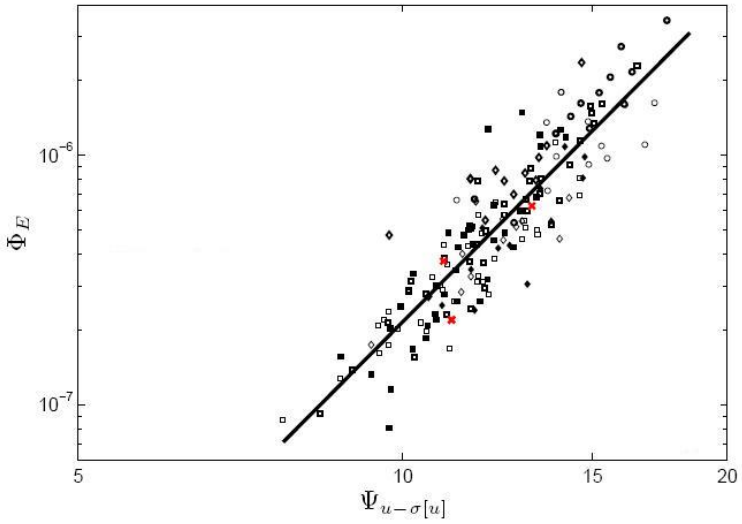

Figure 2-18 The relation between Φ_E and $\Psi_{u-\sigma[u]}$ as given by Hoan [2008]

Hoan [2008] also used his measurements to redefine the relation of the dimensionless entrainment rate Φ_E with the Jongeling parameter Ψ_{WL} and the Hofland parameter Ψ_{Lm}. This led to equations 2-44 and 2-45 respectively.

$$\Phi_E = 1.16 \times 10^{-12} \Psi_{WL}^{4.57} \qquad \text{for } 7.5 < \Psi_{WL} > 25 \tag{2-44}$$

$$\Phi_E = 1.90 \times 10^{-8} \Psi_{\text{Lm}}^{4.32} \qquad \text{for } 1.3 < \Psi_{\text{Lm}} > 3.2 \tag{2-45}$$

2.4 Data sets on stone stability

In this section, a number of experiments that are conducted in the investigation on stone stability are discussed. The experiments that will be discussed are the ones from Jongeling et al. [2003], Hoan [2008], Dessens [2004] and finally Huijsmans [2006]. The experimental set-up is given for each of the experiments, followed by an overview of the measured data.

2.4.1 Jongeling Data

In Jongeling et al. [2003] a relation is tried to be found between flow characteristics, the turbulent kinetic energy and the stability of stones at the bed. To do this, experiments are performed in which the flow and the associated bed response are measured in different situations. The measurements are used by Jongeling et al. [2003] to find the stability relation from section 2.3.3.

Experimental set-up

The measurements from Jongeling et al. [2003] are executed the Paul Kolkmangoot at WL|Delft Hydraulics. This is a flume with a rectangular cross-section with a width of 0.50 m and a height of 0.70 m. The flume is approximately 23 m long and the water that leaves the flume is pumped back to the inlet again via a pumping system. The side walls of the flume exists of a number of glass plates, placed in a frame of steel. The space between the different glass plates is 0.01 m and is filled with silicone. This connections causes a small disturbance in the flow and clearly observable irregularities in the water surface. At the downstream side of the flume, an adjustable gate is situated that can be used to adjust the downstream water level. The inflow and outflow section are made out of concrete and the first 2 to 3 meter behind the inflow section has steel side walls. A rail is located on top of the flume on which measurement instruments can be attached.

During the experiments, the bed of the first 13.6 m of the flume is covered with stones to let the flow adapt to the roughness. After this 13.6 m long adaption area, the measurement area starts. Here, the bed is covered with a 0.04 m thick layer of colored stones, in strips of 0.10 m. Looking in downstream direction the colors pink, yellow, green, red/orange, blue, brown and gray are applied, respectively. This sequence is repeated eight times. The goal of these strips is to determine how many stones have moved from a certain location and what distance these stones move. In the experiment, stones with a nominal diameter d_{n50} of 0.0062 m have been used with a density of 2716 kg/m^3. The goal of these strips is to determine the location where the stones move when they are entrained by the flow. The stones had a nominal diameter d_{n50} of 0.0062 m and a density of 2716 kg/m^3.

Measurements of velocities, waterlevels and discharge have been carried out in different types of configurations. Velocities and water levels are measured at different cross-sections, indicated with a dashed line in figure 2-19. In a certain cross-section, velocities are measured at different levels above the bed. The lowest measurement point in a vertical is 0.02 m above the bed and the total number of measurement points in vertical directions depends on the water level and configuration. The used configurations and the number of measurement points are:

- Flow over a flat bed with water depths of 0.50 m (10 points in z direction), 0.375 m (9 points in z direction) and 0.25 m (7 points in z direction). Measurements have been performed at 3 x locations. See configurations 1-3 in figure 2-19.
- Flow over a long sill with an upstream slope of 1:8 and a downstream slope of 1:3. Water depths of 0.375 (10 - 11 points in z direction) and 0.50 m (10 - 12 points in z direction) are used. Measurements have been performed at 10 x locations. See configuration 4 in figure 2-19.
- Flow over a flat bed. Extra turbulence is created using large stones upstream. The water depth is 0.25 m (7 points in z direction). Measurements have been performed at 3 x locations. See configuration 5-6 in figure 2-19.
- Flow over a short sill with an upstream and downstream slope of 1:8. Water depths of 0.375 (8 - 11 points in z direction) and 0.50 m (10 - 12 points in z direction) are used. Measurements have been performed at 10 x locations. See configuration 7 in figure 2-19.
- Flow under a gate. The opening had a height of 0.15 m and the upstream water depths that are used are 0.25 m (13 points in z direction) and 0.50 m (16 points in z direction). Measurements have been performed at 12 x locations. See configuration 7 in figure 2-19.

The measurement instruments that are used are summarized in table 2-4. Different instruments have been used for different flow directions. Here, the x direction is horizontal in the dominant

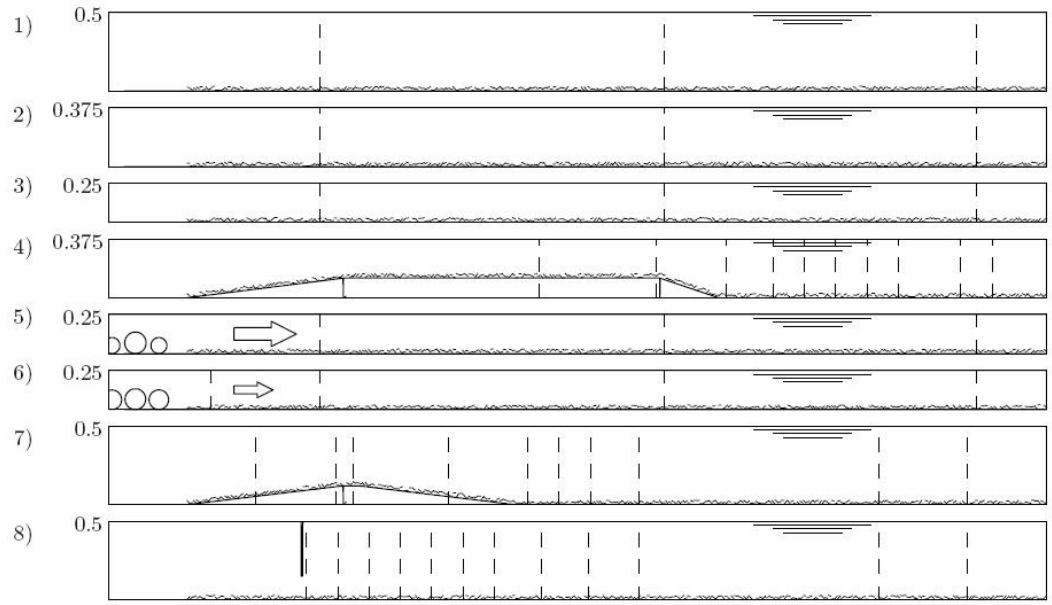

Figure 2-19 Longitudinal sections of the geometries used in Jongeling et al. [2003] with the measurement locations indicated with dashed lines

flow direction, the y direction is horizontal and perpendicular to the flow direction. The z direction is vertical and positive from the bed in upward direction. It should be noted that the LDA is not placed in the water and thus does not disturb the flow. The EMS, however, has been placed within the water creating a disturbance and reducing the accuracy.

Instrument	Measured quantity	Direction
Laser Doppler Velocimeter (LDA)	Flow velocity	x, z
Electromagnetic Flow Velocimeter (EMS)	Flow velocity	x, y
Wave gauge	Water level	z
Discharge meter	Discharge	x

Table 2-4 Used measurement instruments in Jongeling et al. [2003]

One measurement lasts 3 minutes per measurement point (at a certain x and z location) and the sample frequency is 100 Hz for both LDA [3] and EMS[4], which is enough to find the turbulent characteristics in a right way. The duration of the total experiment is in the order of 10 hour per configuration.

Next to the flow characteristics, also the bed response is measured. At the end of each experiment the number of stones that are moved from their strip of origin are counted. This could be done because the stones from each strip had a different color.

In table 2-5 the quantities that are measured in Jongeling et al. [2003] for a number of configurations are summarized.

2.4.2 Dessens Data

In Dessens [2004] the influence of the acceleration on the stability of stones has been investigated. This is done by doing measurements in a flume with a local contraction. The ratio between the effect of the depth-averaged velocity and the acceleration is derived using the threshold of motion together with the Morison equation. This is also used to derive a relation of the depth-

[3] Measurement instrument: Laser Doppler Anemometer
[4] Measurement instrument: Electromagnetic Velocity Meter

Quantity	Symbol
Mean velocity in x and z direction. Measured at different heights above the bed in different cross-sections with a LDA with sample frequency of 100 Hz.	u_x, u_z
Mean velocity in x and y direction. Measured at different heights above the bed in different cross-sections with an EMS with sample frequency of 100 Hz.	u_x, u_y
The discharge during each measurement.	Q
The water level at different locations.	h
The total number of dislocated stones per strip.	n
Total measuring period of each configuration.	T

Table 2-5 Quantities measured in Jongeling et al. [2003]

averaged flow quantities and the entrainment.

Experimental set-up

The experiments in this research are carried out in the Fluid Mechanics Labaratory of the department of Hydraulic Engineering of the Faculty of Civil Engineering at the Delft University of Technology. The flume that is used has a width of 0.50 m and a height of 0.70 m. The inlet section of the flume contains a flow stabilizer to reduce the turbulence, which is very turbulent when the water enters the flume. The discharge in the inlet and the water level at the outlet of the flume can be regulated. After passing the water level regulation gate at the outlet the water is discharged in a large water basin.

The bed of the flume is covered with stones for this experiment. Two different stone sizes have been used, one with a nominal diameter d_{n50} of 0.02 m, the other with a d_{n50} of 0.0082 m. Both stones had a density of approximately 2680 kg/m^3. In the last 0.40 m of the contraction the bed is covered with colored stones in strips of 0.10 m.

Two set-ups are used in this experiment. One set-up with a symmetrical contraction with a length of 1.50 m and another with a length of 2.00 m (see table 2-6).

	$L_{1.50}$	$L_{2.00}$
Length [m]	1.50	2.00
Width flume [m]	0.50	0.50
Width contraction [m]	0.15	0.15
Angle [°]	6.65°	5.00°

Table 2-6 Contractions used in Dessens [2004]

In the first part of the flume there is an approach section to let the flow stabilize. The contractions are constructed after this approach section by placing wolden plates in the flume. In figure 2-20 the experimental set-up is shown.

Velocity and water level measurements are performed at locations with different x-positions. At these locations, velocity measurements are done at 7 different heights above the bed. For the smalle stones (d_{n50} of 0.0082 m), the measurement point closest to the bed is approximately 0.025 m. For the large stones (d_{n50} of 0.02 m) this is slightly higher at approximately 0.04 m above the bed. All of the measurements are performed in the center of the flume, since the lateral velocities here are approximately zero. Measurements are performed for the following discharges and water levels:

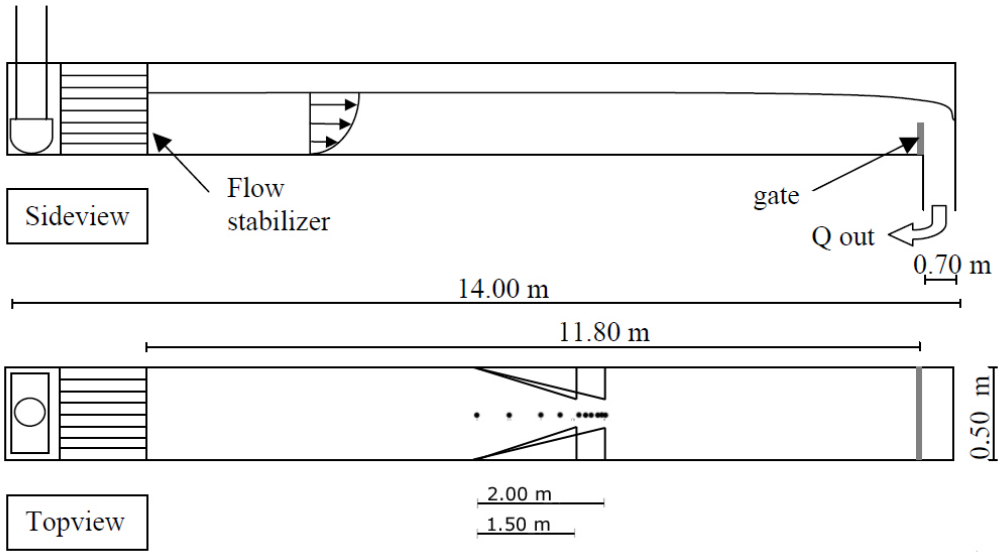

Figure 2-20 Side view and top view of the flume and geometries used in Dessens [2004]

Contraction Length	Discharge
1.50	0.03 m^3/s
1.50	0.05 m^3/s
1.50	0.06 m^3/s
2.00	0.03 m^3/s
2.00	0.04 m^3/s
2.00	0.06 m^3/s

The measurement instruments that are used in the experiment are given in table 2-7. Also, the measured quantities are indicated. An Electromagnetic Flow Velocimeter has been used to measure the velocities. The duration is 60 s for each measurement with a sample frequency of 50 Hz (which again is enough to catch all the turbulent characteristics). The locations of the measurements are indicated in the top view figure in 2-20. These locations are at the beginning and the end of strips of colored stones.

Instrument	Measured quantity	Direction
Electromagnetic Flow Velocimeter (EMS)	Flow velocity	x, y
Point gauge	Water level	z
Orifice plate	Discharge	x

Table 2-7 Used measurement instruments in Dessens [2004]

The bed response is measured again by counting the colored stones that moved from their strip of origin. In table 2-8 the quantities that are measured in Dessens [2004] for two contractions are summarized.

2.4.3 Huijsmans Data

The research done by Huijsmans [2006] is a continuation on the research done by Dessens [2004] discussed in the previous section. The influence of acceleration on the stability of stones is further investigated using the measurements of Dessens [2004] and by executing additional measurements. From the 7 stages of movement from DHL [1969], the Shields parameter associated with the observed movement of stones is derived. From here, the critical velocity is

Quantity	Symbol
Mean velocity in x and y direction. Derived from measurements at different heights above the bed in different cross-sections with a sample frequency of 50 Hz.	u_x, u_y
The discharge during each measurement.	Q
The water level at different locations in the contraction.	h
The total number of dislocated stones per strip.	n
Total measuring period of each configuration.	T

Table 2-8 Quantities measured in Dessens [2004]

calculated for which this amount of movement would occur in uniform flow conditions. This velocity is compared with the velocity measured in the experiments. A lower measured velocity indicates whether that the acceleration had an effect on the stability, which indeed is the case.

Experimental set-up

Measurements are done in the same flume as in Dessens [2004]. The same constrictions of 1.50 m and 2.00 m are used but a constriction with a length of 2.50 m is added. In Huijsmans [2006] only the stone with a nominal diameter of 0.0082 m is used, since the influence of the stone size is already investigated in Dessens [2004]. Again, the velocity is measured at different locations and heights above the bed. A number of discharges and water levels (and thus velocities and accelerations) are used. Strips of 0.10 m of colored stones have been used at the last 0.4 m of the contractions.

The obtained data is equal to the data that is obtained from the experiments in section 2.4.2.

2.4.4 Hoan Data

In Hoan [2008] the effect of increased turbulence on the stability of stones is investigated by conducting measurements in a gradually expanding open-channels in a laboratory flume. The turbulence intensities in such an expanding flow are higher. Three different expansions are used to create different combinations of velocity and turbulence. The bed response and the flow field are measured. The measurements are used for the derivation of the stability relation that discussed in section 2.3.3.

Experimental set-up

The measurements are executed in the same flume as in section 2.4.2 at the department of Hydraulic Engineering of the TU Delft. The flow in three different expansions is measured, these are given in table 2-9. The geometry of the experiment is shown in figure 2-21.

	Set-up 1	Set-up 2	Set-up 3
Expansion length [m]	2.90	1.70	1.20
Width flume [m]	0.35	0.35	0.35
Width expansion [m]	0.50	0.50	0.50
Angle α [°]	3°	5°	7°

Table 2-9 Expansions used in Hoan [2008]

The bed is covered with normal stones with a density of 2700 kg/m^3 and a nominal diameter d_{n50} of 0.008 m. However, the flow during the experiments is too low to displace these natural stones. Therefore, two layers of uniformly colored strips of artificial light stones are placed before and along the expansion. The density of these stones range from 1320 to 1971 kg/m^3 and

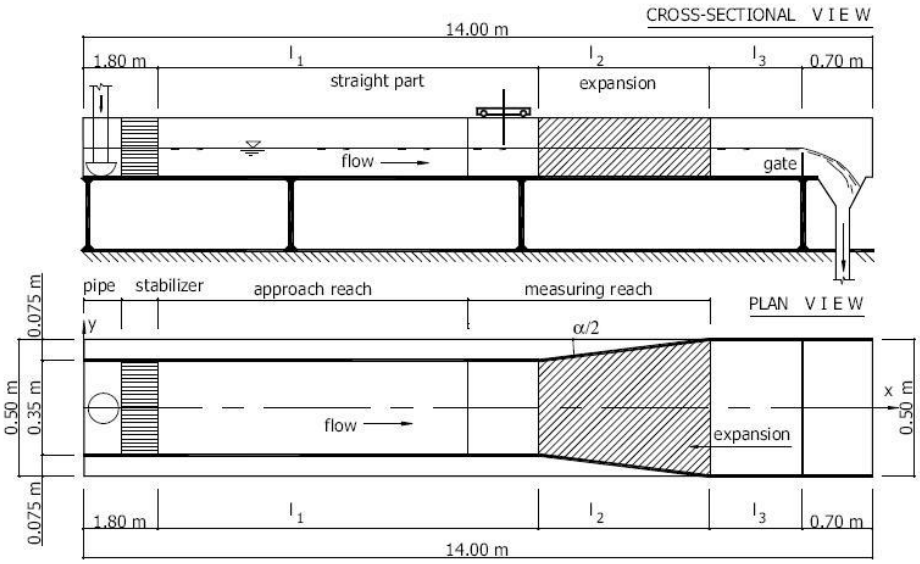

Figure 2-21 Side view and top of of the flume and geometry used in Hoan [2008]

the nominal diameter d_{n50} is 0.0082 m. The shape of the stones is comparable to the naturlas stones The strips had a length of 0.10 m in stream wise direction and a width of 0.20 m perpendicular to the flow direction. The placement of the stones can be seen in figure 2-22.

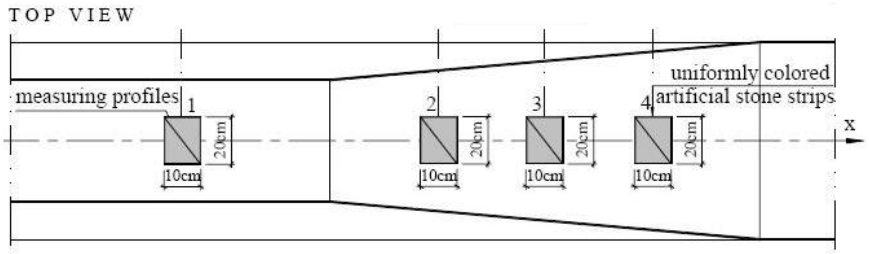

Figure 2-22 Placement of colored stones in Hoan [2008]

The measurement instruments that are used in Hoan [2008] are shown in table 2-10. Velocity measurements are done at x locations before and along the expansions. The x locations match with the center of the strips with colored stones as in figure 2-22. The number of measurement points in a vertical is rather accurate and ranged from 18 to 25 measurement points with a water depth in the order of $0.10 - 0.20$ m.

The velocity in x and z direction are done with a LDA. Each time series lasted 2 minutes with an sample frequency of 500 Hz. Next to this,an EMS is used to measure the velocities in x and y direction. Again, the EMS has the disadvantage that it disturbs the flow being measured and that it can not measure velocities close to the bed. Therefore, the output is only used as a supplement to the LDA measurements. The EMS measurement lasted 1 minute per measurement point with a sampling frequency of 200 Hz. The movement of stones is measured by counting the number of stones that moved from the strip of origin

Instrument	Measured quantity	Direction
Laser Doppler Velocimeter (LDA)	Flow velocity	x, z
Electromagnetic Flow Velocimeter (EMS)	Flow velocity	x, y
Measurement needle	Water level	z
Orifice plate	Discharge	x

Table 2-10 Used measurement instruments in Hoan [2008]

In table 2-11 the quantities that are measured in Hoan [2008] for three contractions with a variety of hydraulic conditions are summarized.

Quantity	Symbol
Mean velocity in x and z direction. Measured at different heights above the bed in different cross-sections with a LDA with sample frequency of 500 Hz.	u_x, u_z
Mean velocity in x and$y$ direction. Measured at different heights above the bed in different cross-sections with an EMS with sample frequency of 200 Hz.	u_x, u_y
The discharge during each measurement.	Q
The water level at different locations.	h
The total number of dislocated stones per strip.	n
Total measuring period of each configuration.	T

Table 2-11 Quantities measured in Hoan [2008]

2.5 Summary and conclusions

From the theory that is given in this chapter, a number of conclusions can be given about the existing stone stability assessment methods. First, a summary of the existing stability parameters is given and the way they incorporate the different forces acting on the stone. Secondly, the way the stability relation is established is given. Also, the suitability (availability and accuracy) of the existing data sets for the improvement of the stone stability assessment method is discussed. Finally, the aim for the rest of the report is given in the concluding remarks, based on the conclusions from this chapter.

2.5.1 Stability parameters

Section 2.2 describes the forces that work on a single stone are given. Table summarizes 2-12 these forces.

Force	Function of
Quasi-steady (drag and lift) forces (QSF)	$\overline{u}$ u'
Steady acceleration induced forces	$\overline{a}$
Time dependent acceleration (du/dt) (e.g. TWP or waves)	a'

Table 2-12 Summary forces acting on a stone

That stability parameters that are given in section 2.3.1 (Ψ_S, Ψ_{WL}, Ψ_{Lm} and $\Psi_{u-\sigma[u]}$) all have their own way of incorporating (some of) the different forces from table 2-12. In table 2-13 a summary is given on the way the parameters include the different forces.

From table 2-13 it is obvious that none of the mentioned parameters take into account the forces caused by advective acceleration or the turbulent wall pressure. A way to predict the bed

Ψ	QSF	Steady acceleration forces	TWP
Ψ_S	Takes into account the depth-averaged mean velocity. Velocity fluctuations are taken into account by multiplying the depth-averaged mean velocity with a correction factor K_v.	-	-
Ψ_{WL} and Ψ_{Lm}	Both the mean and the fluctuating part of the velocity are taken into account explicitly. Here, the velocity profile over the depth is used. The velocity fluctuations are taken as a function of the turbulent kinetic energy k.	-	-
$\Psi_{u-\sigma[u]}$	Both the mean and the fluctuating part of the velocity are taken into account explicitly. Again, the velocity profile over the depth is used. The velocity fluctuations are taken as a function of the standard deviation of the velocity $\sigma(u)$.	-	-

Table 2-13 Summary mentioned stability parameters and the way all the forces are included

response to forces caused by the flow of water more accurately is to include the forces caused by acceleration (steady and TWP) to the stability parameter.

2.5.2 Stability relations

In section 2.3.2 and 2.3.3 different ways of assessing the stability of stones is given. In figure 2-23 this is summarized.

In the previous sections it is already mentioned that the threshold of motion has a couple of disadvantages. First, the threshold of motion is rather subjective. Secondly, it has been shown that a threshold of motion does not really exist. Finally, the stability formulation based on the threshold of motion do not give information about the bed response once the stones have become unstable. The stone transport approach is physically more realistic and gives a cause-and-effect relation between flow parameters and bed response. Therefore, it can be used to predict the bed response as function of time which could lead to less conservative designs and the possibility to design maintenance programs. The damage could be expressed using the (dimensionless) entrainment rate and the bed load transport. Since the bed load transport parameter is a non-local parameter, this can only be used for uniform flow. For non-uniform flow the entrainment rate is a better quantity to express the bed response, since it is a local parameter and is directly related to the local flow conditions. In practice, two types of formulas are used to describe the movement of particles. One without using a critical value (type 1 formula) and one with using a critical value (type 2 formula). Although the latter has the advantage that the bed response is less sensitive of the stability parameter, it is especially applicable for high transport rates. Considering the above, the best way to describe the damage to bed protections of stone is to use the stone transport concept. The flow characteristics are related to the entrainment using a exponential relation of the form $\Phi = a\Psi^b$.

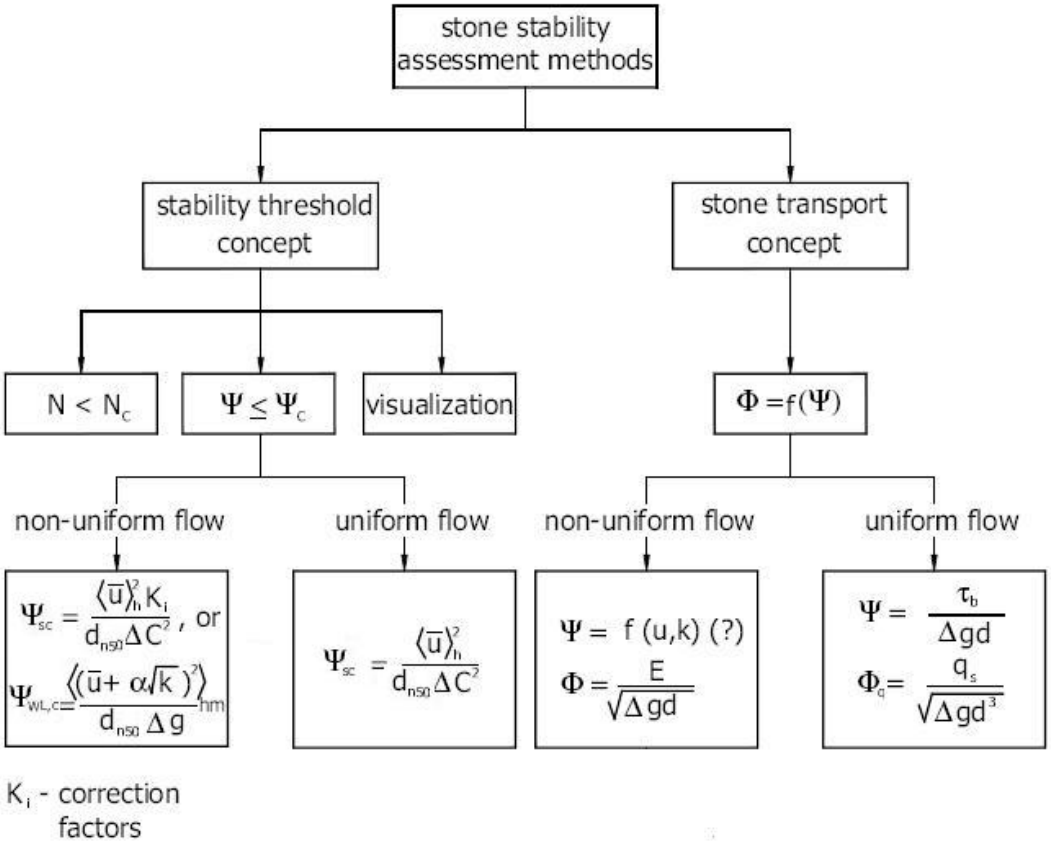

Figure 2-23 Summary of the different stone stability assessment methods (from Hoan [2008])

2.5.3 Data sets

The data that can be obtained from the experiments described in section 2.4 is summarized in table 2-14. It gives the number of useful measurement profiles. One measurement here means a certain combination of the vertical distribution of $\bar{u}$, k or $\bar{a}$ together with measurements of the bed response (the number of stones that moved from a strip). In the last column, the possibility to use the data set for deriving different variables is evaluated.

Name	Cases	Measured variables	Number of useful measurements	Possibility use or derive variable
Jongeling et al. [2003]	• Flow over a flat bed • Flow over a short sill • Flow over a long sill • Flow under a gate	• Velocity: u_x, u_z (LDA) • Velocity: u_x, u_y (EMS) • Water level: h • Discharge: Q • Number of moved stones: n	41 profiles	$\overline{u}$: Yes k: Yes $\overline{a}$: No Φ_E: Yes
Dessens [2004]	Accelerating flow through a local contraction	• Velocity: u_x, u_y (EMS) • Water level: h • Discharge: Q • Number of moved stones: n	32 profiles	$\overline{u}$: Yes k: Yes $\overline{a}$: Yes Φ_E: Yes
Huijsmans [2006]	Accelerating flow through a local contraction	• Velocity: u_x, u_y (EMS) • Water level: h • Discharge: Q • Number of moved stones: n	42 profiles	$\overline{u}$: Yes k: Yes $\overline{a}$: Yes Φ_E: Yes
Hoan [2008]	Decelerating flow through a local expansion	• Velocity: u_x, u_z (LDA) • Velocity: u_x, u_y (EMS) • Water level: h • Discharge: Q • Number of moved stones: n	132 profiles	$\overline{u}$: Yes k: Yes $\overline{a}$: Yes Φ_E: Yes

Table 2-14 Summary of the data sets and their applicability for the formulation of the new stability parameter

In the last column of table 2-14 it can be seen that all of the variables are present (or can be calculated) in the measurements from Dessens [2004], Huijsmans [2006] and Hoan [2008]. The bed-response is measured by counting the stones that have moved from this strip. This means that the variables that are used for the stability calculations need to representative for that strip.

The velocity profiles in Dessens [2004] and Huijsmans [2006] are measured at the beginning and end of 4 strips, resulting in 5 velocity profiles with a horizontal distance between them of 0.10 m. To get the velocity measurements that are representative for the strip, assumptions need to be done on the velocities in the strip, since only the extremities are measured. The velocity measurements are performed only in x and y direction with an EMS. Therefore, this data set does not contain information on the velocities (and thus the turbulence intensities) in the z direction. This is required to calculate the turbulent kinetic energy, so assumptions have to be made on this part too. Finally, since the velocities at the extremities of the strip are known, the mean acceleration (in x direction) can be calculated using this data. It should be noted that because an EMS is used, the minimal height above the bed where measurements could be performed is somewhat higher than in the case a LDS is used.

The measurements in Hoan [2008] are performed in the center of the strips with colored stones. The measurements are performed in x and z direction with an LDS and an EMS is used to measure the x and y direction. Information of the flow velocities is directly available from the measurements. The horizontal distance between the measurement locations varied from 0.40 m to 2.10 m, so the measurements can not be used to calculate the acceleration (or in this case, deceleration) that occurred over a certain strip with enough accuracy. However, Hoan [2008] also modeled his flow situations numerically using the Delft incompressible flow solver, formerly known as ISNaS (Information System for Navier-Stokes equations) with $k-\varepsilon$ closure. In his report it is stated that this reproduced the velocities with reasonable accuracy. Therefore, instead of using the measurements, the output of this numerical model is used to calculate the acceleration that occurred over the length of the strip.

The data set from Jongeling et al. [2003] have, just like in Hoan [2008], been performed in the center of the strips with colored stones in x and z direction with a LDS and in x and y with an EMS. The information on flow velocities and turbulence can be used directly for the stability calculations. However, the experiments have been performed to investigate the influence of turbulence on the stability of stones. Therefore, the measurements are only located in decelerating, high turbulent, parts of the flow. Also the horizontal distance between the measurement points is rather large, making the calculation of the acceleration belonging to a certain strip not possible from these data. The accelerating parts of the flow do not contain measurements, although the number of moved stones are measured there. In Jongeling et al. [2003] the experiments also have been modelled in the numerical simulation package CFX of AEA Technology, using a RANS model with k - ε turbulence closure. The output of this model is only given for the measurement locations.

2.5.4 Concluding remarks

In the above it is found that none of the existing stability parameters take into account the acceleration ($\overline{a}$ nor a'). Since it is found in multiple experiments that this does have a influence on stability, the existing methods of stone stability assessment can be made more physically based by incorporating these effects. Acceleration can be divided into two types, i.e. steady spatial acceleration and time-dependent acceleration. The last one can be caused by large scale time dependent phenomena (e.g. waves, inlet of water or bow-thruster induced flow) or by small scale turbulent structures (i.e. TWP). The incorporation of the effects of TWP would require a very high level of understanding of the phenomenon and very accurate measurements are needed. This is outside the scope of this research.

Including the effects of time-dependent acceleration would mean that the time-dependent response of the bed should be considered. The velocity profile should be known over time together with the instantaneous bed-response. Tromp [2004] did this and derived a Morison-like equation. However, this will not be included in this thesis. The remainder of this report will focus only on the incorporation of the effects of the steady spatial acceleration into the stability parameter.

The conventional methods of numericall modelling turbulence in flow are Large Eddy Simulations (LES) or Reynolds-averaging (RANS). The computation times in LES calculations can be quite substantial. Therefore, the possibility to use the output of RANS simulations in the stability parameter is desired. Because of this reason, the Hoan stability parameter $\Psi_{u-\sigma[u]}$ will not be used. RANS models only give a value for k and not for $\sigma(u_x)$, which is required in the Hoan stability parameter. It is chosen to expand the Hofland stability parameter Ψ_{Lm} because this parameter has a clear physical basis and because the turbulence is incorporated explicitly. The relation between the flow characteristics, expressed as Ψ, and the bed response, expressed as Φ, should be of type 1 as given in section 2.3.3.

From the data sets, the ones from Dessens [2004], Huijsmans [2006] and Hoan [2008] can (with some assumptions) directly be used for the derivation of a new stability parameter that includes the acceleration. The data set from Jongeling et al. [2003] showed not to be sufficient for this. One possibility is to omit the data set of Jongeling et al. [2003], but it is desired that diverse situations are used in the determination of the new stability relation. Therefore it is not chosen to omit the data set but to complement the dataset by modelling some of the flow situations numerically. How this is done will be described in chapter 3.

This chapter is concluded with a summary of the goal of the remainder of this report:

Finding a relation between the forces on the bed caused by the flow and the bed response. The forces on the bed are expressed as a dimensionless stability parameter Ψ which is a function of the mean velocity $\overline{u}$, the velocity fluctuation u' ($\propto \sqrt{(k)}$) and the steady spatial acceleration $\overline{a}$. The bed response is expressed as the dimensionless entrainment rate Φ_E. The flow forces and the bed response will be related using an exponential relation of the form $\Phi = a\Psi^b$.

3 Numerical Modelling

This chapter deals with the numerical modelling of a number of flow situations from Jongeling et al. [2003]. The modelling is done with the open source numerical software package OpenFOAM. In section 3.1, a theoretical basis is given on numerical modelling. In section 3.2, the modelling approach is given, after which each of the cases is elaborated. For detailed information on the OpenFOAM case structure and settings, one is referred to appendix C.

3.1 Background on numerical modelling

Section 3.1.1 gives a general background on numerical modelling. Subsequently, the choice of the method of turbulent closure in this thesis is discussed. Finally, the near-wall and free surface treatment are discussed in section 3.1.3 and 3.1.4 respectively.

3.1.1 Computational models

In engineering practice the real world gets often approximated by mathematical models using simplifying assumptions. Mathematical equations are used as a simplified description of physical phenomena. In this way, real world phenomena are mapped to a continuous abstract number space (see also Zijlema [2012]). This space is structured by mathematical notions as continuity and differentiability. Examples of this kind of mathematical equations are conservation laws (e.g. mass, momentum, energy) and examples of simplifying assumptions in hydraulics are the hydrostatic pressure assumption or turbulence modelling and Reynolds-averaging (as discussed in section 2.1.1).

Often the boundary values problems can not be solved analytically, particularly when nonlinear terms are included. This is the moment when the methods from the field of numerical mathematics are introduced. Numerical mathematics is the study of the methods of numerically approximating solutions of mathematical equations with finite computational processes.(Vuik et al. [2006]). The continuous abstract number space of the mathematical model is then projected on a discrete space or grid containing a finite number of grid points. In this space the notions continuity and differentiability do not exist, and functions are represented as a series of samples in the discrete space and differential equations are replaced by recurrent relations.

There is a large number of numerical techniques available to approximate mathematical models, often being tedious and repetitive arithmetic. This makes computers an excellent help for this kind of calculations. Examples of methods to discretize (partial) differential equations in time, space and combinations of that are given in table 3-1 with a brief description. For more detailed explanations one is referred to Zijlema [2012] or Vuik et al. [2006].

Method	Scheme
In time ($u = f(t)$):	
Explicit (forward) Euler	$\frac{du}{dt} \approx \frac{y^{n+1} - y^n}{\Delta t} = f(y^n)$
Implicit (backward) Euler	$\frac{du}{dt} \approx \frac{y^{n+1} - y^n}{\Delta t} = f(y^{n+1})$
Crank-Nicolson (trapezoidal)	$\frac{du}{dt} \approx \frac{y^{n+1} - y^n}{\Delta t} = \frac{1}{2} f(y^n) + \frac{1}{2} f(y^{n+1})$
Midpoint rule	$\frac{du}{dt} \approx \frac{y^{n+1} - y^{n-1}}{2\Delta t} = f(y^n)$
BDF	$\frac{du}{dt} \approx \frac{3y^{n+1} - 4y^2 - y^{n-1}}{2\Delta t} = f(y^{n+1})$
In space ($u = f(x,t)$):	
Forward finite differences	$\frac{\partial u}{\partial x}(m\Delta x, t) = \frac{u_{m+1}(t) - u_m(t)}{\Delta x}$
Backward finite differences	$\frac{\partial u}{\partial x}(m\Delta x, t) = \frac{u_m(t) - u_{m-1}(t)}{\Delta x}$
Central differences	$\frac{\partial u}{\partial x}(m\Delta x, t) = \frac{u_{m+1}(t) - u_{m-1}(t)}{2\Delta x}$
Upwind differencee scheme	$\frac{\partial u}{\partial x}(m\Delta x, t) = \frac{u_m(t) - u_{m-1}(t)}{\Delta x}$ for $u > 0$
In space and time	
FTCS	Forward Euler in time and central differences in space
Leapfrog	Midpoint rule in time and central differences in space
FTBS	Forward Euler in time and space
Preissmann	Trapezoidal in both space and time

Table 3-1 Examples of numerical schemes

The results from numerical models are only an approximation of the real solution since infinite operators from the mathematical equations (e.g. derivative and integrals) are calculated using only simple mathematical operators (i.e. addition, subtraction, division and multiplication). This discretization and the use of computers give rise to errors, the most well-known causes of errors are:

- **Truncation error:** some functions can be represented by an infinite Taylor series). This is approximated on computers by using a finite sum, leading to an error which is called the truncation error.
- **Round-off error:** computers do not calculate with infinite precision but use floating point numbers of fixed word length. Real values are represented by this number and information is lost by this rounding off.
- **Measurement error:** boundary conditions, bottom topography or empirical coefficients are usually used in numerical models. Errors in the measurements or assumptions that had to be made influence the model output and can be a source of errors.

Often the following requirements are imposed on numerical models:

- **Convergence:** when the $\Delta t \to 0$ or $\Delta x \to 0$ the scheme has to converge to the exact solution. A basic rule of thumb to proof convergence is *consistency* + *stability* $\Rightarrow$ *convergence*.
- **Consistency:** the truncation error goes to zero when $\Delta t \to 0$ or $\Delta x \to 0$.
- **Stability:** the error has to stay small when time evolves ($t \to \infty$).
- **CFL condition:** a necessary condition for the stability of numerically solving partial differential equations defined by $u\Delta t/\Delta x \leq C_{max}$. Here C_{max} is value that depends on the used numerical scheme.
- **Accuracy:** the error that s caused by the discrete representations of infinite operators can not be too large.
- **Computation time:** depending on the situation, the computation time has to stay within certain limits.

The Reynolds-averaged Navier-Stokes equations from section 2-3, together with the equations following from the turbulent closure is the set of equations that has to be computed numerically in this thesis. How this is done will be the subject of the remainder of this chapter.

3.1.2 The k-ω SST model

The method of turbulence closure in this thesis will be the $k-\omega$ SST turbulence model. This model is proposed by Menter [1994] and is an adaptation of the $k-\omega$ model by Wilcox [1993]. In the 'standard' $k-\omega$ model by Wilcox [1993], the turbulence is resolved using transports equations for the turbulent kinetic energy and for the large scale turbulent frequency (or specific turbulence dissipation rate). In Menter and Esch [2001] it is stated that the $k-\omega$ model has significant advantages near surfaces and accurately predicts the turbulent length scales in adverse pressure gradient flows. The model has a very simple analytical low-Re (low Reynolds number) formulation, which does not require additional non-linear wall damping terms and the correct sublayer behaviour is achieved through a Dirichlet boundary (a fixed value) of ω. In Menter and Esch [2001] it is stated that the sublayer behavior of the ω is in principle similar to using an elliptic relaxation equation (as in the V2F model of Parneix et al. [1999]).

Another advantage of the $k-\omega$ model is its robustness even for complex applications and the reduced mesh resolution demands near the wall. The main deficiency of the standard model, according to Menter and Esch [2001], is the strong sensitivy of the solution to free stream values for ω outside the boundary layer. To overcome this deficiency, Menter [1994] proposed a com-

bination of the $k-\omega$ model near the wall and the $k-\varepsilon$ model away from the wall, resulting in the $k-\omega$ SST (Shear Stress Transport) model. Although the method is initially developed for heat transfer simulations in aerodynamics it is also applicable beyond this field of study. The model combines the best elements of the $k-\varepsilon$ and $k-\omega$ models using a blending function that activates the $k-\omega$ in the near-wall region and the $k-\varepsilon$ in the rest of the flow.

Menter [1994] states that, in his experience, higher order turbulence models offer little advantage over well calibrated eddy-viscosity models (like the $k-\omega$ SST turbulence model). However, the eddy-viscosity does have to fulfill a number of requirements in order to capture the main characteristics of the boundary layer development. The most important of these requirements is that the model must be designed to avoid the build-up of turbulence in stagnation regions, which is frequently observed in standard two-equation models. To overcome this deficiency, Menter [1994] proposed a production limiter as a modification in the definition of the eddy viscosity of the standard formulation. Bardina et al. [1997] validated the $k-\omega$ SST model for a variety of cases and demonstrated the capability of the model to predict the separation under adverse pressure gradient conditions accurately.

The difference between the standard $k-\omega$ model by Wilcox [1993] is that the absolute value of the transport of shear stress (the strain rate) S is now used in the defitinition of the eddy viscosity instead of the vorticity. This eddy viscosity can be used in the RANS equations (see equation 2-3) to calculate the mean flow properties using the Boussinesq approximation. Transport equations of the turbulent kinetic energy k and the large scale turbulent frequency ω are given in equation 3-6 and 3-2.

$$\frac{\partial \rho k}{\partial t}+\frac{\partial \rho U_j k}{\partial x_j}=\tilde{P}_k-\beta^*\rho\omega k+\frac{\partial}{\partial x_j}\left[\frac{1}{\rho}\left(\nu+\frac{\nu_t}{\sigma_k}\right)\frac{\partial k}{\partial x_j}\right] \tag{3-1}$$

$$\frac{\partial \rho \omega}{\partial t}+\frac{\partial \rho U_j \omega}{\partial x_j}=\frac{\gamma}{\nu_t}-\beta\rho\omega^2+\frac{\partial}{\partial x_j}\left(\frac{1}{\rho}\left(\nu+\frac{\nu_t}{\sigma_\omega}\right)\frac{\partial \omega}{\partial x_j}\right)+2(1-F_1)\rho\sigma_{\omega 2}\frac{1}{\omega}\frac{\partial k}{\partial x_j}\frac{\partial \omega}{\partial x_j} \tag{3-2}$$

With:

$$P_k=\tau_{ij}\frac{\partial U_i}{\partial x_j} \tag{3-3a}$$

$$\tilde{P}_k=\min(P_k;c_1\beta^*k\omega) \tag{3-3b}$$

The Boussinesq equation is used and given in equation 3-4.

$$\tau_{ij}=-\rho\overline{u_i'u_j'}=\mu_t\left(2S_{ij}-\frac{2}{3}\frac{\partial u_k}{\partial x_k}\delta_{ij}\right)-\frac{2}{3}\rho k\delta_{ij}=\mu_t\left(\frac{\partial U_i}{\partial x_j}+\frac{\partial U_j}{\partial x_j}-\frac{2}{3}\frac{\partial U_k}{\partial x_k}\right)-\frac{2}{3}\rho k\delta_{ij} \tag{3-4}$$

With:

$$S_{ij}=\frac{1}{2}\left(\frac{\partial u_i}{\partial x_j}+\frac{\partial u_j}{\partial x_i}\right) \tag{3-5}$$

The eddy viscosity is calculated as shown in equation 3-6.

$$\mu_t = \rho \frac{a_1 k}{\max(a_1 \omega, SF_2)} \tag{3-6}$$

The values of the coefficients in the equations above (called φ) depend on the blending function F_1 (see equation 3-8a). The blending function F_1 has a value of 1 near surfaces (resulting in $\varphi = \varphi_1$) and a value of 0 in the outer part of the boundary layer and for free shear flows (resulting in $\varphi = \varphi_2$). The coefficients for φ_1 and φ_2 arge given in table 3-2.

$$\varphi = F_1 \varphi_1 + (1 - F_2)\varphi_2 \tag{3-7}$$

In which:

φ_1 the coefficients for the $k-\omega$ model
φ_2 the coefficients for the $k-\varepsilon$ model

Coefficient (φ_1)	Value	Coefficient (φ_2)	Value
σ_{k1}	1.17 6	σ_{k2}	1.000
$\sigma_{\omega 1}$	2.000	$\sigma_{\omega 2}$	1.168,
κ	0.41	κ	0.41
γ_1	0.5532	γ_2	0.4403
β_1	0.0750	β_2	0.0828
β^*	0.09	β^*	0.09
a_1	0.31	a_1	0.31

Table 3-2 The coefficients in the $k-\omega$ SST model

The blending function and its associated equations are defined in equation 3-8a to 3-8d.

$$F_1 = \tanh\left[\left(\min\left[\max\left(\frac{\sqrt{k}}{\beta^*\omega\gamma}, \frac{500\nu}{y^2\omega}\right), \frac{4\rho\sigma_{\omega 2}k}{CD_{k\omega}y^2}\right]\right)^4\right] \tag{3-8a}$$

$$CD_{k\omega} = \max\left(2\rho\sigma_{\omega 2}\frac{1}{\omega}\frac{\partial k}{\partial x_j}\frac{\partial \omega}{\partial x_j}, 1.0e^{-10}\right) \tag{3-8b}$$

(3-8c)

$$F_2 = \tanh\left[\left(\max\left[\frac{\sqrt{k}}{\beta^*\omega\gamma}; \frac{500\nu}{y^2\omega}\right]\right)^2\right] \tag{3-8d}$$

The equations mentioned in this paragraph combined with the Navier-Stokes equations in equation 2-3 leads to a set of equations. Together with the boundary and initial conditions they can be solved to describe the flow. Special attention goes to the treatment of flow close to the wall (section 3.1.3) and near the free surface (section 3.1.4).

3.1.3 Near-wall treatment

The flow at the wall can be treated in different way in numerical flow models (see Menter and Esch [2001]). The first option is to use a wall function, which bridges the viscous sublayer and uses the available knowledge in the logarithmic profile region of the boundary layer. Another option is integration to the surface using a low turbulent Reynolds number (low-Re) formulation.

The former allows the use of much coarser near-wall meshes resulting in shorter computation time (and thus costs). However, this also imposes limitations on the mesh generation process because the mesh height of the first cell has to be large enough to remain in the logarithmic part of the boundary layer. The disadvantage of wall functions is the fact that they ignore the influence of the viscous sublayer, which sometimes leads to significant errors in the solution. This disadvantage is not important for bed protections because the stones are in the rough wall regime and the effect of the viscous sublayer is negligible.

In Grotjans and Menter [1998] the above limitations are avoided by introducing a new approach of wall treatment by wall functions which is optimized ever since and is given in Menter [1994]. In this approach the model switches gradually from between a viscous (low-Re) sublayer formulation and wall functions, based on the mesh density. The way the wall function approach is implemented in OpenFOAM is described in the remainder of this section.

The logarithmic relation for the velocity in the log-law layer is described in table 2-1 and is repeated here for convenience:

$$u^+ = \frac{u_t}{u_\tau} = \frac{1}{\kappa}\ln(z^+) + A \tag{3-9}$$

$$z^+ = \frac{\Delta z u_\tau}{\nu} \tag{3-10}$$

$$u_\tau = \left(\frac{\tau_b}{\rho}\right)^{1/2} \tag{3-11}$$

in which:

- u_t the velocity tangent to the wall
- Δz the height of the center of the first cell close to the wall [m]
- A a log layer constant depending on the the wall roughness [m s^{-1}]

Equation 3-9 has two shortcomings (see also ANSYS, Inc. [2011]). First, in separation points where the near wall velocity approach zero the value of z^+ becomes 0 and u^+ becomes 1. To overcome this problem, an alternative velocity scale is introduced that is called u_* here and is given in equation 3-12. The main advantage of this way of determining u_* that it does not go to zero if the velocity goes to zero.

$$u_* = C_\mu^{1/4} k^{1/2} \tag{3-12}$$

The equation above can be used to obtain an explicit formulation for u_*, given in equation 3-13.

$$u_\tau = \frac{u_t}{\frac{1}{\kappa}\ln(z^*) + B} \tag{3-13}$$

with:

$$z^* = \frac{\rho u_* \Delta z}{\mu} \tag{3-14}$$

The absolute value of the shear stress can now be calculated as in equation 3-15.

$$\tau_b = \rho u_* u_\tau \tag{3-15}$$

Secondly, the log-law is used to express the near-wall velocity, this formulation is only valid when the center of the first cell is placed in the associated region ($30 > z^+ < 300$). This means that when a fine near-wall grid is used, the formulation is not applicable and the accuracy decreases. The extent of the log-law layer is quite large for high Reynolds number flows, but for low Reynolds number flows this extent is much smaller and therefore it becomes increasing difficult to place the first grid point in this region. This problem is avoided by limiting the lower value of z^* that is used in the equations above with a value of 11.06 which corresponds to the intersection between the logarithmic and linear near wall profile. This is displayed in equation 3-16. For grids where the limiter is activated, the relation between u^* and u_t becomes linear.

$$\tilde{z}^* = \max(z^*, 11.06) \tag{3-16}$$

The near-wall treatment that is discussed until now is only applicable for hydraulically smooth walls (see table 2-2). Since practically any situation in civil engineering has a rough surface, this should be included. As already discussed in 2.1.2 this can be done adding a certain roughness dependent value to the integration constant B. The value of this constant ΔB depends on the value of the dimensionless equivalent roughness height (k_s^+).

$$u_* = \frac{1}{\kappa} \ln(z_*) + B - \Delta B \tag{3-17}$$

With in OpenFOAM:

B 5.2 [-]

The effect of ΔB is shown in figure 3-1. A larger roughness leads to a greater value of ΔB and thus a smaller velocity near the wall. The roughness is included in OpenFOAM using the `nutRoughWallFunction` boundary condition. Here, OpenFOAM uses the rough law of the wall to calculate the turbulent viscosity ν_t near the wall. In OpenFOAM it is first checked whether the first cell height is placed within the logarithmic layer ($k_s > 90$). When this is the case, the value of ΔB is calculated using equation 3-18.

$$\Delta B = \frac{1}{\kappa} \ln(1 + C_s k_{s*}) \tag{3-18}$$

in which:

C_s the roughness constant to take into account the type of roughness (C_s can vary from 0.2 to 1)

OpenFOAM uses the rough law of the wall to compute the turbulent viscosity near the wall ν_t,

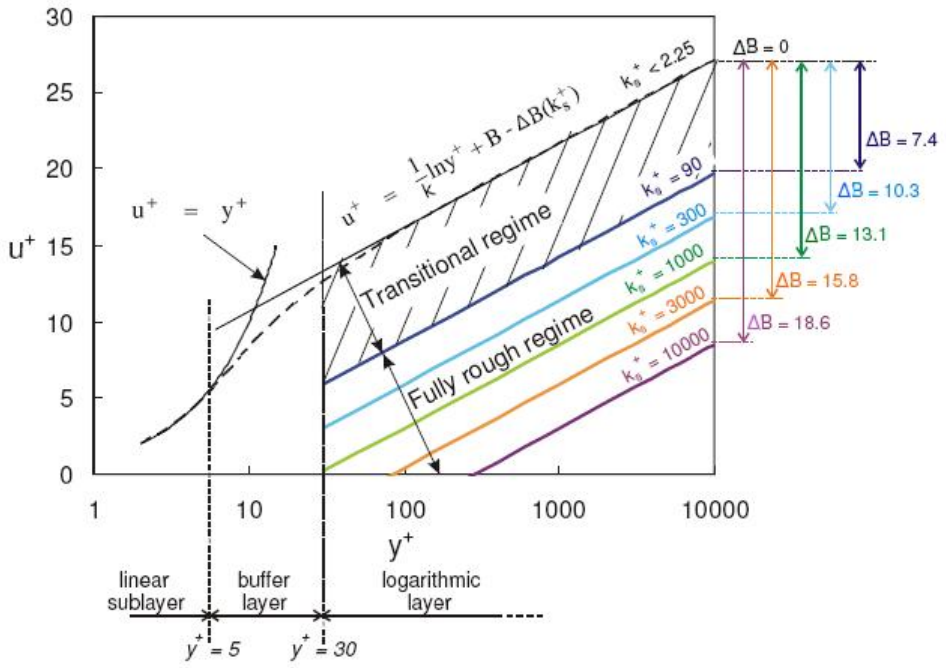

Figure 3-1 Roughness regions and the value of ΔB for a number of k_s^+ (from Martinez [2011])

the expression that is used can be seen in equation 3-19. This expression is derivated using the rough law of the wall, the definition of the bed shear stress $\tau_b = \rho u_{*k}^2$ and the definition from a linear interpolation of the shear stress $\tau_b = \rho(\nu_t + \nu)u/\Delta z)$

$$\mu_t = \mu \left(\frac{z_* \kappa}{\ln[(1 + C_s k_s^+) z_*]} - 1 \right) \tag{3-19}$$

In OpenFOAM, first the turbulent eddy viscosity ν_t is calculated. This value can subsequently be used to calcutate the turbulence production term P_k in the cell near the wall. The production term is calculated with the formulation of equation 3-20, based in equations 3-4 and 3-3a.

$$P_k = (\nu_t + \nu) \frac{\partial u_i}{\partial x_j} \cdot \frac{C_\nu^{1/4} \sqrt{k_p}}{\kappa \Delta z} \tag{3-20}$$

The production term P_k is used in the transport equation of k (equation 3-1). The final step is to calculate the ω_{tot} according to equation 3-21c. It is already mentioned that the wall function has to switch gradually from between a viscous (low-Re) sublayer formulation and wall functions, based on the mesh density. The solutions for ω in the linear and logarithmic near-wall region are given in 3-21a and 3-21b, respectively. It should be mentioned though that the viscous sublayer is lost very quickly for increasing roughnes and the influence of the viscous layer is very low for values of k_S^+ larger than 70. The equations for ω below can be implemented in OpenFOAM by

using the `omegaWallFunction` boundary condition for the bed.

$$\omega_{vis} = \frac{6\nu}{\beta_1 (\Delta z^*)^2} \tag{3-21a}$$

$$\omega_{log} = \frac{\sqrt{k}}{C_\mu^{1/4} \kappa z^*} \tag{3-21b}$$

$$\omega_{tot} = \sqrt{\omega_{vis}^2 + \omega_{log}^2} \tag{3-21c}$$

Finally, in Martinez [2011] it is mentioned that the velocity distributions in a sand grain rough wall that follow from using the rough law of the wall leads to velocity profiles corresponding the measurements when the height of the first cell is chosen such that $\Delta z > 0.2$. This is shown in figure 3-2. The value of C_s that is used in the OpenFOAM simulations is introduced to take into account the roughness type of the bed, and can vary from 0.2 to 1 and the default value in OpenFOAM is 0.5. No guidelines exist for this value.

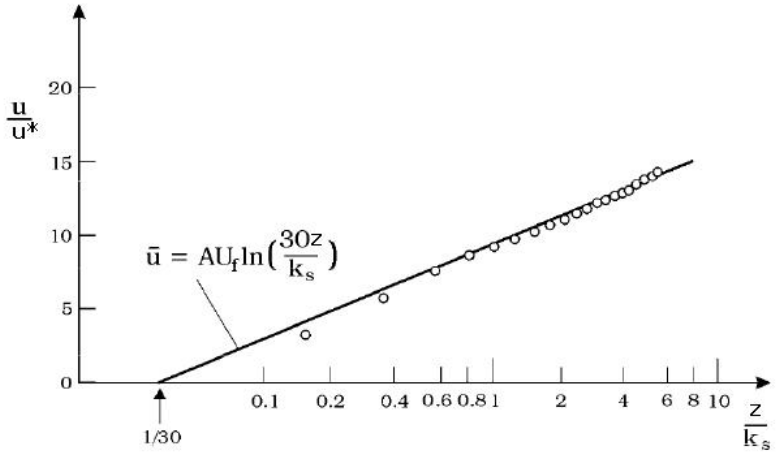

Figure 3-2 Roug law of the wall for sand grains compared with measurements (from Martinez [2011])

3.1.4 Free surface treatment

In the previous section, the treatment of the flow near the bed is discussed. Another important aspect of open-channel flow is the free surface. Some important findings about the nature of near surface turbulence are mentioned in Shi et al. [2000] and are:

- turbulent kinetic energy of vertical velocity fluctuations is redistributed to horizontal motion;
- the energy transfer from vertical to horizontal components is confined to relatively large eddy scales;
- the most important coherent structures are surface normal vortex tubes and vortex tubes with axes nearly parallel to the free surface. The first deform the free surface and the latter are flattened by the free surface;

As a first approximation Rodi [1980] suggests to model the free surface using a symmetry plane, also called a rigid lid (a frictionless wall at the surface of the flume). The presence of a shear layer at the free surface (caused by e.g. wind) is then modelled as a moving wall near the surface. This boundary condition is obtained by imposing a zero gradient normal to the surface for u_x, u_y, k, ω and p and a zero value for the velocity normal to the surface, u_z. These boundary conditions assume that the water surface is not deformed even by a net transport of momentum into the surface region (Hoohlo [1994]). Alfrink and van Rijn [1983] states that this assumption

is especially valid for flows with low Froude numbers Fr (dimensionless ratio between inertia and gravitational forces). Meselhe and Sotiropoulos [2000] found also reasonable results with a rigid-lid approximation for the free surface for moderate Froude numbers ($Fr \approx 0.3 - 0.6$).

$$Fr = \frac{\overline{u}}{\sqrt{gh}} \tag{3-22}$$

Rodi [1980] mentions that there is only very little known about the effects of the free surface on the turbulence in a water body, but that the effect appears to be similar to the effect walls have in the way that it also reduces the (vertical) length scale of turbulence. To account for this reduction of length scale, Rodi [1980] proposes the boundary conditions given in equation 3-23a for the dissipation ε (in the absence of a shear stress at the free surface). In equation 3-23b this is rewritten for the specific dissipation ω, using that $\omega = \varepsilon/(\beta \cdot k_{fs})$.

$$\varepsilon = \frac{(k_{fs} \cdot \sqrt{\beta^*})^{3/2}}{\kappa \left(\Delta z_{fs} + ah\right)} \tag{3-23a}$$

$$\omega = \frac{k_{fs}^{1/2}}{\beta^{*1/4} \cdot \kappa \left(\Delta z_{fs} + ah\right)} \tag{3-23b}$$

(3-23c)

in which:

k_{fs}	the value of k near the free surface
Δz_{fs}	the height of the first cell below the surface [m]
a	an empericial constant with the value 0.07 [-]
$u_{\tau S}$	the friction velocity at the free surface [m s^{-1}]

Using this boundary limits the length scale near the free surface (and increases ε) below the length scale that would yield from merely a symmetry condition. However, the equation is considered as only tentative. A second method to model the effects of the free surface is to use a two phase model that calculates the flow for two phases (both water and air). A well-known method to do this is the Volume Of Fluid (VOF) method. In this method an extra equation for the volume fraction α is used, which is defined in equation 3-24.

$$\alpha = \begin{cases} 0 & \text{for a volume totally occupied by air} \\ 1 & \text{for a volume totally occupied by water} \end{cases} \tag{3-24}$$

The values for the density and the viscosity are calculated using a blending function. The effect ofα is added to the RANS equations and an extra transport equation is added for α to solve the set of equations (see also Liu and Garcia [2008]).

$$\frac{\partial \alpha}{\partial t} + \nabla \cdot (U\alpha) = 0 \tag{3-25}$$

Contrary to the rigid lid approach, the VOF method can be used also in situations with rapidly changing water surfaces (e.g. waves and hydraulic jumps). However, a more refined at the free surface is required to catch the interface between water and air and to avoid oscillations. Also, numerical diffusion will spread out the interface between the two phases and to remain a sharp interface a artificial compression term (Higuera et al. [2013]) or a compressing difference

scheme (Liu and Garcia [2008]) has to be used.

3.2 Modelling considerations

All of the numerical modelling in this thesis (i.e. numerical approximations of the solutions of the RANS equations) is done using the open-source modelling tool OpenFOAM (Open Source Field Operation and Manipulation), version 1.6-ext. Appendix C gives detailed information on the OpenFOAM case structure, possible boundary conditions, solvers and other settings. In this section, some considerations on the way the flow will be modelled are discussed together with the choices that are made. The configurations of the experiments of Jongeling et al. [2003] are shown in figure 2-19. Because of the relatively large complexity of the flow under a gate and the problem that it is rather hard to make a stable accurate calculation, it is chosen to omit this case. The configurations that are modelled in this thesis are the flat bed (for validation and boundary condition set-up) and the flow over a short and long sill. The latter two are simulated because these are relevant real world examples of flow in which both acceleration and deceleration occurs.

Table 3-3 gives the Froude and Reynolds numbers for the modelled configurations. It can be seen that the Froude numbers vary from 0.3 to 0.6. Because all these Froude numbers are situated in the the moderate region that is mentioned in Meselhe and Sotiropoulos [2000] it is to use the rigid lid as free surface boundary. An other reason for choosing the rigid lid is that a stable solution is reached more easily when a rigid lid is used as opposed to two phase models.

Configuration	Q [m^3/s]	h_{max} [m]	u_{max} [m/s]	Fr [-]	Re [-]
Flat bed	0.168	0.495	0.679	0.308	340.000
Short sill	0.189	0.335	1.110	0.613	370.000
Long sill	0.166	0.376	0.883	0.460	330.000

Table 3-3 Froude numbers in the experiments of Jongeling et al. [2003]

The rigid lid boundary is discussed in section 3.1.4. The effect of the free surface can be incorporated by imposing a fixed value for ω at the upper boundary (equation 3-23b).

In the long sill configuration the measurements show that there is flow separation behind the sill. As already mentioned before, it has been demonstrated that the $k-\omega$ SST is able to predict the separation under adverse pressure gradient conditions accurately. Therefore, the $k-\omega$ SST is used in all of the following computations. The solver that will be used is the `pimpleFoam` solver, which is described in appendix C together with the associated settings in OpenFOAM. Also, to reduce calculation times, it is assumed that the flow is two-dimensional and does not vary in transversal direction. In Jongeling et al. [2003], it is found that this is not entirely true because the side walls seemed to have an influence on the flow. Because of the influence of the side walls the width of the flow is effectually narrowed, leading to higher velocities in the center of the flume and lower velocities at the sides (compared to the 2D velocity profile). This problem is accounted for by increasing the discharge in the model in the 2DV flow situation.

In the remaining sections of this chapter, the modelled cases are discussed. The flat bed simulation is discussed in section 3.3, the short sill in section 3.4 and finally the short sill in section 3.4. Each section contains information on the modelled geometry and flow conditions, the mesh, boundary conditions and a comparison with measurements. The following settings are used for all of the cases in the next sections:

Solver:	`pimpleFoam`
Turbulence model	`kOmegaSST`
Free surface	Rigid lid

3.3 Case 1: flat bed

The case that will be modelled in this section is the flow over a flat bed from Jongeling et al. [2003], as shown in figure 3-3. The experimental set-up is described in section 2.4.1, and a summary of the properties that are of importance for the numerical modelling are given in table 3-4.

Figure 3-3 The flat bed configuration that is modelled

Variable	Symbol	Value
Discharge	Q	0.168 m^3/s
Discharge per unit width	Q_w	0.336 m^2/s
Nominal diameter	D_{n50}	0.0062 m
Nikuradse roughness	k_s	0.0124 m - 0.0188 m
Water level in stagnant water	h_{st}	0.5 m
Water level in flowing water	h_{fl}	0.495 m
Viscosity (at 20 $^\circ$ C)	ν	$1 \cdot 10^{-6}$ m^2/s

Table 3-4 Values used in the flat bed experiment in Jongeling et al. [2003]

3.3.1 Mesh

A numerical mesh has to fulfill some requirements, e.g:

- Mesh independence: the solution has the be independent of the mesh;
- Height of the first cell: the height of the first cell has to be higher than $0.2 \cdot k_s$ (see chapter 3.1.3)
- Expansion factor and aspect ratio: increasing the expansion factor and aspect ratio leads to smaller computation times, however too large values of both leads to inaccurate description of the flow.

In appendix E the mesh convergence study is described from which a mesh for this configuration is the result. Here, only a description of the resulting mesh is given. The grid size gradually increases from the bottom to the top and the heighest cell is 3.5 times as large as the first cell. In table 3-5 and figure 3-4, the mesh characteristics are given. A vertical has been drawn in the figure for every 10 mesh cells in the model.

Variable	Symbol	Value
Cell length	Δx	0.2 m
Smallest cell height (at bed)	Δz_b	0.0083 m
Largest cell height (at surface)	Δz_s	0.012 m
Expansion rate in z-direction	$\Delta z_s / \Delta z_b$	1.42
Surface aspect ratio	$(\delta x / \delta z)$	16.67
Number of cells in x-direction	N_x	152
Number of cells in z-direction	N_z	50

Table 3-5 Mesh characteristics for the flat bed computations

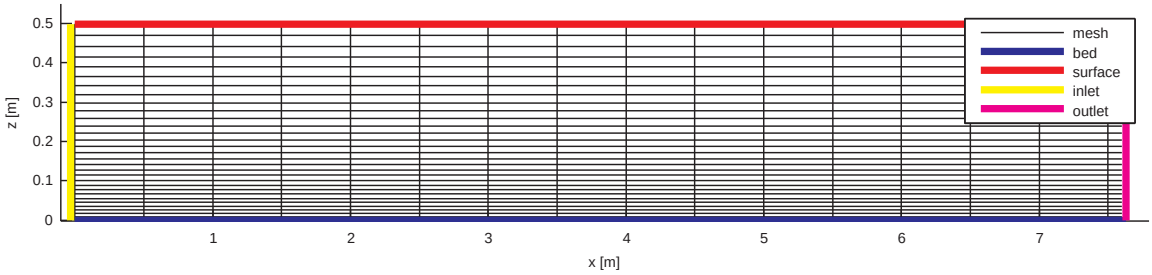

Figure 3-4 Mesh used for the flat bed computation

Boundary conditions

The boundary conditions that are used in this case are summarized in table 3-6. At the inlet boundary, a profile is imposed for `U`, `k` and `omega`. The derivation of these profiles can be found in appendix D. The outflow is modelled as free outflow boundary, i.e. `zeroGradient` for every variable.

The surface boundary value of ω is calculated with equation 3-23b. The value for k_{fs} is obtained using the measured value of k closest to the surface, which is $k = 0.00099$ kg $\cdot$ m^2/s^2. This leads to a value of $\omega_{fs} = 9.67$ s^{-1} at the surface boundary.

Boundary Conditions

Boundary	U	k	omega	p	nut
Inlet	Inlet profile	Inlet profile	Inlet profile	zeroGradient	zeroGradient
Outlet	zeroGradient	zeroGradient	zeroGradient	zeroGradient	zeroGradient
Bed	Uniform Value (0 0 0)	zeroGradient	omega-WallFunction	nutRough WallFunction Ks = 0.0093 Cs=0.5	zeroGradient
Surface	slip	zeroGradient	fixedValue 9.67	zeroGradient	calculated
Side Walls	empty	empty	empty	empty	empty

Table 3-6 Boundary conditions for the flat bed case

3.3.2 Validation

The settings described above are used in the computations using the `pimpleFoam` solver in OpenFOAM with a time step `deltaT` of 0.0001 s and simulation time of 200 s (which proved to be enough to reach an equilibrium). the results for the velocity `U` and the turbulent kinetic energy `k` are plotted in figures 3-5 and 3-6, respectively.

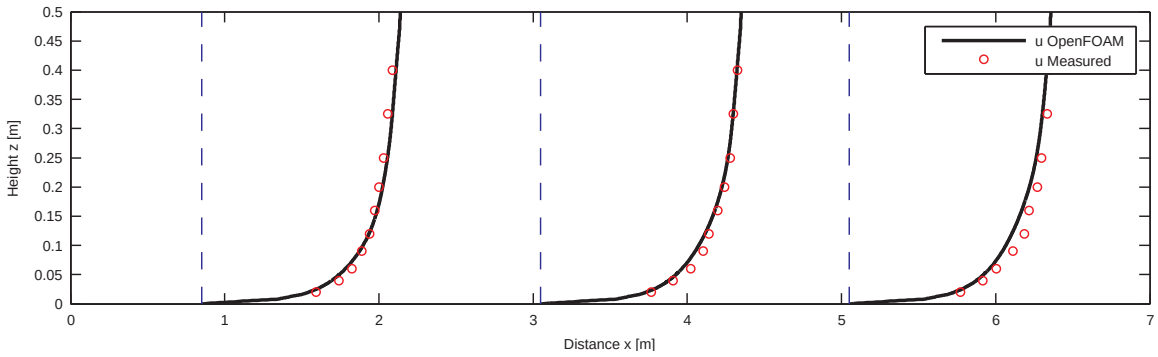

Figure 3-5 Velocity profiles from OpenFOAM and measurements of the flat bed experiments

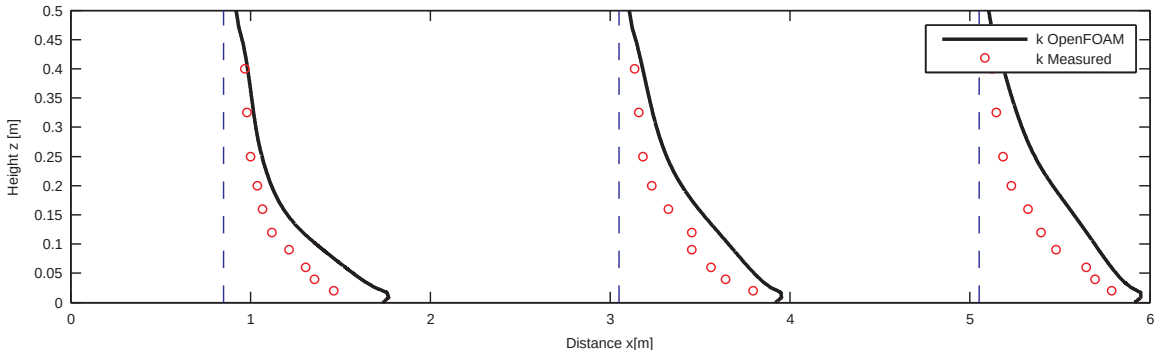

Figure 3-6 Turbulent kinetic energy profiles from OpenFOAM and measurements of the flat bed experiments

The computed OpenFOAM velocity profiles are very similar to the measured velocity profiles. The deviations of the model compared to the measurements are approximately 1.0 % higher in the water column and 5 % near the bed in the first profile. The turbulent kinetic energy profile differs significantly from the measurements and can be in the order of 30% in the first cross-section to almost 80% for the last cross-section.

In Jongeling et al. [2003] it is mentioned that the flume showed currents that are caused by 3D-effects because of the presence of the side walls. In Nezu [2005] it is also mentioned that secondary currents in rectangular cross-sections exist when the the ratio B/h is smaller than 5. The existence of these secondary currents can be the cause of the deviation of the 2D model from the measurements.

The modelled velocity profiles in the different cross-sections do not change over the length of the model domain, indicating that equilibrium is almost reached. The turbulent kinetic energy does change over the length of the domain to the same profile that can be expected based on the expression by Nezu [2005]. In appendix D it can be seen that it is observed that the velocity profile is still changing in the direction of the flow and that the turbulent kinetic energy profile deviated from the profile in an equilibrium situation. Both are arguments in favor of the hypothesis that 3D current patterns exist.

At this point there are two options, one is to model the entire domain in 3D and the other is to accept the error that is caused by this. The output of the model is used to calculate the acceleration over the long and short sill. In these cases it is expected that the effect of the geometry is dominant over the 3D effects caused by the side walls. Also, calculation times will be much larger when the 3D situation is modelled. Both of the arguments led to the decision to model the

other configurations also in 2DV.

3.4 Case 2: short sill

This section discusses the computations of the short sill configuration, shown in figure 3-7. The most important characteristics of the short sill experiment are given in table 3-7.

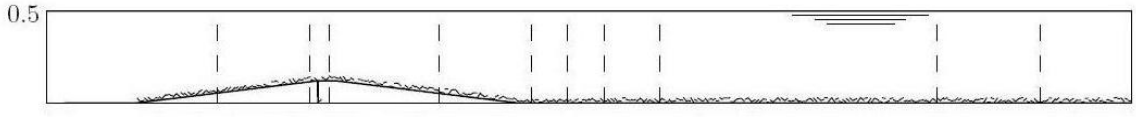

Figure 3-7 The short sill configuration that is modelled

Variable	Symbol	Value
Discharge	Q	0.1892 m^3/s
Discharge per unit width	Q_w	0.3784 m^2/s
Nominal diameter	D_{n50}	0.0062 m
Nikuradse roughness	k_s	0.0062 m - 0.0188 m
Water level in stagnant water	h_{st}	0.5 m
Water level in flowing water	h_{fl}	0.495 m
Viscosity (at 20 $^\circ$ C)	ν	$1 \cdot 10^{-6}$ m^2/s

Table 3-7 Values used in the short sill experiment in Jongeling et al. [2003]

3.4.1 Mesh

The geometry is added to the mesh using the `blockMesh` utility in OpenFOAM. The generation of the mesh is described in appendix E. The number of cells in vertical direction is 50 and a ratio between the cell near the bed and the cell near the surface is 1.42. From the boundary to the sill, the length of the cells in x direction gradually decrease from 0.05 to 0.01 m. Behind the sill, the cell length is gradually increased again from 0.01 m near the cell the 0.1 at the outflow boundary. The mesh characteristics are given in table 3-8 and the mesh is shown in figure 3-8. In the figure only every second z and every third x line are displayed.

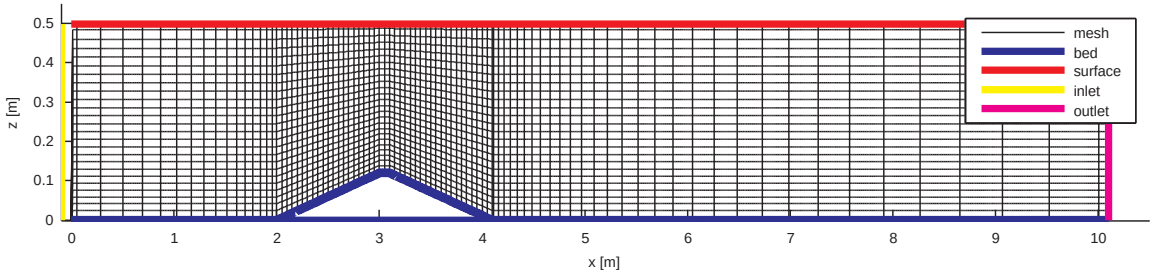

Figure 3-8 Mesh used for the short sill computations

3.4.2 Boundary conditions

The boundary conditions are the same as the boundary conditions for the flat bed computations from table 3-6, except for the inlet boundary. The higher discharge in the short sill experiment results in a higher velocity profile at the inflow boundary of these computations. The derivation of the inlet profiles is shown in appendix D.

Variable	Symbol	Value
Cell length	Δx	0.01 m - 0.10 m
Smallest cell height (at bed)	Δz_b	0.0083 m
Largest cell height (at surface)	Δz_s	0.012 m
Expansion rate in z-direction	$\Delta z_s / \Delta z_b$	1.42
Surface aspect ratio	$(\delta x / \delta z)$	1.0 - 9.0
Number of cells in x-direction	N_x	440
Number of cells in z-direction	N_z	50

Table 3-8 Mesh characteristics for the short sill computations

3.4.3 Validation

The results that followed from running the model with a time step `deltaT` of 0.0001 s and a simulation time of 200 s are shown in figure 3-9 and 3-10 for the velocity and the turbulent kinetic energy respectively.

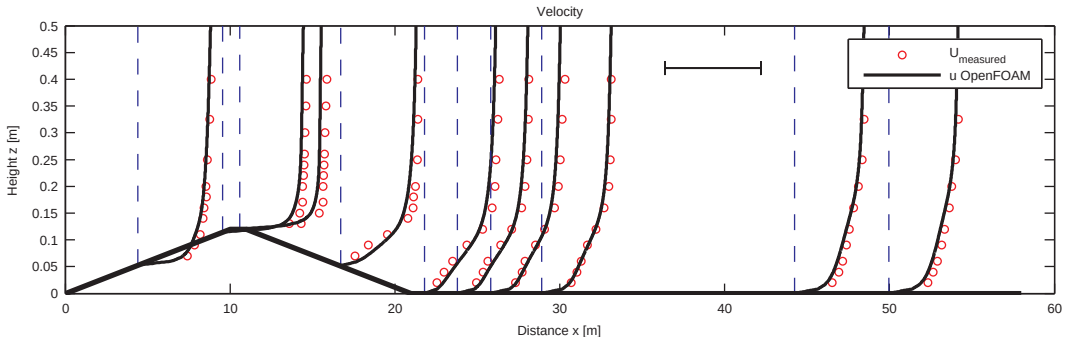

Figure 3-9 Velocity profiles from OpenFOAM and measurements from the short sill experiment (the scale for 1.0 m/s is indicated)

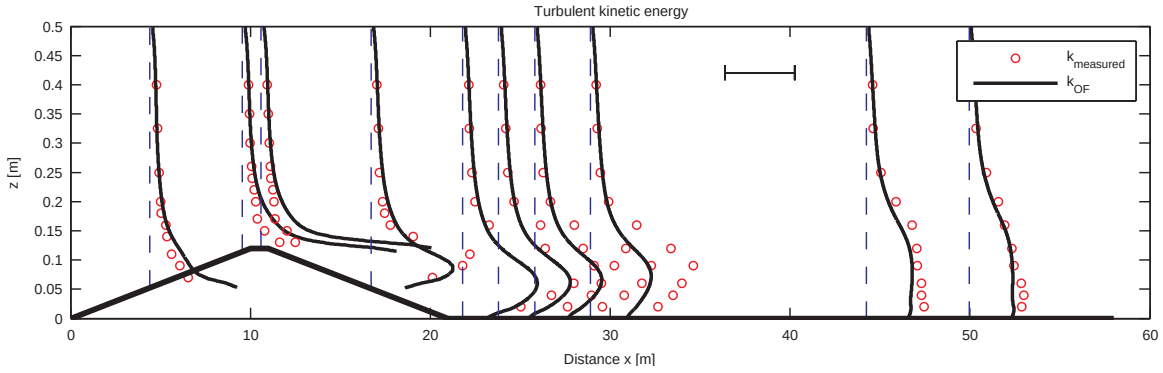

Figure 3-10 Turbulent kinetic energy profiles from OpenFOAM and measurements from the short sill experiment (the scale for 0.01 m^2/s^2 is indicated)

Figure 3-9 shows that OpenFOAM reproduces the velocities from the measurements really well. The errors in the velocity computations varied from 2% to 6% in most of the profiles. The velocities in the fourth and fifth profile in the figure showed a larger deviation near the bottom (in the order of 30 %), while in the upper parts of the vertical this error is only 6 %.

The turbulent kinetic energy profiles again show a larger deviation just like in the flat bed case. It seems like the turbulent kinetic energy on top of the sill is overestimated and that as a consequence of this, too much energy is dissipated on the crest of the sill leading to a smaller turbulent kinetic energy profile behind the short sill. The errors of the turbulent kinetic energy are

on average approximately 30 to 40 % but could reach up to 100 % at the crest of the sill. The error is very high. At the end of the chapter a choice is made whether this is still acceptable.

3.5 Case 3: long sill

Finally, the computations of the long sill configuration are discussed. The configuration is shown in figure 3-11 and the important values that are used in the experiments are given in table 3-9.

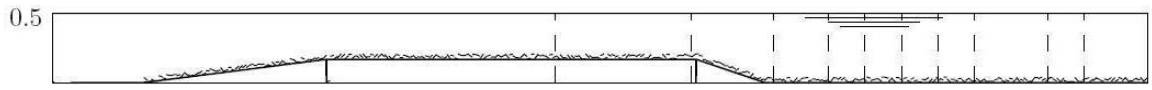

Figure 3-11 The short sill configuration that is modelled

634 cells

Variable	Symbol	Value
Discharge	Q	0.166 m^3/s
Discharge per unit width	Q_w	0.332 m^2/s
Nominal diameter	d_{n50}	0.0062 m
Nikuradse roughness	k_s	0.0062 m - 0.0188 m
Water level in stagnant water	h_{st}	0.5 m
Water level in flowing water	h_{fl}	0.495 m
Viscosity (at 20 ° C)	ν	$1 \cdot 10^{-6}$ m^2/s

Table 3-9 Values used in the long sill experiment in Jongeling et al. [2003]

3.5.1 Mesh

The mesh of the long sill is not that different from the short sill computations explained in the previous section. The same settings are used, except for the fact that the top of the sill is longer.

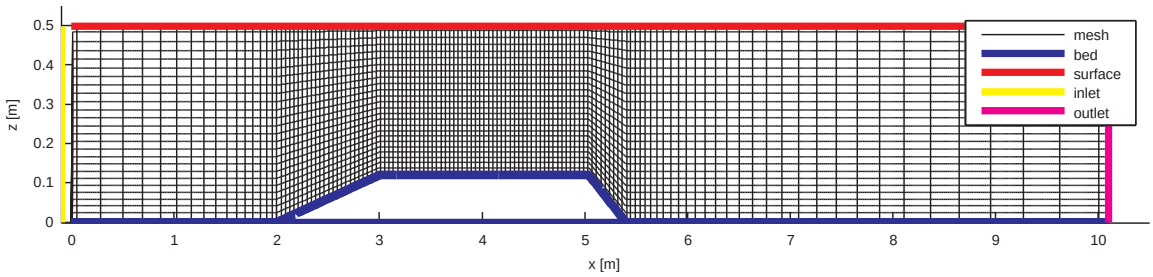

Figure 3-12 Mesh used for the long sill computations

3.5.2 Boundary conditions

The boundary conditions are the same as the boundary conditions for the previous two cases from table 3-6, except for a slightly larger discharge at the inlet boundary. The derivation of the inlet profiles is shown in appendix D.

3.5.3 Validation

The computation time again is 200 s with a time step `deltaT` of 0.0001 s. The results can be seen in figures 3-13 and 3-14.

The discharge in OpenFOAM seemed to be underestimated with on average 3%. However, increasing the discharge led to unrealistic turbulent kinetic energy profiles. Since the velocities are predicted reasonably well even though they are somewhat underestimated, it is chosen to

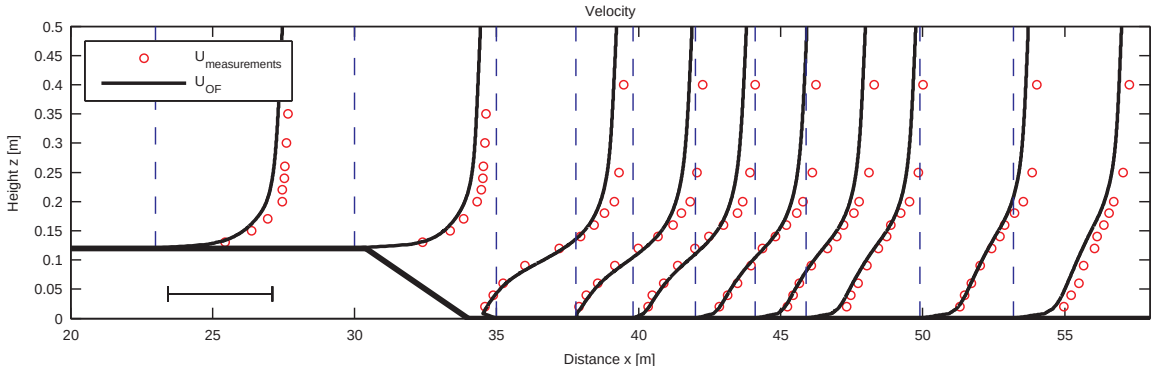

Figure 3-13 OpenFOAM velocity output of the long sill simulation compared with measurements from Jongeling et al. [2003] (the scale for 1.0 m/s is indicated)

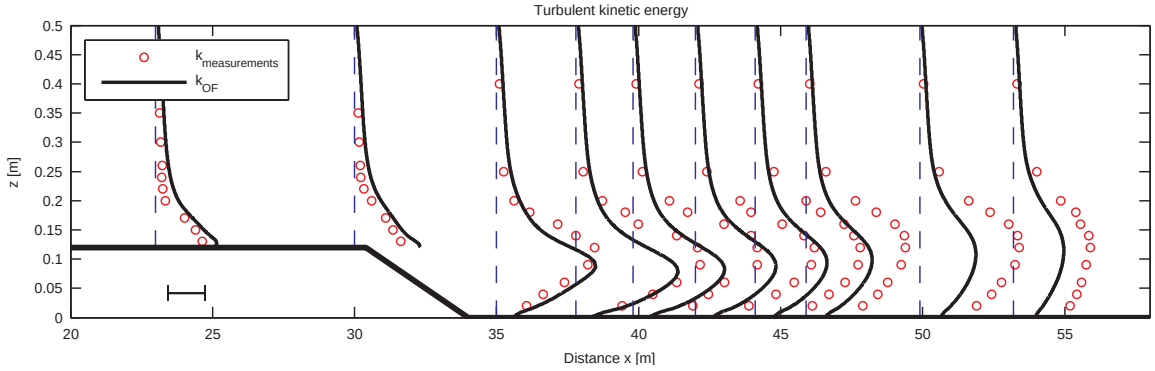

Figure 3-14 OpenFOAM turbulent kinetic energy output of the long sill simulation compared with measurements (the scale for 0.01 m^2/s^2 is indicated)

use the velocities as final model output. The velocities from OpenFOAM reproduce the measurements reasonably with a deviation varying from around 4 % from $x = 40$ to the end of the sill and 15% in the recirculation zone behind the sill. The turbulent kinetic energy just behind the still shows large agreement with the measurements. The further from the sill, the larger the deviations get.

3.6 Concluding remarks

In the flat bed case in section 3.3 is is noticed that 3D effects occurred in the measurements in the flume the 'Kolkmangoot'. Because of these effects the OpenFOAM output deviates from the measurements. The velocity profiles from the model agree reasonably well with the measurements. But the turbulence characteristics show large deviations. The short sill and long sill simulations also showed the same behaviour. The velocities deviated in the order of 5 to 10% from the measurements while the error in the turbulent kinetic energy could even be of the order of 50%.

This deviations from the measurements arise because the simulations in OpenFOAM are done in 2D. A solution for this problem is to include the glass side walls in the model. By modelling in 3D the effects that occur in the flume are also simulated in OpenFOAM. The output of the numerical model is used in later chapters to calculate the advective acceleration. For this calculation only the the velocities are of importance (see section 4.4). Because of this, the choice is made to not optimize the model output any further in this thesis. This choice is supported by the fact that the data that is used for the calculation of the advective acceleration for Hoan [2008], Dessens [2004] and Huijsmans [2006] has an error of the same or even larger order of magnitude.

The result of this choice is that the boundary conditions of the model should be chosen in such a way that the flow characteristics are approximately correct. This results in an extreme sensitivity of the model output on the boundary conditions, which is far from optimal in numerical modelling.

Summarizing, deviations from the measurements in the 2D model are attributed to:

- the inflow boundary conditions;
- 3D effects in the measurements while modelling in 2D;
- the use of the rigid lid boundary instead of modelling the free surface.

The first step in optimizing the model is running a simulation of the flow in the entire flume in 3D. The mesh in horizontal direction has to fulfill the same requirements as in vertical direction. The large inflow area of the flume must be included in this 3D model. Together with the effects of the side walls, the actual flow properties in the measurement area of the flume should result. So, by modelling in 3D the problem with the extreme sensitivity on the inflow boundary is most likely also solved. A final step in optimizing the model is to simulate the free surface instead of the rigid-lid. Especially the short sill had a rather high Froude number, so the effect of the water level change could be of importance for the calculations.

This chapter concludes with a comparison of the model results obtained by the $k-\omega$ SST model with the model results with the $k-\varepsilon$ model in Jongeling et al. [2003]. Section 3.2 chooses the $k-\omega$ because of its performance in separating flow. The results from Jongeling et al. [2003] are plotted in figures 3-16 and 3-15 for the short sill and the long sill respectively. The figures below show that the computations with the $k-\varepsilon$ model result in almost identical profiles as with $k-\omega$ SST model. The use of the $k-\omega$ SST model has not a large advantage over the $k-\varepsilon$ for these particular simulations. It should be mentioned Jongeling et al. [2003] also modelled in 2D. The same causes as described above can be the reason for the deviations with the measurements.

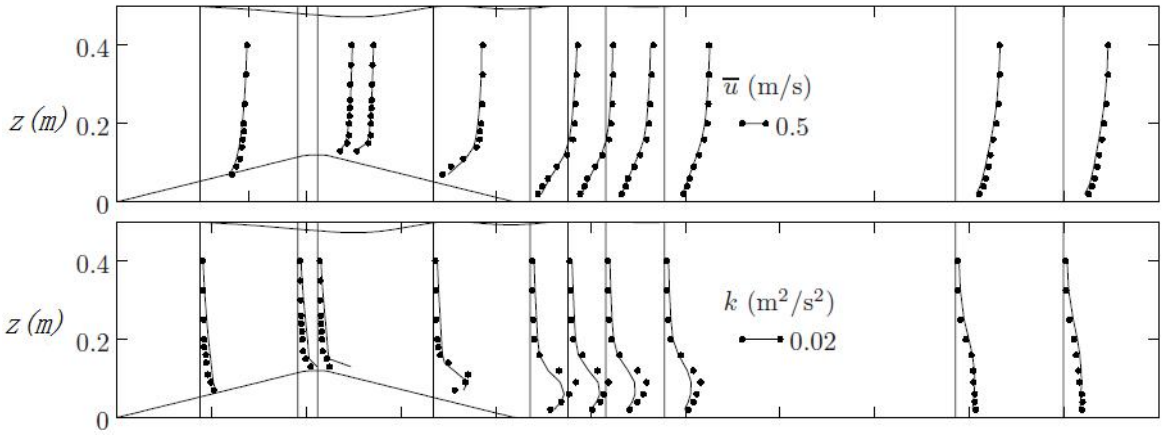

Figure 3-15 Model output from CFX with the $k-\varepsilon$ model for the short sill from Hofland [2005]

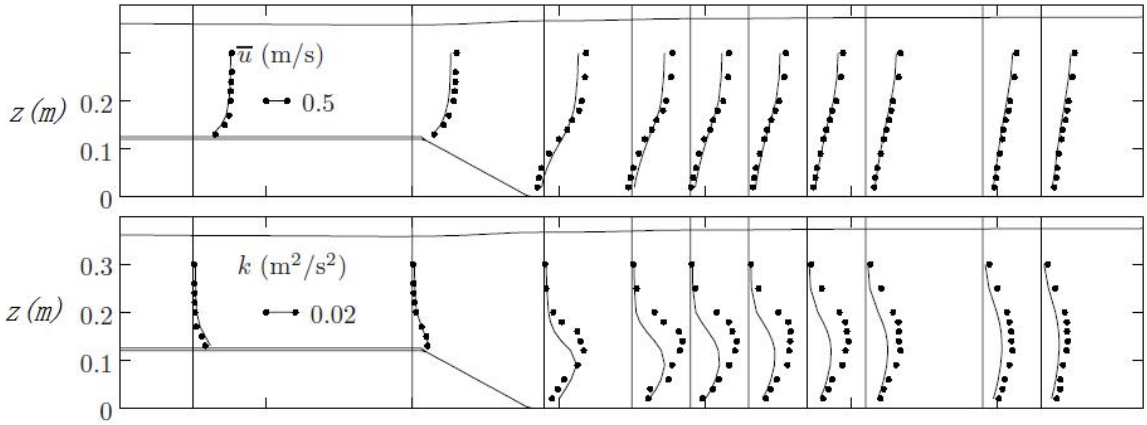

Figure 3-16 Model output from CFX with the $k-\varepsilon$ model for the long sill from Hofland [2005]

4 Data Processing

In section 2.5 the data sets that could be used to find the relation between the new stability parameter and the entrainment were mentioned. Information that is necessary, but could not be obtained from the data set of Jongeling et al. [2003], was reconstructed with the output of a numerical model in chapter 3. This above mentioned data will be used for the derivation of the stability relation in chapter 5. Before this can be done some important definitions, assumptions and methods in the processing of the data need to be discussed.

This chapter elaborates the calculation of the following variables:

- the mean velocity $\overline{u}_x$, $\overline{u}_y$ and $\overline{u}_z$ (section 4.1);
- the standard deviation of the velocity $\sigma(u_x)$, $\sigma(u_y)$ and $\sigma(u_z)$ (section 4.2);
- the turbulent kinetic energy k (section 4.2);
- the bed shear stress τ_b (section 4.3);
- the pressure gradient dp/dx (section 4.4);
- the spatial acceleration $\overline{a}$ (section 4.4)

Some of these variables already have been calculated in the reports associated with the data sets, but these will not be used in this thesis. In order to prevent inconsistencies in the calculations each of the variables is calculated from scratch. During an experiment a signal from the measurement instrument is measured every unit of time. This signal can be translated into a velocity. This results in a time series of velocity measurements with a frequency that depends on the used instrument. The velocity time series are the starting point for each of the calculations in this thesis. All of the calculated variables in this thesis are originate from these time series.

This chapter concludes with a brief discussion of the statistical methods that are used to calculate the correlation between the stability parameter and the entrainment rate.

4.1 Mean velocity

From each of the data sets, the mean velocity at every measured height above the bed is determined using equation 4-1.

$$\overline{u_j} = \frac{1}{n}\sum_{j=1}^{n} u_j \tag{4-1}$$

with:

j the direction x, y or z

The Hoan [2008], Dessens [2004] and Huijsmans [2006] data sets all had a flat bed covered with stones, and all the changes in geometry were in the lateral (y) direction. The velocities that are responsible for movement of the stones are the velocities along the bed, which in the cases above is the u_x velocity. The Jongeling data set has changes in geometry in the vertical z direction, and the definition of the velocity is not as trivial. One could argue that it are the velocities in the direction of the bed that causes the stones to move. On an upward sloping bed, part of the velocity could push a stone further into the bed. Therefore a velocityparallel to the bed $\tilde{u}$ is defined in equation 4-2. In the rest of this report all of the velocities and the variables derived

from it are the ones parallel to the bed.

$$\tilde{u} = u_{x//} + u_{z//} = u_x \cos\theta + u_z \sin\theta \tag{4-2}$$

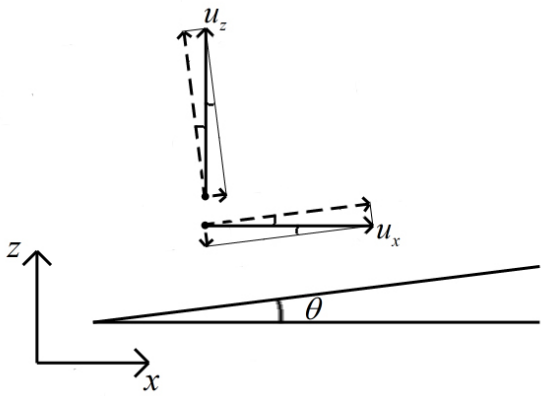

Figure 4-1 Definition of the velocity along the bed

In the measurements from Jongeling et al. [2003] and Hoan [2008] and LDV was used to measure the velocity, while in the Dessens [2004] and Huijsmans [2006] an EMS was used. Consequently, the Jongeling (0.02 m) and Hoan (0.005 m) data sets contains velocity measurements that are closer to the bed than the Dessens and Huijsmans data (0.028 m). In the method of calculation the Hofland stability parameter, the values of the velocities closer to the bed seem to have a rather large effect on the final value of the stability parameter. Therefore, for the velocity measurements of Dessens and Huijsmans a data point closer to the bed has been added by using a cubic interpolation for the velocity and a linear interpolation for the turbulent kinetic energy (see figures 4-2a and 4-2b). The extra data point is situated at a height of 0.15 m. The reason for this is that this is the closest point near the bed for the other data sets.

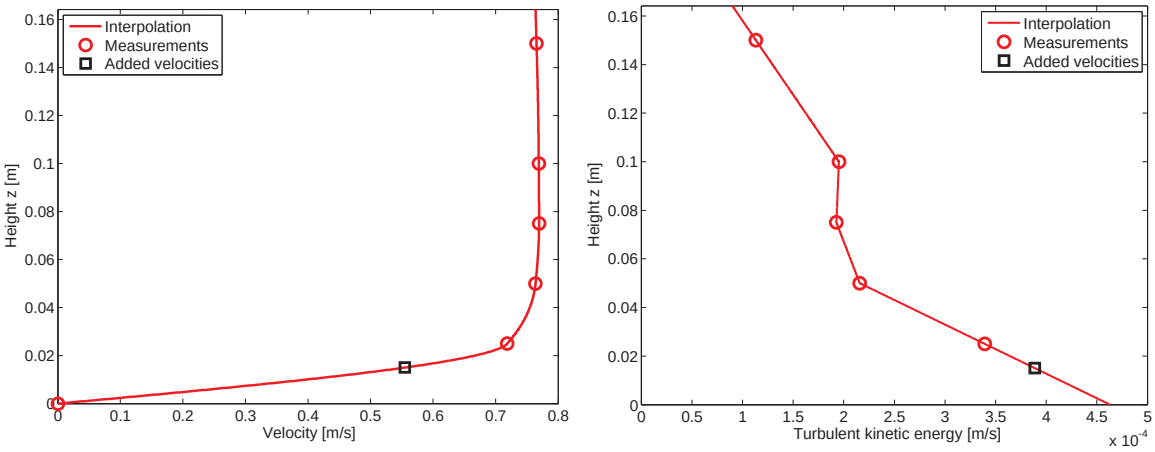

(a) Velocity

(b) Turbulent kinetic energy

Figure 4-2 Added data points using interpolation

4.2 Turbulent kinetic energy

The turbulent kinetic energy is calculated using the standard deviation that is obtained from the velocity measurements. The standard deviation can be calculated using equation 4-3. after

which the turbulent kinetic energy can be calculated using 2-15.

$$\sigma(u_j) = \sqrt{\frac{1}{n}\sum_{i=1}^{n}\left(\overline{u_i} - \frac{1}{n}\sum_{i=1}^{n} u_j\right)^2} \tag{4-3}$$

for

j is x, y or z

n is the number of measurements

In the Jongeling data set, velocity measurements are available in three directions (x and z with LDV and x and z with EMS). Because the measuring volume of the EMS is larger than the LDV, the fluctuating velocities are underestimated by this device (Hofland [2005]). Therefore, $\sigma(u_y)$ was corrected using the ratio between $\sigma(u_x)$ measured by the LDV and the EMS. Hoan [2008] also measured the velocities in x and z direction with an LDV. He used the EMS measurements in x and z direction to derive an approximation for $\sigma(u_y)$, given in equation 4-4.

$$\sigma(u_y) \approx \frac{\sigma(u_x)}{1.9} \tag{4-4}$$

In the Dessens and Huijsmans data sets only the velocity in x and y direction are known. In Nezu [2005] an empirically found ratio between the standard deviations σ in different directions is found, this is shown in equation 4-5. In the Dessens and Huijsmans data sets, $\sigma(u_z)$ is approximated by this value.

$$\sigma(u_z) \approx \frac{\sigma(u_x)}{1.82} \tag{4-5}$$

4.3 Bed shear stress

The bed shear stress τ_b is calculated to make a comparison between the new stability parameter and the stability parameter of Shields [1936]. In equation 2-8 the definition of the bed shear stress can be found. First the shear stress velocity u_τ is calculated for the datasets. The value of u_τ is then used to calculate the bed shear stress with $\tau_b = \rho u_\tau^2$. The shear stress velocity can be calculated in two ways.

1. Using the definition from equation 2-18:

$$u_\tau = \sqrt{\nu \left.\frac{\partial u}{\partial z}\right|_{z=0}}$$

2. Using the velocity measurement point closest to the bed and the law of the wall from table 2-1:

$$u_\tau = \frac{\overline{u} \cdot \kappa}{\ln \frac{z}{z_0}}$$

In section 5 the shear velocity will be used to compute the Shields stability parameter. This is done to compare its behavior compared to the new stability parameter. Because it is the behavior that is important and not the accuracy of the method, method 2 is used to calculate u_τ because it requires the least computation steps. A z_0 if $d_{n50}/15$ is used in the calculations.

4.4 Acceleration

The formulation for the force on a stone caused by acceleration is given in equation 2-23. Since only the advective acceleration is considered this reduces to equation 4-6.

$$F_a = -C_m V \frac{\partial p}{\partial x} = C_m \rho V u \frac{\partial u}{\partial x} \tag{4-6}$$

As equation 4-6 shows, the force on a stone can be expressed as both a pressure gradient and the advective term of the material derivative. There are no measurements of the pressure, but the pressure can be obtained from the numerical modelling output for the Jongeling and Hoan data sets. Equation 4-7 shows how this is done for the numerically modelled data sets.

$$\frac{\partial p}{\partial x} = \lim_{\Delta x \to 0} \left(\frac{\Delta p}{\Delta x} \right)_{m+\frac{1}{2}} \approx \frac{p_{m+1} - p_m}{\Delta x} \tag{4-7}$$

With:

m the number of the strip

The advective acceleration is calculated using the velocity profiles that were obtained in section 4.1. Both the u and du/dx part of the advective acceleration term is calculated at the middle of a strips using the central differences scheme (see also table 3-1). Equation 4-8 shows the method of calculating the acceleration. The governing variables are visualized in figure 4-3. The calculated acceleration is the acceleration in the direction parallel to the bed.

$$\overline{a} = u \frac{\partial u}{\partial x} = \lim_{\Delta x \to 0} \left(u \frac{\Delta u}{\Delta x} \right)_{m+\frac{1}{2}} \approx \left(\frac{u_{m+1} + u_m}{2} \right) \frac{u_{m+1} - u_m}{\Delta x} \tag{4-8}$$

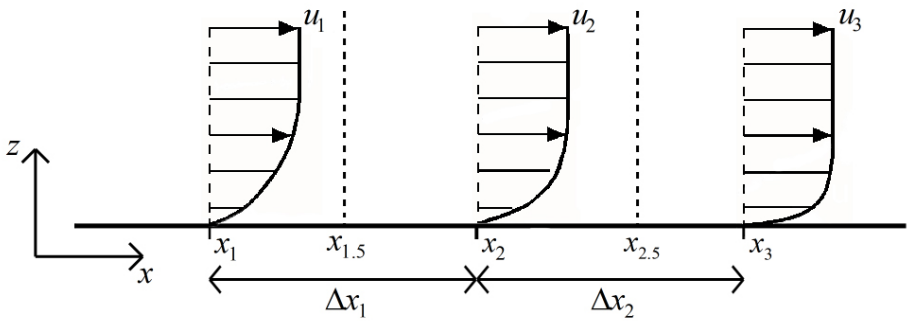

Figure 4-3 Variables used to calculate the acceleration

The acceleration in the Jongeling and Hoan data sets is determined using the output of the numerical models. The bed response is measured as the number of stones that moved from a certain strip and can be seen as the strip-averaged bed response. The acceleration is therefore also calculated as the average over a strip. The acceleration is first calculated at the center of every grid cell located within the strip. This means that a number of advective acceleration profiles is obtained. In the numerical computations of the Jongeling cases the cell length is approximately 0.01 m and in the Hoan computations 0.03 m, resulting in 9 and $3-4$ acceleration profiles re-

spectively. These profiles are subsequently averaged over the length of the strip. Equation 4-9 shows this calculation. It should be mentioned that the velocity is the velocity parallel to the bed, which is described section 4.1.

$$\left(u\frac{\Delta u}{\Delta x}\right)_{\text{strip}} \approx \frac{1}{M}\sum_{m=1}^{M}\left[\left(\frac{u_{m+1}+u_m}{2}\right)\frac{u_{m+1}-u_m}{\Delta x}\right] \tag{4-9}$$

with:

M the number of acceleration profiles within the strip
m the location of the profile

The acceleration in the Dessens and Huijsmans data sets is determined using the same method ase described for the Jongeling and Hoan data sets. However, since the measurements only have been performed at both sides of the strips of 0.1 m, the Δx that has been used also had this value. This resulted in only one acceleration profile at the center of each strip.

Now, the strip-averaged acceleration profile over the entire depth is known. The mechanism that causes a force on the stone due to spatial acceleration as described in 2.2.2 can be considered as a local mechanism. Accelerations in the higher parts of the flow do not generate forces on the stone. Only the acceleration at a certain height above the bed should be accounted. The height above the bed where the velocity is taken is called h_a in this report. Section 5.1 elaborates on the question which height above the bed should be taken.

4.5 Entrainment

The entrainment is calculated using the expressions from equation 2-35, using the measured number of stones that have moved from a certain strip. In Hofland [2005] it is argued that the measured number of colored stones is not a correct measurement. This is caused by:

- The stones that leave their position and end up within the strip of origin are neglected;
- Often in stone stability experiments, a certain stone color is used multiple times. Stones that end up in the strip with the same color are therefore not taken into account.

Because of the above mentioned effects, the measured number of stones leads to an underestimation of the entrainment. Hofland [2005] developed a method to calculate the total entrainment from the measured entrainment. In this method the strip length, stone diameter and the probability distribution of the displacement length of the stones are used. It is assumed that:

- the probability of a certain displacement length is distributed according to a negative exponential distribution;
- the average displacement length is proportional to the stone diameter;
- the probability of a certain stone originating from a certain position within a strip is uniformly distributed;
- stones from strips with the same color are situated at such a distance that the stones do not reach the next strip.

This leads to equation 4-10.

$$E_c = \frac{\tilde{L}}{1-e^{-\tilde{L}}}E_m \tag{4-10}$$

with:

E_c the corrected entrainment rate [ms^{-1}]
E_m the measured entrainment rate [ms^{-1}]
$\tilde{L}$ the dimensionless strip length $\tilde{L} = L/\bar{l}$ [-]
$\bar{l}$ the average displacement length [m]

Because the displacement lengths were measured in neither of the data sets that are used, the displacement lengths are estimated using the results of De Gunst [1999] who did measure the displacement lengths. De Gunst [1999] used a strip length of $L = 9.2d$ and found that $\tilde{L} = 1.51$. Since it was assumed that the average displacement length was proportional to the stone diameter this data can be used to determine $\tilde{L}$ for the other data sets. Using this method leads to the results in table 4-1.

Data	L	E_c
Jongeling	16.1d	2.83 E_m
Hoan Dessens Huijsmans	12.2d	2.31 E_m

Table 4-1 Entrainment corrections using the method of Hofland [2005]

Hoan [2008] mentions that, although this method is more physics based, has to be applied cautiously. He states that measurements of the displacement lengths should be available and that the use of the De Gunst [1999] results leads to an overestimation of the entrainment for the Hoan [2008] data where it was observed that the stones usually were moved much further. He roughly estimated the displacement length from this, leading to a corrected entrainment $E_c = 1.10E_m$. Since the characteristics were the same in the Dessens and Huijsmans data, this is also used for the entrainment from these data sets. The correction factor for the Jongeling data of $E_c = 2.83E_m$ is kept this way because in both Hoan [2008] as well as Hofland [2005] this gives best relation with the stability parameters.

4.6 Correlation analysis

In section 5 a relation between the stability parameter Ψ and the dimensionless entrainment rate Φ_E is established. The performance of this relation is based on the correlation between the stability parameter and the entrainment rate, which is is quantified by the coefficient of determination R^2 in equation 4-11 (this method is also used in Hoan [2008]).

$$R^2 = 1 - \frac{SSE}{TSS} \tag{4-11}$$

With SSE the error sum of squares and TSS the total sum of squares. These are defined for this as in equation 4-12a and 4-12b respectively.

$$SSE = \sum_i (\Phi_i - \hat{\Phi}_i)^2 \tag{4-12a}$$

$$TSS = \sum_i (\Phi_i - \overline{\Phi})^2 \tag{4-12b}$$

With:

Φ_i the measured entrainment rate
$\hat{\Phi}_i$ the entrainment rate predicted from the proposed relation
$\overline{\Phi}$ the mean entrainment rate

The relation between the entrainment rate and the stability parameter ($\Phi = a\Psi^b$) is found through linear regression for one independent (Ψ) and two constants (a and b). This relation can than be used for calculating the predicted entrainment rate $\hat{\Phi}_i$ in equation 4-12a.

5 Stability Relation

The raw data from chapters 2.4, 3 is processed with the methods described in chapter 4. The result is a consistent data set that serves as input for the derivation of the stability relation in this section. A stability parameter that incorporates the effects of velocity, turbulence and acceleration is composed. Figure 2-27 gives a general description for a stability parameter, this is repeated below.

$$\Psi_{\text{tot}} \equiv \frac{\left(C_{\text{b}}(\bar{\tilde{u}}+\tilde{u}')+C_{\text{m}}(\bar{\tilde{a}}+\tilde{a}')d\right)_{\max}}{\Delta g d}$$

In the existing stability parameter of Hofland only the first part of this equation is taken into account. In this way the effects velocity and velocity fluctuations are incorporated. The definition of the Hofland stability parameter is:

$$\Psi_{\text{Lm}} = \frac{\max\left[\left\langle \bar{u}+\alpha\sqrt{k}\right\rangle_{Lm}\frac{L_m}{z}\right]^2}{\Delta g d}$$

Some of configurations have a slope in the bed. The effect of a bed slope on the stability is included in the way described in section 2.2.3. Equations 5-1a and 5-1b describe this effect for an upward and downward sloping bed respectively. For all the stones, that all have a nominal diameter of approximately 5 - 10 mm, an angle of repose of 35° is obtained from figure 2-10. The calculated factor has to be applied to the strength (i.e. the denominator) of the stability parameter. For the upward slope of 1:8 in short and long sill configuration this leads to a reduction of the stability parameter of approximately 15%. The stability parameter increases approximately 20% on the downward 1:8 slope behind the short sill.

$$K(\beta_{up}) = \frac{\sin(\phi+\beta)}{\sin\phi} \tag{5-1a}$$

$$K(\beta_{down}) = \frac{\sin(\phi-\beta)}{\sin\phi} \tag{5-1b}$$

The force on the stones due to advective acceleration are added to the stability parameter described above. Chapter 5.1 discusses this acceleration force. In 5.1.2 the constants in the stability parameter are found using a correlation analysis. By linear regression a exponential relation between the stability parameter and the measured dimensionless entrainment rate is found and subsequently the coefficient of determination R^2 is calculated. The combination of constants that results in the highest correlation are used.

5.1 The acceleration force

The force on a stone caused by the advective acceleration in flow direction is described in equation 2-23 and is repeated below.

$$F_a = -C_{\text{m}}V\frac{\partial p}{\partial x} = C_{\text{m}}\rho V u\frac{\partial u}{\partial x} \approx C_{\text{m}}\rho d^3 u\frac{\partial u}{\partial x}$$

The equation shows that the force on the stone can be described by both the pressure gradient as the advective acceleration. In section 5.1.1 the pressure gradient profiles and the advective acceleration profiles obtained from the numerical models are compared. The final method of determining the acceleration is discussed in section 5.1.2.

5.1.1 Pressure gradient and advective acceleration profiles

Figures 5-1a and 5-1b show the pressure gradient $\frac{1}{\rho}\frac{dp}{dx}$ and advective acceleration $u\frac{du}{dx}$ profiles from the numerical results of the short sill simulation from Jongeling et al. [2003]. In figures 5-2a and 5-2b the same plots are given for the numerical results of the expansion from Hoan [2008].

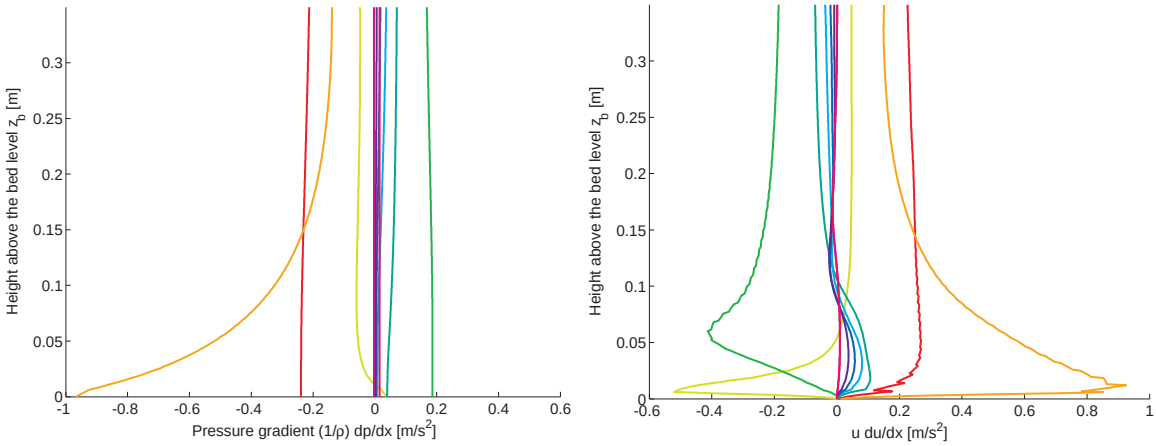

(a) Pressure gradient *(b) Advective acceleration*

Figure 5-1 Profiles from the short sill simulation

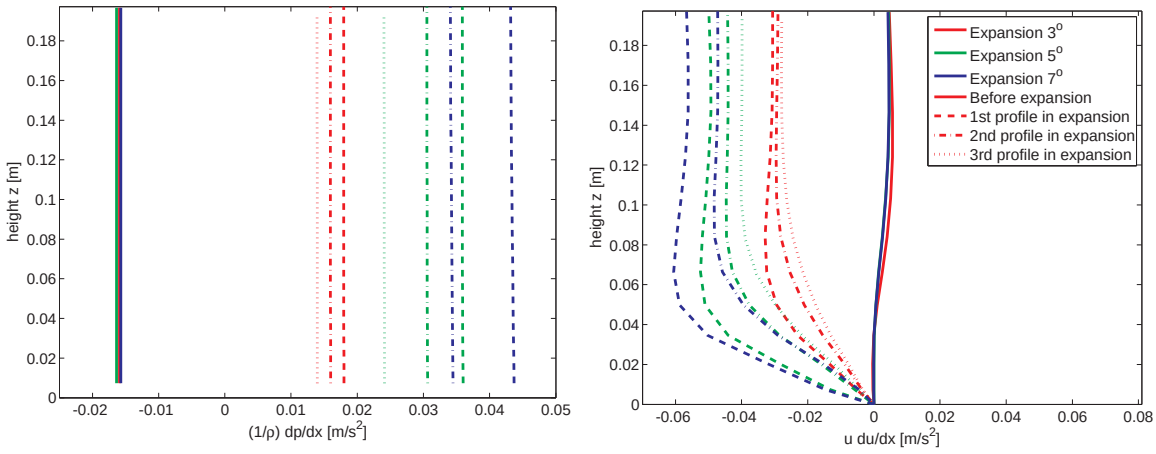

(a) Pressure gradient *(b) Advective acceleration*

Figure 5-2 Profiles from the expansion simulation from Hoan [2008]

In both figures the profiles with a negative pressure gradient belong to the profiles with a positive acceleration. A negative pressure gradients is associated with a positive net force and thus a positive acceleration. The profiles in the figures show this behavior correctly. Also it is observable that the pressure gradient is rather constant in the vertical in most of the profiles. The advective acceleration is more or less constant in the upper parts of the water column, but show large deviations from this value near the bottom.

The Euler equation given in the derivation of the force on the stone in appendix B suggests that

the pressure gradients are equal to the the negative value of the advective acceleration. In the short sill case 5-1 this is true in the upper part of the water column. Closer towards the boundary layer the absolute values of the pressure gradient and the advective acceleration starts to deviate. In the expansion in figure 5-2 the same behavior is observable. This is an indication that the approximation of the pressure gradient by using the material derivative of the velocity is not entirely accurate.

The most important findings based on figures 5-1 and 5-2 are:

- The pressure gradient is in most of the cases rather constant over the vertical. The advective acceleration is constant only in the upper parts of the vertical.
- The height above the bed at which the advective acceleration becomes constant is approximately equal for both cases (between 0.05 m and 0.10 m), although the water levels are very different. The short sill water level in the experiments is almost twice the expansion water level.
- Equation 2-23 suggests that the absolute value of the pressure gradient (with a factor $\frac{1}{\rho}$) is equal to the value of advective acceleration. For the short sill this is true in the upper parts of the vertical, but closer to the bed this is not true. In the expansion the absolute values of the pressure gradients deviate but are of the some order of magnitude higher in the water column. Near the bottom they again start to deviate from each other.

These findings will be used in the next chapter for the final definition of the force due to acceleration.

5.1.2 Determination of the acceleration force

Two variables are considered for the determination of the force on the stone due to acceleration:

- using the pressure gradient $\frac{\partial p}{\partial x}$
- using the advective acceleration $u\frac{\partial u}{\partial x}$

At first sight the pressure gradient seems the most obvious choice to use in the calculation of the acceleration force. Because the pressure gradient is nearly constant over the vertical for most cases, it does not really matter at what height the pressure gradient is determined. However, the pressure gradient is unknown in the data sets of Dessens [2004] and Huijsmans [2006]. These data sets have large accelerations in the flow and are of special interest for this research. Therefore the advective acceleration $u\frac{\partial u}{\partial x}$ is used in this thesis for the determination of the acceleration force. This brings up another problem, i.e. at what height h_a above the bed should the advective acceleration be determined?

In Hofland [2005] it is stated that $0.15d$ above the top of the stones is the optimal height for correlating velocity sources to forces on the stone. For this height, the velocity gives a more or less constant drag coefficient for all protrusions of the stone. Also is the correlation between the instantaneous velocity and the drag force maximum at this height. Contrary to the velocity a pressure fields penetrates further into the bed because of the porosity of stones, and therefore the determination is probably also done at another level above the bed.

The figures in the previous section show that the acceleration goes to zero at the bed, so choosing the acceleration to close to the bed would lead to an underestimation of the effect of the acceleration. On the other side, choosing the acceleration too high is also not undesirable since it is the acceleration near the bed that has effect on the stone.

In the previous section it is found that at a certain height above the bed the absolute values of the acceleration and the pressure gradient started to deviate. This height was approximately

equal for the short sill and the expansion, although the water depth was entirely different. This suggests that the behavior of $u\frac{\partial u}{\partial x}$ depends more on the stones on the bed and the geometry than on the water level. A logical step is to let the height h_a be dependent on the nominal stone diameter d_{n50}. Because it is not possible to find a value for h_a from the acceleration profiles. The height h_a is determined in the same way as the constants C_b, C_m and α, i.e. with a correlation analysis.

Now that the force caused by the acceleration is defined it is possible to give definition of the stability parameter that also contains the effects of advective acceleration. Equation 5-2 shows the new stability parameter[1]:

$$\Psi_{\mathrm{RS}} = \frac{\overbrace{C_\mathrm{b}\left(\max\left[\left\langle \bar{u}+\alpha\sqrt{k}\right\rangle_{Lm}\frac{L_m}{z}\right]^2\right)}^{\text{velocity and turbulence terms}} + \overbrace{C_\mathrm{m}\left(\bar{u}\frac{\partial \bar{u}}{\partial x}\right)_{h_a} d}^{\text{acceleration term}}}{K(\beta)\Delta g d} \tag{5-2}$$

The first part in the numerator is calculated with the method of Hofland [2005] as described in section 2.3.1. To be consistent in the way the parameter is calculated this is done from scratch for each of the data sets. The final step to a new stability parameter is to determine the constants C_b, C_m, α and h_a. A statistical method is used to find the combination of values for these constants that lead to the highest correlation. The next section covers this correlation analysis.

5.2 The determination of the constants

The constants in equation 5-2 that will be determined in this chapter are:

- C_b the relative importance of the force caused by velocity and turbulent velocity fluctuations, determined with the method of Hofland [2005].
- α the importance of the turbulent velocity fluctuations represented by $\sqrt{k}$ relative to the mean velocity.
- h_a the height above the bed where the advective acceleration, that is used to calculate the acceleration force on a stone, is determined.
- C_m The relative importance of the force caused by acceleration.

For relating the entrainment rate Ψ_E to the stability parameter Ψ_{RS} it is not the absolute value of $(C_\mathrm{b}(\bar{\tilde{u}}+\tilde{u}')+C_\mathrm{m}(\bar{\tilde{a}}+\tilde{a}')d)$ that is of importance but rather the ratio between the two terms. To establish a relation between Ψ_E and Ψ_{RS} the ratio between C_m and C_b is sufficient. Varying C_b will only cause a shift of the data points along the Ψ axis. In this thesis C_b is therefore set to 1 and in the remainder of this report the constant $C_{\mathrm{m:b}}$ is used, which is defined in equation 5-3. Instead of four unknowns now only three unknowns need to be found. It should be mentioned though that the resulting value in the numerator in the stability parameter says nothing about the magnitude of the actual force that is exerted on the bed.

$$C_{\mathrm{m:b}} = \frac{C_\mathrm{m}}{C_\mathrm{b}} \tag{5-3}$$

The constants α, h_a and $C_{\mathrm{m:b}}$ are now determined by finding the constants that result in the highest value of R^2. The method used for this was given in section 4.6. The value for α is var-

[1] RS stands for R squared (R^2) named after the method of determining the constants

ied 0 to 7 with steps of 0.25, based on the findings in previous researches (6.0 and 3.0 in Hofland [2005] and Hoan [2008] respectively). Based on table 2-3 $C_{m:b}$ is varied from 0 to 40. The height h_a is varied from 1.0 to 10.0 times the nominal stone diameter. This is the approximately the height over which the advective acceleration varies the most. These values are obtained from figures5-1 and 5-2. The following steps are taken:

1. Set values for α, $C_{m:b}$ and h_a/d_{n50}
2. Calculate Ψ_{RS} with equation 5-2
3. Find a and b in $\Phi_E = a\Psi^b$ trough linear regression (see section 4.6)
4. Calculate R^2 with equation 4-11
5. Repeat steps 1 to 4 for the values for α and C_m shown in table 5-1

Variable	Minimal value	Step	Maximal value
α	0.0	0.25	7.0
$C_{m:b}$	0.0	1.0	40.0
h_a/d_{n50}	1.0 b	1.0	10.0

Table 5-1 Used values for α and $C_{m:b}$ and h_a/d_{n50}

Using this method for the described values of α and $C_{m:b}$ h_a/d_{n50} leads to number of correlation contour plots. These are shown in appendix F for each of the values of h_a/d_{n50}. Table 5-2 and figure 5-3 show the R^2 and the associated $C_{m:b}$ and α for different heights h_a. In the table the values for h_a/d_{n50} of 20.0 is also calculated, to check the behaviour. For small h_a/d_{n50} the correlation is the lowest. As h_a increases R^2 also increases, until approximately a h_a/d_{n50} of 7.0. For higher values of h_a/d_{n50} the correlation and the associated values of $C_{m:b}$ remain more or less equal, although a small decrease is visible for higher h_a. The highest correlation with $R^2 = 0.8003$ is obtained for $h_a/d_{n50} = 9.0$, $C_{m:b} = 23.0$ and $\alpha = 3.75$. These values are used from now in the remainder of this thesis.

h_a/d_{n50}	$C_{m:b}$	α	R^2
1.0	0.50	24.0	0.6856
2.0	1.00	14.0	0.7093
3.0	1.50	12.0	0.7274
4.0	2.00	14.0	0.7537
5.0	2.75	18.0	0.7739
6.0	3.00	19.0	0.7886
7.0	3.50	22.0	0.7967
8.0	3.75	23.0	0.7998
9.0	3.75	23.0	0.8003
10.0	3.75	23.0	0.7969
20.0	3.75	22.0	0.7905

Table 5-2 R^2 and associated α and $C_{m:b}$ for different h_a

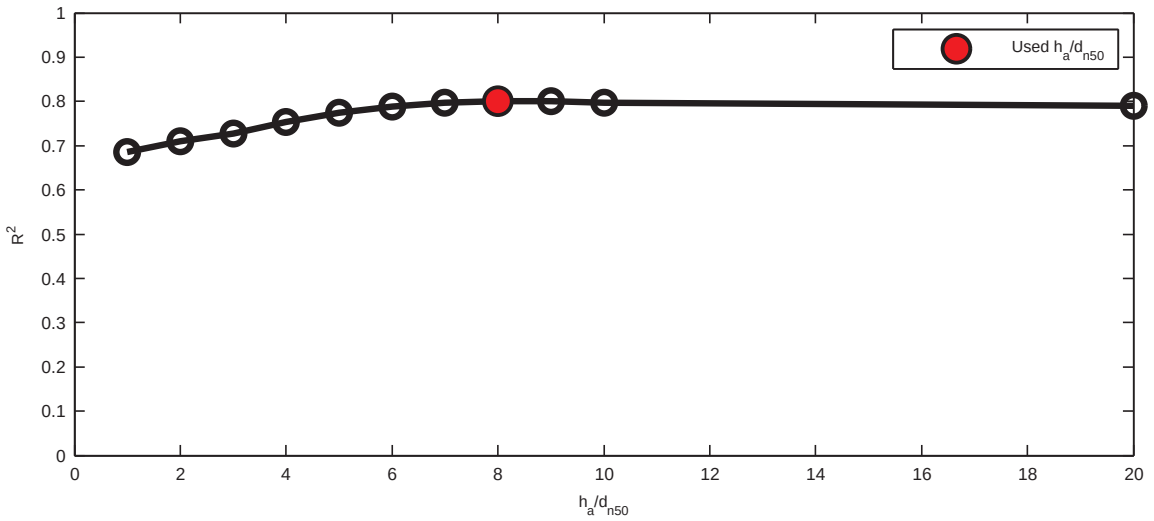

Figure 5-3 Plot of R^2 for different h_a

Figure F-12 shows the contour plot for $h_a = 9.0 \cdot d_{n50}$ in which the coefficient of determination R^2 is visualized for the different combinations of α and $C_{m:b}$. The black dots indicate the local maximum of R^2 for every $C_{m:b}$. The location in the contour plot for Ψ_{Lm} (with $\alpha = 3$ and $C_{m:b} = 0$) is also indicated. For Ψ_{Lm} a correlation of $R^2 = 0.2723$ is obtained.

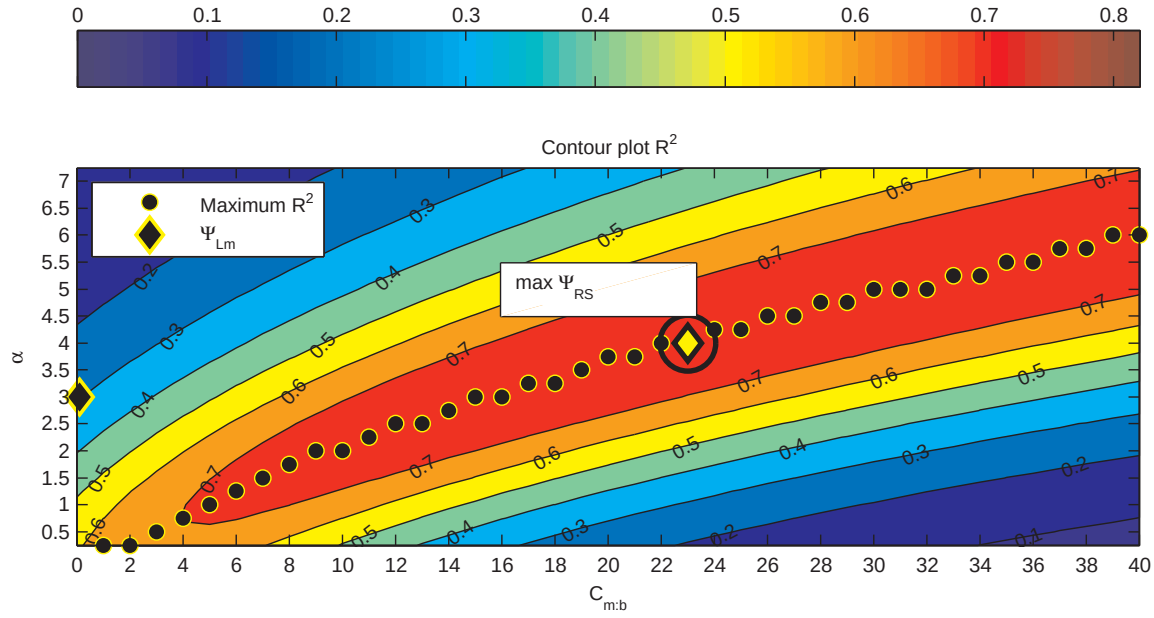

Figure 5-4 Contour plot resulting from the correlation analysis

The absolute maximum R^2 is found along the line of local maxima. The line of local maxima is plotted in 5-5 against C_m. An absolute maximum of $R^2 = 0.8003$ is found. Although the R^2 is fairly constant in the neighborhood of this point, it is observed that R^2 decreases for larger values of $C_{m:b}$. Table 5-3 summarizes the constants resulting in the highest correlation. These constants are used in the relation between the stability parameter Ψ_{RS} and the dimensionless entrainment rate Ψ_E. Chapter 6 evaluates the performance and behaviour of this new relation. This chapter also elaborates on the values that are found in this correlation analysis and a comparison with theory is made.

Constant	Value
α	3.75
$C_{m:b}$	23.0
h_a/d_{n50}	9.0

Table 5-3 The $C_{m:b}$, α and h_a/d_{n50} that give the highest R^2

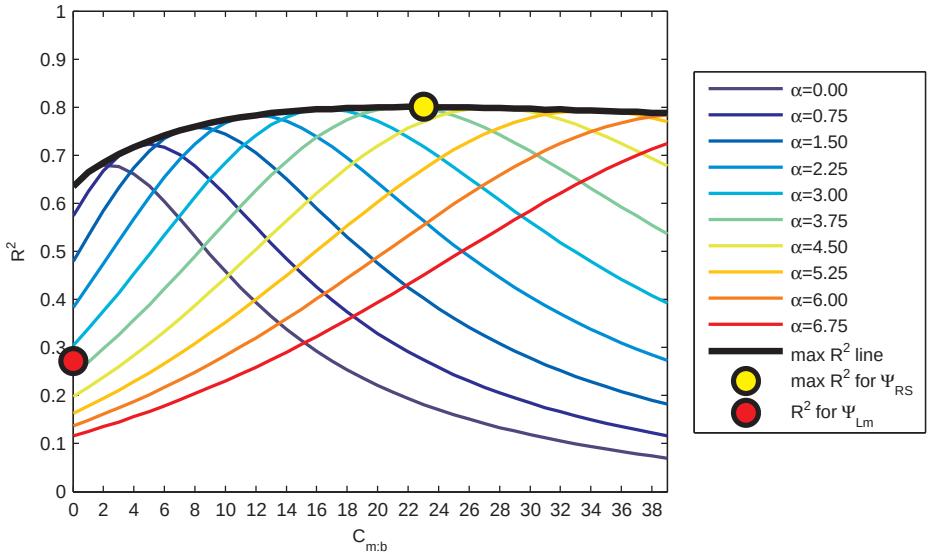

Figure 5-5 R^2 plotted against C_m. The colored lines are the R^2 for different values of α

6 Evaluation of the Stability Assessment Method

Chapter 5 discussed the determination of the constants in the stability parameter with incorporation of the acceleration forces Ψ_{RS}. This chapter elaborates on the relation of this stability parameter with the dimensionless entrainment rate. But first, in section 6.1, the performance of the already existing stability parameters Ψ_S, Ψ_{MS} and Ψ_{Lm} is checked for the data sets of this thesis. The relations of Ψ_{MS} and Ψ_{Lm} with Φ_E found by Dessens [2004] and Hofland [2005] respectively are also compared with the data sets.

After this, section 6.1 gives the new stability assessment method. This method contains the stability parameter Ψ_{RS} and its relation with the entrainment rate. An evaluation of this new method is given in section 6.3. The chapter concludes with an example of the application of the new method in section 6.4.

6.1 Evaluation of other stability parameters

This section checks the performance of the following already existing stability parameter:

- the Shields parameter Ψ_S (section 6.1.1);
- the Dessens parameter Ψ_{MS} (section 6.1.2);
- the Hofland parameter Ψ_{Lm} (section 6.1.3).

The stability parameters are calculated and plotted against the dimensionless entrainment rate for all of the data sets. The relations between the stability parameter and the entrainment rate that are derived before are also shown in these plots. These plots are used to check how well the existing stability parameters are performing for the data sets in this thesis.

6.1.1 The Shields parameter

The friction velocity u_τ, calculated with the method described in section 4.3, is input for the Shields stability parameter. Equation 2-28 defines the Shields parameter and is repeated below:

$$\Psi_S = \frac{u_{\tau c}^2}{\Delta g d}$$

The Shields parameter is calculated for each of the datasets. Figure 6-1 shows the Shields parameter Ψ_S plotted against the entrainment rate Φ_E. It can be seen

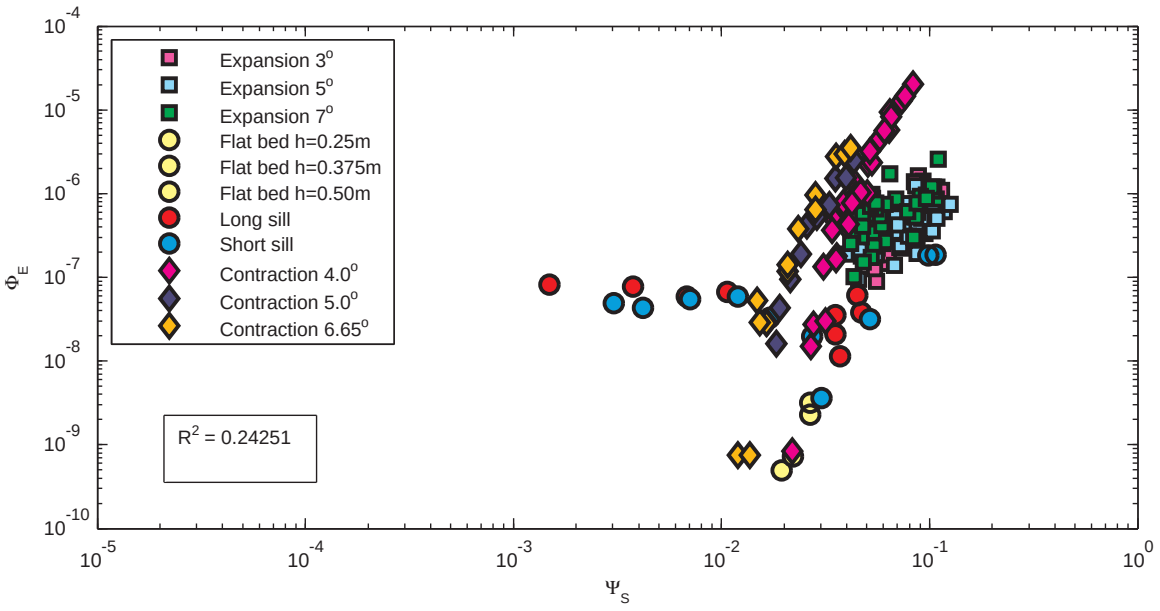

Figure 6-1 The Shields parameter Ψ_S plotted against Φ_E for all the data sets

A lot of scatter is present in figure 6-1. The coefficient of determination R^2 has a value of 0.24251. Especially the long and short sill configuration deviate from the cloud of data points. However, the main disadvantage of using the bed shear stress is illustrated when the data sets are shown separately. Figure 2-2 already showed that in accelerating flow the boundary layer get smaller resulting in larger shear stresses. Deceleration of flow causes a larger boundary layer and thus smaller shear stresses.

Figure 6-2 shows the Ψ_s at different locations along the contraction. With location 1 at the beginning to location 4 at the end. Along the contraction the shear stress gets larger. According to the Shields parameter the bed shear stress is the destabilizing force and increasing bed shear stress causes increasing entrainment. The figure clearly shows this behaviour for the accelerating flow. However, figure 6-1 shows that the data points in contraction with the smallest angle, for equal entrainment, have a larger Ψ_S than the contraction with a larger angle. In Dessens [2004] it was found that the expansions with larger angles had larger accelerations. The above is an indication that the effect of the acceleration itself (aside from the increased bed shear stress in accelerating) is not incorporated correctly in the Shields parameter. This corresponds to the findings of Dessens [2004] and Huijsmans [2006].

Figure 6-3 shows the data points in the expansion of Hoan [2008]. From figure 2-2 it is expected that Ψ_S decreases in decelerating flow. And the Shields parameter predicts a decreasing entrainment rate for smaller Ψ_S. The figure shows totally different behaviour. Ψ_S does get smaller further in the expansion but the entrainment rate stays equal or even increases. The effect of increased turbulence is absent in the Shields parameter.

This above clearly shows that the bed shear stress is not a sufficient measure for predicting the damage to bed protections.

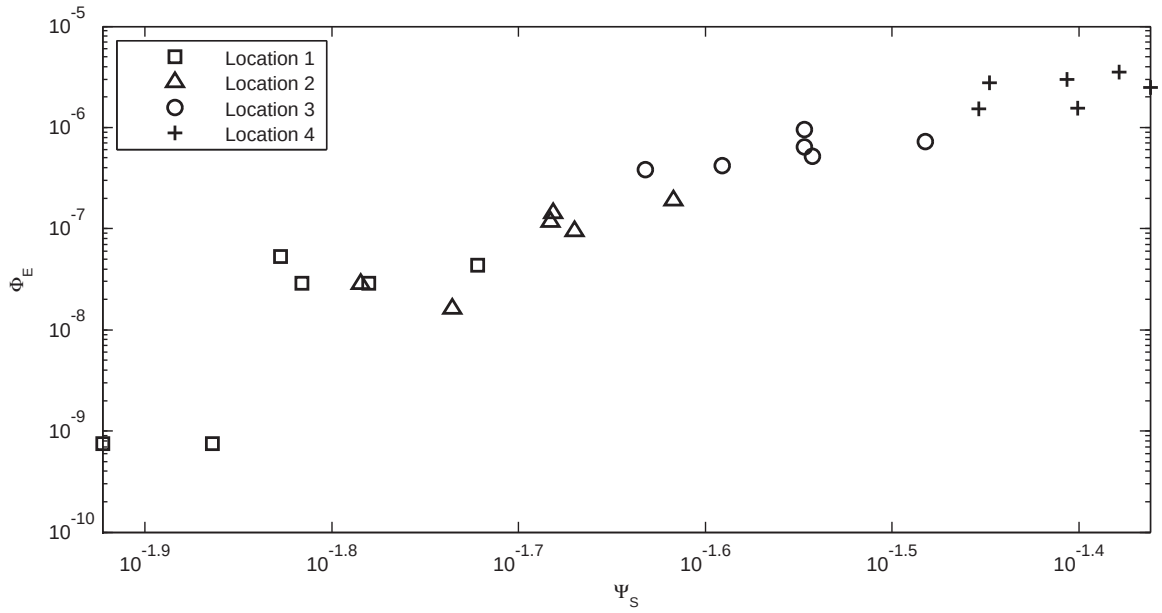

Figure 6-2 The Shields parameter Ψ_S plotted against Φ_E in the contraction

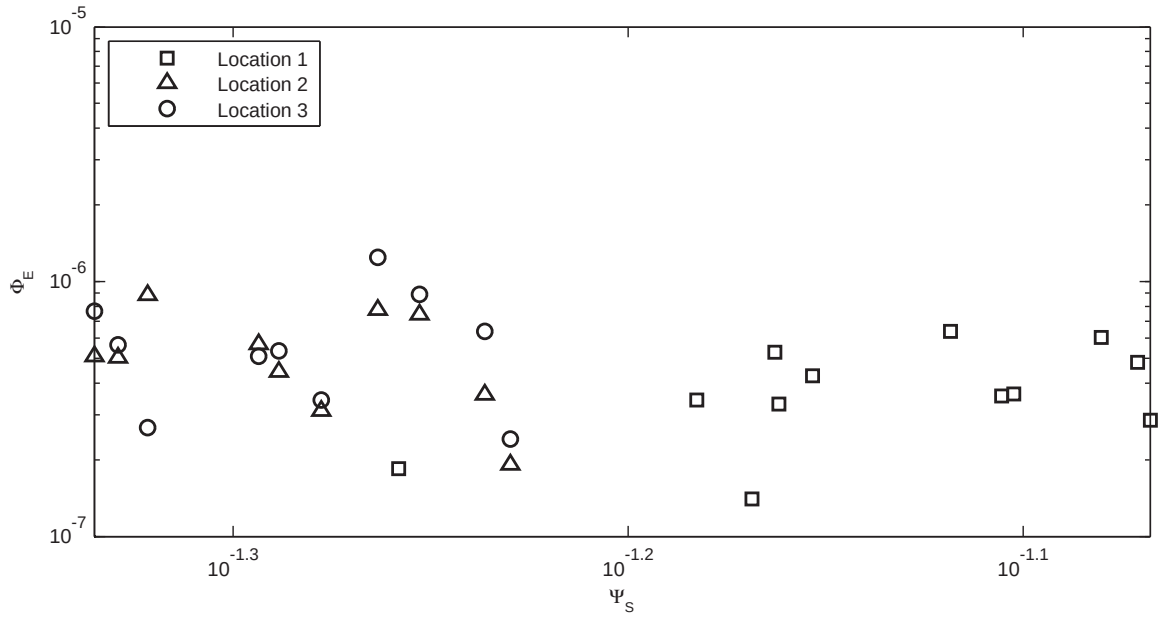

Figure 6-3 The Shields parameter Ψ_S plotted against Φ_E in the expansion

6.1.2 The Dessens parameter

The stability parameter Ψ_{MS} derived in Dessens [2004] uses the depth-averaged velocity and the depth-averaged acceleration. The values of $\overline{u}_{da}$ and $\overline{a}_{da}$ are obtained by averaging the velocity and acceleration profiles over the depth. Dessens [2004] coupled the depth-averaged velocity with the velocities in accelerating flow measured by the EMS (see figure 6-4). The argument for this is that the depth-averaged velocity is easy to determine, but that the actual, larger, velocity is causing the damage. Dessens [2004] gives a ratio between the depth-averaged velocity and the actual velocity higher in the water column of approximately 1.1. It should be mentioned thatsection 5.1 showed that the ratio between the depth-averaged velocity and the actual velocity in accelerating flow is far from trivial. Using the ratio between both velocities derived for the contraction therefore seems incorrect for other configurations. However, to show the behvaiour

of Ψ_{MS} this ratio is kept equal.

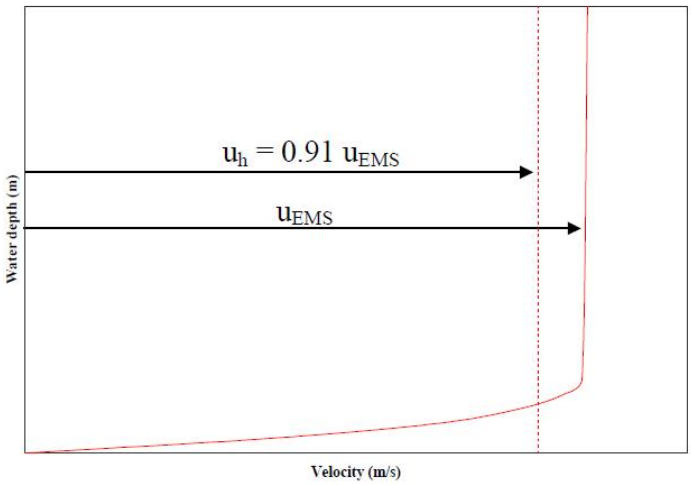

Figure 6-4 Definition of the velocities used by Dessens [2004]

The stability parameter from equation 2-29 is calculated and plotted against Φ_E in figure 6-5:

$$\Psi_{MS} = \frac{\frac{1}{2}C_b\overline{u}_{da}^2 + C_m d\overline{a}_{da}}{\Delta g d}$$

Equation 2-41 gives the relation between Ψ_{MS} and Φ_E found by Dessens [2004], with $C_b = 0.10$ and $C_b = 3.92$.This relation is also plotted in figure 6-5.

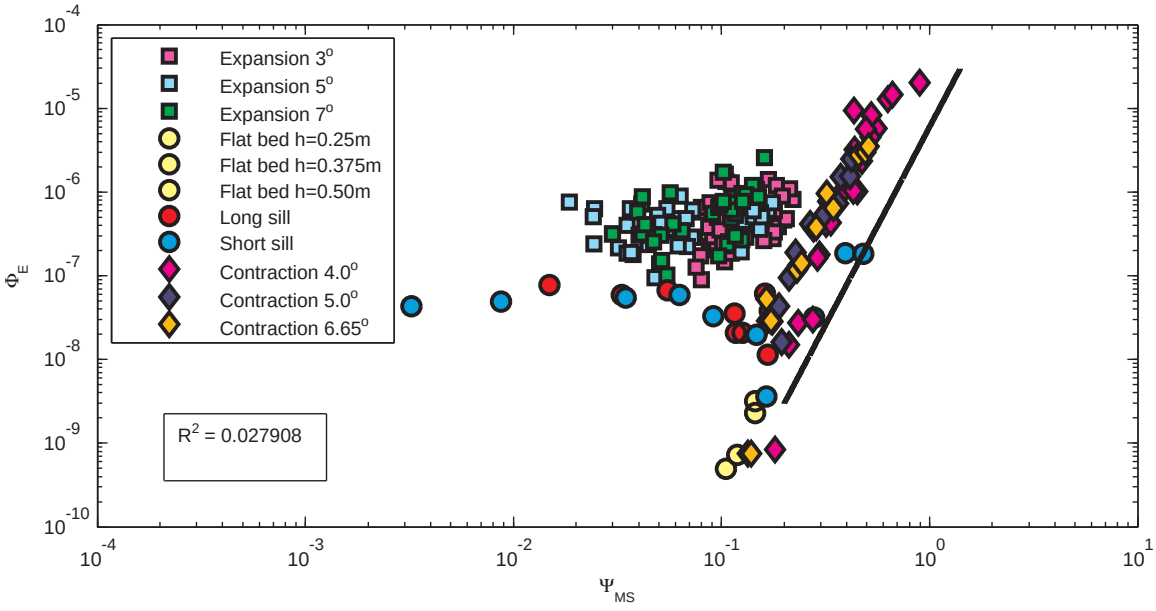

Figure 6-5 The Dessens parameter Ψ_{MS} plotted against Φ_E for all the data sets

Using Ψ_{MS} leads to even larger scatter than the Shields parameter Ψ_S. The value of R^2 is 0.0279 for the entire data set in this thesis. This is almost a factor 10 smaller than the R^2 from the Shields parameter. In contrast to figure 6-1, the contraction data points are now situated along one line. These are the data sets for which Ψ_{MS} is derived. The flat bed and part of the sill data points also lie along the same line.

The relation of Dessens [2004] does not go trough the data set of the contraction in figure 6-5. This is the result of the fact that the effect of turbulence is not included. Dessens [2004] gives equation 6-1 to account for the relative turbulence as function of the distance in the contraction. Dessens [2004] uses the negative x as the positive flow direction. So equation 6-1 states that the relative turbulence gets smaller further in the contraction. Dessens [2004] is not clear on how the relative turbulence changes in other configurations. Therefore this effect can not be included in figure 6-5, since this effect is different for each of the configurations.

$$\frac{u_{peak}}{u} = 0.10\left(\frac{x}{L}\right)^2 + 0.10\left(\frac{x}{L}\right) + 1.03 \tag{6-1}$$

The data points with a lot of turbulence (i.e. the expansion and part of the sills) deviate a lot from the data points of the contraction. For these data points the entrainment rate is highly underestimated by the relation of Dessens [2004], which is derived for relatively small turbulence. The entrainment rate in the expansion shows almost no correlation with the stability parameter.

The Dessens stability parameter Ψ_{Lm} performs reasonably for situations with relatively small turbulence, such as in accelerations. As soon as there is turbulence, and there is no formulation present for the change in relative turbulence, Ψ_{MS} does not predict the bed damage correctly. Using such is formulation is basically the same as using correction factors. This is something that should be avoided since correction factors are different for every other situation, which is clear to see in figure 6-5.

6.1.3 The Hofland stability parameter

The final existing stability parameter that is evaluated is the stability parameter Ψ_{Lm} from Hofland [2005].The parameter Ψ_{Lm} is defined by:

$$\Psi_{\text{Lm}} = \frac{\max\left[\left\langle \overline{u} + \alpha\sqrt{k}\right\rangle_{Lm} \frac{L_m}{z}\right]^2}{\Delta g d}$$

Both Hofland [2005] and Hoan [2008] give a formulation for the relation of Ψ_{Lm} with Φ_E. The relations are given in equation 2-42 and equation 2-45 respectively. The first is derived with the Jongeling et al. [2003] data set and uses an α of 6.0. The latter is derived with the data set from Hoan [2008] and has an α of 3.0. Both relations are plotted for all of the data sets in this thesis in figures 6-6 and 6-7 respectively. Both formulations do not include the acceleration and $C_{\text{m:b}}$ is thus equal to zero.

The data points with relatively high turbulence and the data points of the flat bed simulation are situated along the same line in both figures. Both the formulations go through these data points, although it is clear that the correlation is the highest for the data sets for which the formulations are derived. In Hoan [2008] a correlation with $R^2 = 0.81$ was found with $\alpha = 3.0$, but this was based only on his own data set. The correlation for all the data points in this thesis is much smaller and R^2 is 0.2722 for the relation of Hoan [2008]. The correlation of Ψ_{Lm} with $\alpha = 6.0$ for all the data sets is even smaller with a R^2 of 0.12523.

The data points from the configurations with high accelerations show much higher entrainment than that the relations predict based on the value of Ψ_{Lm}. This again is indicates that the entrainment rate is influenced by the effects of acceleration.

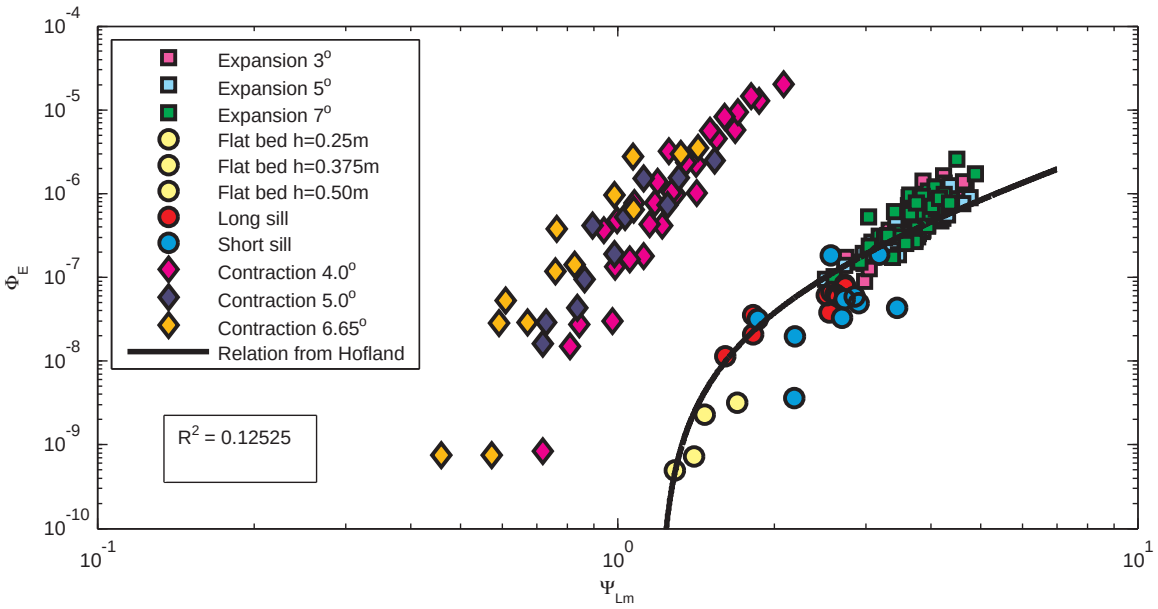

Figure 6-6 Ψ_{Lm} with $\alpha = 6.0$ plotted against Φ_E for all the data sets together with equation 2-42

The Hofland stability parameter Ψ_{Lm} was designed to incorporate the effects of turbulence explicitly. Figure 6-6 and 6-7 both show that the parameter does this correctly. This confirms the findings of Hofland [2005], in which the behaviour of Ψ_{Lm} was analysed more extensive for the configurations of Jongeling et al. [2003]. However, the data points with a larger acceleration do not predict the entrainment rate sufficiently. Both the relation of Hofland [2005] and Hoan [2008] underestimate the entrainment for the contraction configurations. This underestimation is attributed to the effects of the acceleration on the stone stability. The remainder of this chapter is dedicated to the stability parameter Ψ_{RS} which incorporates the forces due to acceleration in the stability parameter.

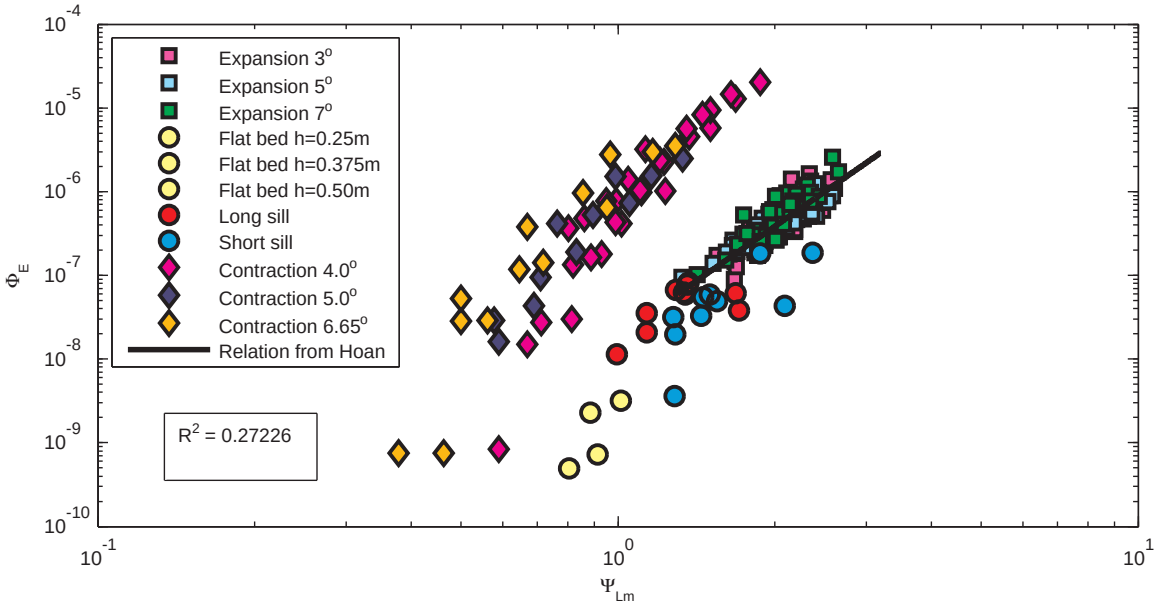

Figure 6-7 Ψ_{Lm} with $\alpha = 3.0$ plotted against Φ_E for all the data sets together with equation 2-45

6.2 The stability relation with incorporation of the acceleration

Equation 6-2 gives the final definition of the stability parameter Ψ_{RS}. The first term in the nominator includes the forces that are caused by the velocity and the turbulent fluctuations that reach the bed. The second term accounts for the force caused by the pressure gradient due to acceleration. The values of the constants α, $C_{m:b}$ and h_a are determined in section 5.2 by means of a correlation analysis.

$$\Psi_{RS} \equiv \frac{\left(\max\left[\left\langle \overline{u} + \alpha\sqrt{k}\right\rangle_{Lm} \frac{Lm}{z}\right]^2\right) + C_{m:b}\left(\overline{u}\frac{\partial \overline{u}}{\partial x}\right)_{h_a} d}{K(\beta)\cdot \Delta g d} \tag{6-2}$$

With:

α =	3.75 [-]
$C_{m:b}$=	23.0 [-]
h_a	$9.0 \cdot d_{n50}$ [m]
k	the turbulent kinetic energy [m^2// s^2]
Lm	the Bakmetev mixing length [m]
z	the height above the bed [m]
$\overline{u}$	the mean (i.e. time-averaged) velocity [m s^{-1}]
d	the nominal stone diameter d_{n50} [m]
$K(\beta)$	the correction for the bed slope [-]
g	the gravitational acceleration of 9.81 [m s^{-2}]

A power law of the form $\Phi_E = a\Psi_{RS}^b$ is used to relate Φ_E to Ψ_{RS}. The values for a and b in this power law follow from the regression analysis in section 5.2. Equation 6-8 gives the relation between the stability parameter and the bed response. The plot of this relation and the associated data points are given in figure 6-8.

The relation between this new stability parameter Φ_E and the dimensionless entrainment rate

Φ_E is given in equation 6-8 and plotted in figure 6-8.

$$\Phi_E \equiv 3.95 \cdot 10^{-9} \Psi_{RS}^{5.89} \qquad \text{for } 0.9 < \Psi_{RS} < 4.3 \tag{6-3}$$

The figure also shows the 95% confidence interval. This basically tells that the probability that Φ_E is situated within these limits is 95% for the used data sets. Table 6-1 gives some statistical quantities that followed from the regression analysis. These quantities can be used in for example probabilistic calculations (see TU Delft [2006]). In the table the mean and standard deviation of the constants in $\Phi_E = a\Psi^b$ are given. Note that the a in this equation is not the acceleration.

	μ	σ
a	$3.95 \cdot 10^{-9}$	$6.3470 \cdot 10^{-10}$
b	5.89	0.2044

Table 6-1 Statistical quantities of the relation in equation 6-2

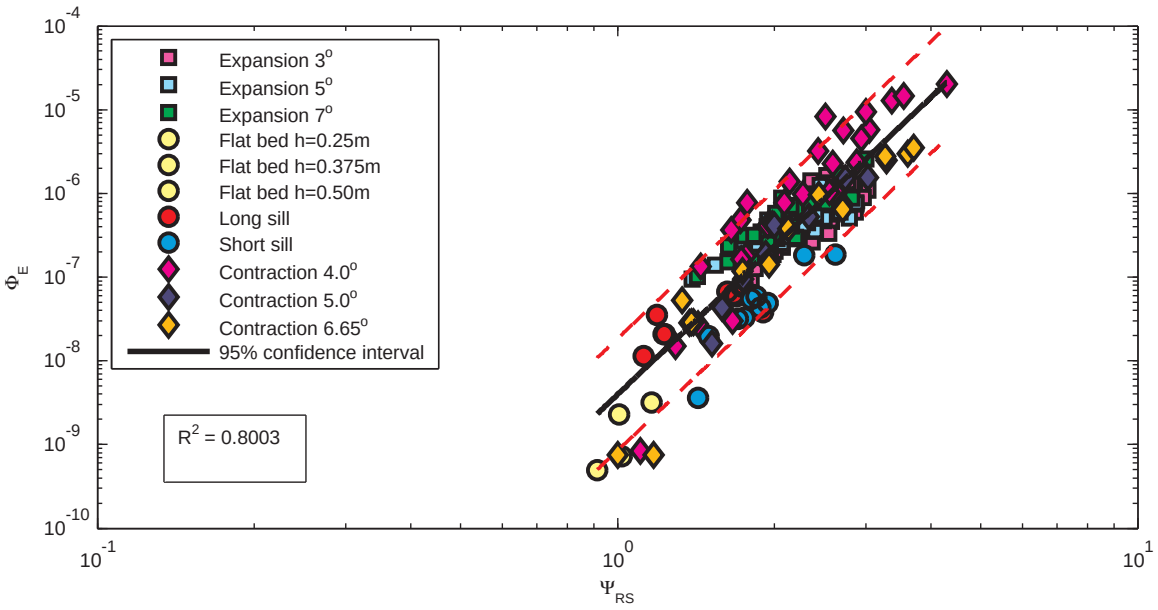

Figure 6-8 Ψ_{RS} plotted against Φ_E for all the data sets

6.3 Evaluation of the stability parameter

This section evaluates some characteristics of the stability parameter Ψ_{RS}. Section 6.1 showed that the entrainment rate in the data points of the configurations with high acceleration is underestimated with the existing parameter Ψ_{Lm} of Hofland [2005]. In figure 5-5 the influence of adding an acceleration term to the stability parameter is clearly visible. If Ψ_{Lm} ($C_{m:b} = 0$ and $\alpha = 3.0$) is used, the coefficient of determination R^2 has a value of 0.27. Using Ψ_{RS} results in a R^2 of 0.80. For the data sets used, adding an acceleration force to the stability parameter leads to a considerable increase in correlation ΔR^2 of 0.53.

Some aspects of the behaviour of Ψ_{RS} are discussed in section 6.3.1. Section 6.3.2 elaborates on the values of the constants and a comparison with literature is made.

6.3.1 Behaviour of the stability parameter

The second term in the nominator of the stability parameter Ψ_{RS} accounts for the acceleration force on the stones. The force due to acceleration causes the contraction data points in figure 6-7 to overlap with the other data points. Table 6-2 gives a crude classification of the used measurement data sets.

Data set	Configuration	Acceleration	Turbulence
Hoan [2008]	Expansion	Deceleration	High
Jongeling et al. [2003]	Flat bed	None	Low
	Short sill	Acceleration and Deceleration	Varying
	Long sill	Acceleration and Deceleration	Varying
Dessens [2004]	Contraction	High acceleration	Low
Huijsmans [2006]	Contraction	High acceleration	Low

Table 6-2 A crude classification of the data sets

The expectation is that acceleration, and thus a negative pressure gradient (see equation 2-23), causes a positive force on the stone. Deceleration causes a negative force on the stone, because of the positive pressure gradient. From table 6-2 the acceleration force should therefore be negative in the expansion and at the decelerating parts of the sills. In the contraction, the acceleration force should be positive. A positive acceleration force is also expected at the upstream side of the sill. The flat bed simulation is more or less in equilibrium and the force due to acceleration should be zero. It is mentioned again that the term 'acceleration force' is used, but the actual force on the stone is unknown since $C_{m:b}$ is used.

The actual influence of the acceleration that is added in Ψ_{RS} is inspected closer by looking at the difference with the Hofland stability parameter Ψ_{Lm}. Figure 6-9 shows Φ_E plotted against the acceleration force $\Psi_{RS} - \Psi_{Lm}$. A semi-log scale is used because the data sets also contain decelerations and thus negative forces due to acceleration.

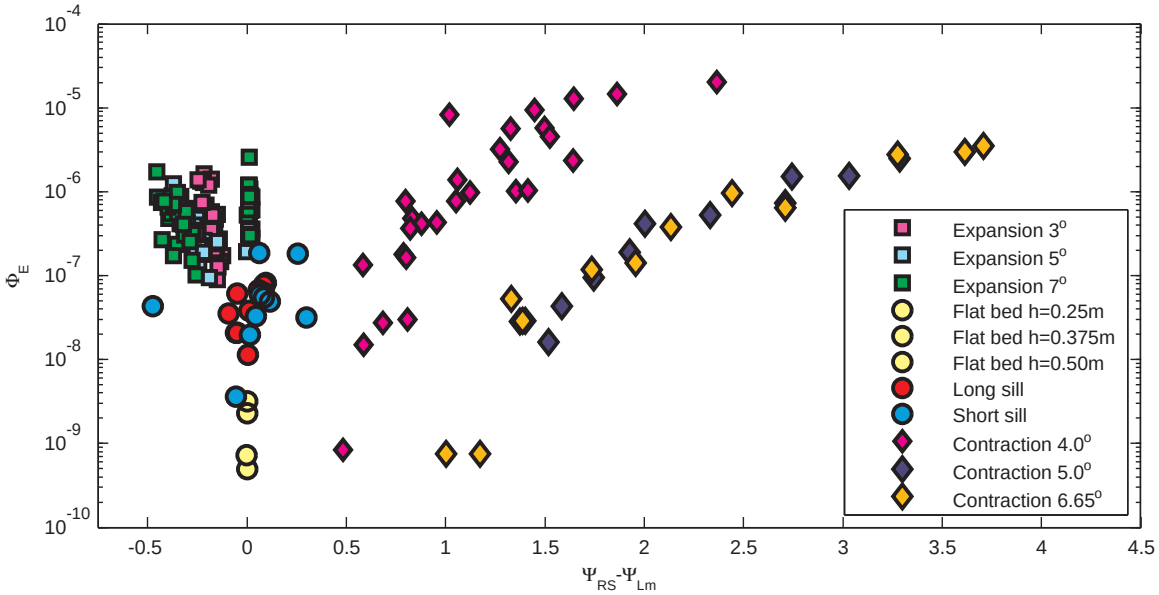

Figure 6-9 The difference between Ψ_{RS} and Ψ_{Lm} plotted against Φ_E for all the data sets

The figure shows that the acceleration part of Ψ_{RS} behaves as expected. The decelerating flow in the expansion causes a negative force on the stone, except for the data points located just before the expansion. The larger expansions (i.e. a higher angle) also show larger negative ac-

celeration forces on the stone. The pressure gradient in decelerating flow has a stabilizing effect on the stones.

The acceleration forces in the contraction are all positive. This means that the acceleration causes an extra destabilizing force on the stones. The contraction with the angle of 4° has the smallest force, because the acceleration in this configuration also is the smallest. In the contractions with the higher angles, the force due to acceleration is also larger.

The acceleration force in the flat bed data is zero as expected. The accelerations and decelerations in the long and short sill simulations are not high. The measurements meanly focused on turbulence properties. The measurement locations are therefore almost all situated further behind the sills, where the flow is recovering again from the deceleration just behind the sills. Figure 6-10 shows the behaviour of Ψ_{RS} compared to Ψ_{Lm} for different locations in the short sill configuration. The acceleration force is positive at the upward slope of the hill and on the crest. On the downward slope the flow decelerates again, resulting in a negative acceleration force. The flow profile recovers again behind the sill, resulting in an acceleration force that is small but positive.

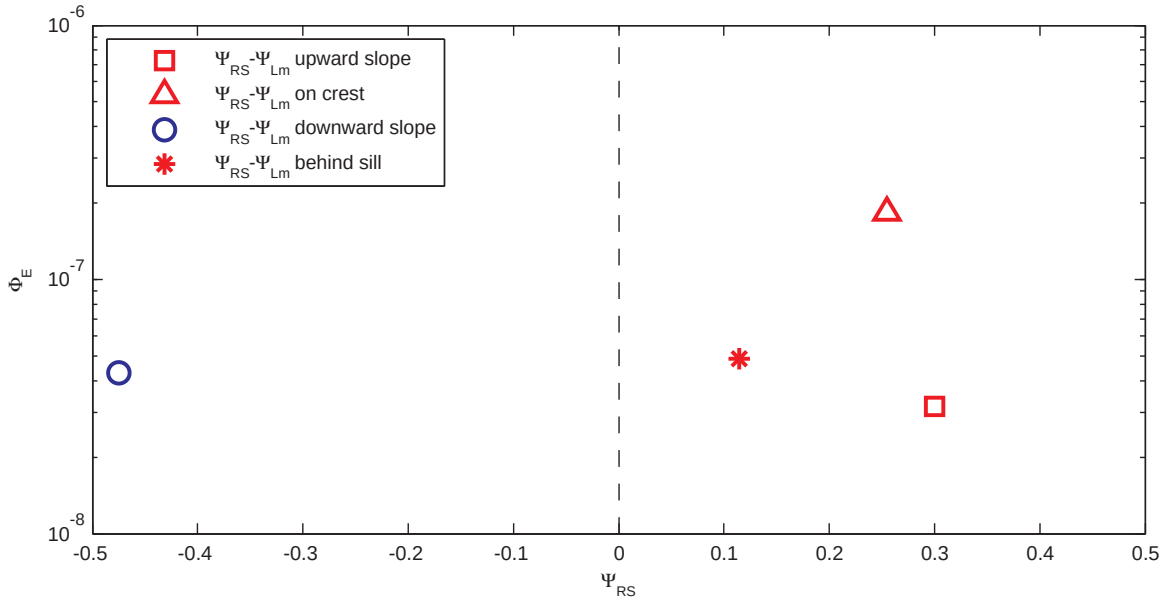

Figure 6-10 Ψ_{RS} compared to Ψ_{Lm} for different locations in the long sill configuration

In all of the cases described above, the added acceleration term in the Ψ_{RS} stability parameter shows the right behaviour. This means that the pressure gradients due to accelerations cause an extra destabilizing force on the stone. Decelerations have the reversed effect and have a stabilizing effect on the stones.

6.3.2 The values of the constants

The constants α, $C_{m:b}$ and h_a are determined by means of a correlation analysis. This analysis is a purely statistical method. The output of such an analysis should always be checked to find the physical meaning of the statistically found constants. This section compares each of the constants with theory and tries to explain the differences.

Turbulence

The highest R^2 in the correlation analysis is reached for α is 3.75. Table 6-3 gives some values of α that have been found in previous researches. The α in Hofland [2005] is derived for a wide

variety of configurations. Hofland [2005] suggests that a reason for the high α could be the fact that other force generating mechanisms such as turbulent wall pressures are not included. The α seems rather high since $\alpha = 3.0$ is a value that is often found in practice and measurements. Hoan [2008] found also found an α of 3.0 for his rather specific measurement configurations. This value corresponds to the value experienced in practice.

Research	α
Hofland [2005]	6.0
Hoan [2008]	3.0
This thesis	3.75

Table 6-3 Comparison of the found α

In this thesis only five of the eight configurations of Jongeling et al. [2003] are used. However, the stability relation is derived for a large number of different configurations i.e. three flat bed cases, a short sill an long sill, an expansion and a contraction. Therefore it is expected that the relation derived in this thesis is more universal applicable.

The value of α found in this thesis is slightly higher that the frequently used value of $\alpha = 3.0$. This can be explained in the following way. In the research of Hoan [2008], the α was derived without the incorporation of the stabilizing effect of the deceleration. In figure 6-9 it can be seen that this stabilizing effect is larger in the expansions with the larger angles. These configurations are also the ones with the highest turbulent intensities. For the Hoan [2008] data set it can be concluded that the configurations with higher turbulence also have higher deceleration. When the acceleration is included with equal α, this means that the data points with higher turbulence are effected more by the acceleration. This effect is illustrated in figure 6-11 for the data sets of Hoan [2008].

Figure 6-11a shows Ψ_{RS} with $\alpha = 3.0$ and figure 6-11b shows Ψ_{RS} with $\alpha = 3.75$. The acceleration is included in both of the figures. In the first figure, the data points are spread out because of the influence of the deceleration. Here the expansions with the larger angles are influenced more. By increasing the relative turbulence in figure 6-11b from 3.0 to 3.75, the points with higher turbulence intensities (and thus also deceleration) are moved together again resulting in a higher correlation. The standard deviation is approximately a factor 0.8 smaller in the second figure.

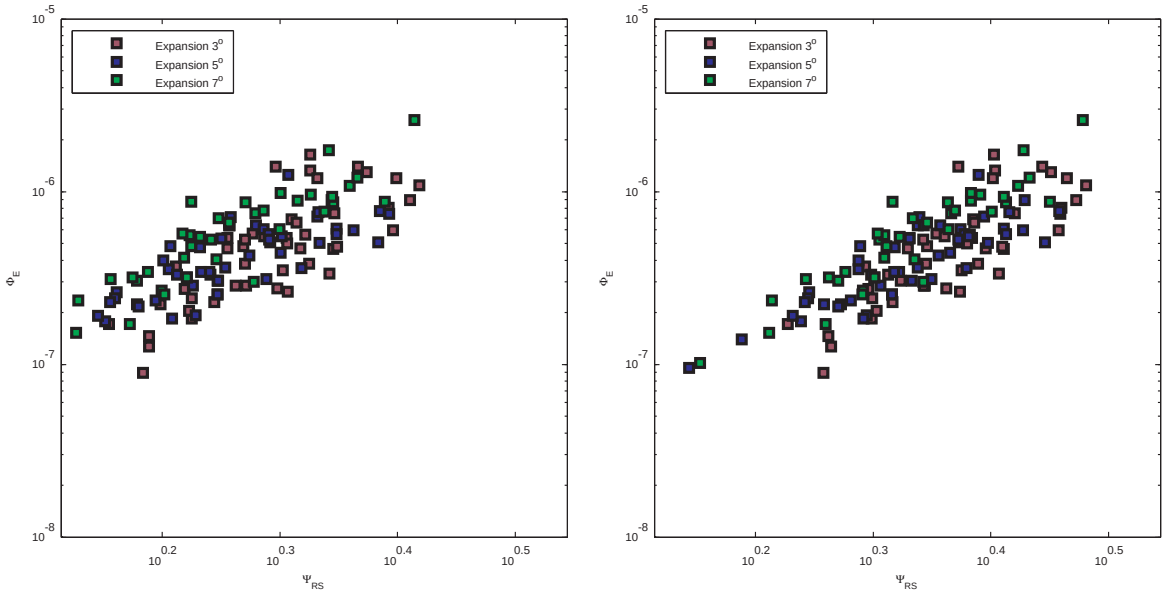

(a) Ψ_{RS}*:* $\alpha = 3.0$ *(b)* Ψ_{RS}*:* $\alpha = 3.75$

Figure 6-11 Ψ_{RS} *plotted against* Φ_E *for different values of* α

Acceleration

The constants associated with the acceleration are $C_{\text{m:b}}$ and h_a. Table 2-3 gives the values for C_{b}, C_{m} and $C_{\text{m}}/C_{\text{b}}$ from theory. Below the last column of this table is repeated. The $C_{\text{m:b}}$ found in this thesis is added to this table.

Research	$C_{\text{m:b}}$
Dean and Dalrymple [1991]	-
Dessens [2004]	39.2 - 39.6
Tromp [2004]	4.85 - 9.375
This thesis	23.0

The value of $C_{\text{m:b}}$ is approximately in the middle of the values found by Dessens [2004] and Tromp [2004]. So the value of $C_{\text{m:b}}$ obtained from the correlation analysis is at least situated within an interval of values that are found before. Not a lot is known about $C_{\text{m:b}}$ in literature. Difference in this value can be due to a lot of reasons, like for example:

- the way of determining the force due to acceleration (e.g. depth-averaged, advective acceleration, temporal acceleration, close to the bed, from velocity gradients, from pressure gradients)
- the way of determining the associated velocity force (e.g. depth-averaged, close to the bed, maximum velocities near the bed, etc)
- the way of including of the effects of turbulence (e.g. correction factors, explicit incorporation)

All of the above can be a cause of the change in the ratio between the velocity force and the acceleration force. The value of $C_{\text{m:b}} = 23.0$ is located within a range of earlier found values of $C_{\text{m:b}}$. The exact reason for this is unknown. For now it is concluded that $C_{\text{m:b}} = 23.0$ is a plausible value for $C_{\text{m:b}}$ because it is within the range and it predicts the effects of acceleration correctly in the stability parameter.

The highest correlation is found when the advective acceleration at h_a/d_{n50}=9.0 is used. Figures 5-2 and 5-1 are repeated below. The height h_a is indictated with the black horizontal line.

In figure 6-12 it is clearly observable that the advective acceleration is determined at the height where the acceleration reaches its approximately constant value. The value of the pressure gradient is equal over the entire water column.

Figure 6-13 shows the height above the bed for the short sill configuration. Here the acceleration occurred due to an obstacle in the vertical, so the profiles are not of the same form as in figure 6-12. However, for some of the profile it is still observed that the advective acceleration is determined at the height where the acceleration is approximately equal to the pressure gradient.

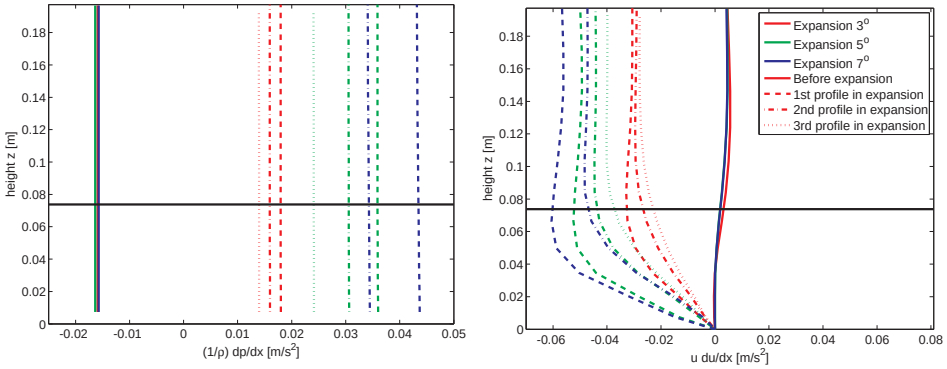

(a) Pressure gradient *(b) Advective acceleration*

Figure 6-12 Profiles from the expansion simulation from Hoan [2008]

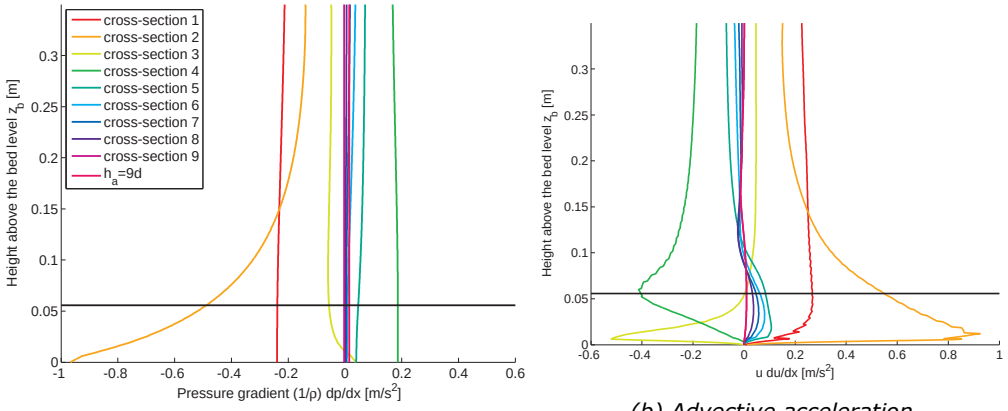

(a) Pressure gradient2 *(b) Advective acceleration*

Figure 6-13 Profiles from the short sill simulation

Figure 6-14 gives the advective acceleration profile for one of the contraction configurations of Dessens [2004]. Again the height h_a is indicated. Again the height $h_a = 9.0 \cdot d_{n50}$ determines the advective acceleration at the level where it is more or less constant. The pressure gradient profiles are unknown for this case. It is suspected that these have the same characteristics as the expansion, but reversed.

From the above it is concluded $h_a/d_{n50} = 9.0$ determines the advective acceleration at the heights were the acceleration is more ore less constant for the expansion and the contraction. For the sill, the acceleration is determined at the level where the advective acceleration is approximately equal to the pressure gradient near the bed. The behaviour of h_a in all of the configurations raises the suspicion that the pressure gradient $\frac{1}{\rho}\frac{\partial p}{\partial x}$ might even be a better measure for the force due to acceleration. The pressure gradient has the advantage that it is much less influenced by the bed than the advective acceleration term. Also, the pressure gradient is tried to be approximated by means of the advective acceleration. The relation between the advective acceleration

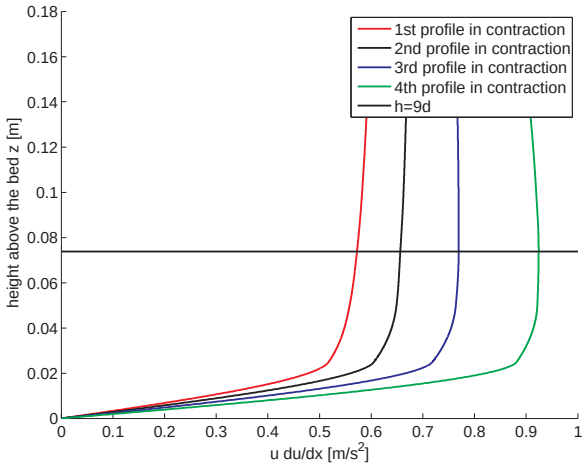

Figure 6-14 The advective acceleration profiles for the contraction

and the pressure gradient required assumptions and is just an approximation. The shortcomings caused by these assumptions can be avoided by using the pressure gradient directly. The pressure gradient was not available for all of the configurations, so this could not be done in this thesis. The pressure gradient can be obtained when computational methods are used to calculate the stability.

The height h_a was set depended on the stone diameter, because the advective acceleration profiles are clearly influenced by the bed. Also, it was observed that the water level did not have much influence on the advective acceleration profile. Based on the value of $h_a/d_{n50} = 9.0$ in the figures, this choice seems plausible. For both the expansion ($d_{n50} = 0.0082$m and the short sill ($d_{n50} = 0.0062$m the acceleration at this height approximates the pressure gradient near the bed.

6.4 Application of the new stability relation

This section gives an example of a calculation with the stability parameter Ψ_{RS}. The design of granular bed protections comes down to estimating a stone size that is stable but also with not too hight costs. Below some steps are given that have to be taken to find this stone size. Note that the determination of the required stone size is an iterative process, because the changing the stone size also changes the flow. Jongeling et al. [2006] states that one iteration step is sufficient. The steps that should be taken in the design process of a bed protection with Ψ_{RS} for an arbitrary situation are given below. Note that here just the deterministic approach is given, but that a probabilistic approach is possible.

1. Determine the acceptable dimensionless entrainment rate, the 'critical' or 'design' entrainment rate $\Phi_{E,c}$
2. Calculate the associated 'critical' stability parameter $\Psi_{RS,c}$ with equation 6-3
3. Estimate a preliminary design stone size d_p
4. Model the desired flow situation with stone size d_p with a numerical model
5. Use the output of the numerical model to calculate the stability parameter $\Psi_{RS,p}$ with equation 6-2 at every location
6. Compare the calculated $\Psi_{RS,p}$ with the critical $\Psi_{RS,c}$
7. Recognize the weak and strong spots in the bed protections, i.e. where does $\Psi_{RS,p}$ exceed $\Psi_{RS,c}$?

8. Increase d_p where necessary with:

$$d_{design} = \gamma \frac{\Psi_{RS,p}}{\Psi_{RS,c}} d_p$$

The γ is a safety factor that accounts for the the inaccuracy of the model and the stability relations. Hofland [2005] suggest a value of at least 1.5.

9. Repeat from step 4 until Ψ_{RS} is smaller than $\Psi_{RS,c}$ at every location. The d_{design} that is found is the stone size that can be used in the bed protection.

The remainder of this section discusses some calculations with the stability parameter Ψ_{RS} to get a feeling of the strengths and weaknesses of the new stability assessment method. Section 6.4.1 compares the stone size calculated with Ψ_{RS} to the stone size calculated with Ψ_{Lm} for the configuration with the most notable accelerations, the contraction. Section 6.4.2 compares the stability parameter Ψ_{RS} obtained from the measurements to the Ψ_{RS} that would be calculated if the model from section 3 was used.

6.4.1 Calculated stone size

The required stone size in the contraction with an angle of 6.65° is calculated in this section. The steps described above are followed to find this stone size. Both Ψ_{RS} and Ψ_{Lm} are used and at the end the found stone sizes are compared and evaluated.

The acceptable dimensionless entrainment rate to $\Phi_{E,c} = 1.0 \cdot 10^{-9}$ which is approximately equal to the flat bed case from Jongeling et al. [2003]. This value is pure for illustration of the method. With equation 6-3 the critical stability parameter is found:

$$\Psi_{RS,c} = \left(\frac{1.0 \cdot 10^{-9}}{3.95 \cdot 10^{-9}} \right)^{1/5.89} = 0.79$$

For $\Psi_{Lm,c}$ this is also done with equation2-45, resulting in $\Psi_{Lm,c} = 0.51$.

A preliminary estimate for the stone size is done. A $d_{preliminary}$ of 0.0082 m is used. The Ψ_{RS} Ψ_{Lm} are calculated with equation 6-2. The measurements of Dessens [2004] are used as input for the stability parameters. Table 6-4 gives the results for different profiles in the contraction. Profile 1 is situated at the start of the contraction and profile 4 at the end.

	Profile 1	**Profile 2**	**Profile 3**	**Profile 4**
Ψ_{RS} [-]	1.3312	1.7373	2.4418	3.6160
Ψ_{Lm} [-]	0.5238	0.6740	0.8874	1.2056

Table 6-4 The stability parameters in the contraction with an angle of 6.65°

For the profiles where $\Psi > \Psi_c$, d_{design} can be calculated using:

$$d_{design} = \gamma \frac{\Psi_{RS,p}}{\Psi_{RS,c}} d_p$$

$$d_{design} = \gamma \frac{\Psi_{Lm,p}}{\Psi_{Lm,c}} d_p$$

A safety factor of 1.0 is used here to only show the effect of the design method on the stone dia-

meter. Because the calculation is just an example only one iteration step is used. The calculated stone sizes are given in table 6-5.

	Profile 1	Profile 2	Profile 3	Profile 4
d_{RS} [m]	0.0138	0.0180	0.0253	0.0375
d_{Lm}[m]	0.0084	0.0108	0.0143	0.0194

Table 6-5 The calculated stone diamaters in the contraction with an angle of 6.65°

Due to the underestimation of the effects of the acceleration the stone sizes calculated with Ψ_{Lm} are much lower than the stone sizes calculated with d_{RS}. Using Ψ_{Lm} in the contraction would lead to unforeseen damage to the bed protection.

6.4.2 Measured stability parameter vs. modelled stability parameter

The stability parameter Ψ_{RS} and its relation with Φ_E are derived using measured flow properties. When the method is used for the design of a bed protection, no such measurements are available. In this case a numerical model is used as input for the stability parameter. The numerical introduces additional errors in the method. For example in section 3 it is noticed that obtaining the correct turbulence characteristics is not that easy. In this section the effect of these errors on the calculated entrainment is investigated.

The measured values of $\Psi_{RS,meas}$ for the short sill are compared to the values of $\Psi_{RS,comp}$ that are calculated with the model from section 3.4. The results are shown in table 6-6 in which also the actual occurring Φ_E can be found.

Table 6-6 shows that the entrainment rate based on measurements $\Phi_{E,meas}$ is within the same order of magnitude as the actual entrainment rate Φ_E. Although the calculated entrainment rate based on measurements is a factor 3-4 larger than the actual entrainment in most of the profiles.

The entrainment rate based on the model $\Phi_{E,comp}$ is approximately equal to $\Phi_{E,meas}$ in the first three profiles. After the third profile, both entrainment rates start to deviate. Section 3.4 showed that the turbulent kinetic energy is not modelled correctly behind the sill. This is the cause of the deviation in Ψ_{RS} and thus in the calculation of the entrainment rate.

It is concluded that it is possible to use the new stability assessment method with the output of numerical models, provided that the model predicts the velocity and turbulence characteristics accurately. Part of the uncertainty in the new stability assessment method that uses Ψ_{RS} comes from the uncertainties in the modelling of the flow.

	1	2	3	4	5	6	7	8	9	10
Calculated based on measurements:										
$\Psi_{RS,meas}$	1.7	2.3	2.6	1.9	1.9	1.8	1.9	1.8	1.5	1.4
$\Phi_{E,meas}$[·1e-6]	0.09	0.50	1.15	0.17	0.20	0.13	0.15	0.11	0.04	0.03
Calculated based on model:										
$\Psi_{RS,comp}$	1.7	2.4	2.6	1.5	1.5	1.5	1.4	1.4	1.3	1.2
$\Phi_{E,comp}$ [·1e-6]	0.08	0.6	1.08	0.05	0.04	0.04	0.03	0.03	0.02	0.01
Actual:										
Φ_E(·1e-6)	0.03	0.18	0.18	0.04	0.05	0.06	0.06	0.03	0.02	0.03

Table 6-6 The calculated Ψ_{RS} and the resulting Φ_E for the measured and the modelled flow characteristics in different cross-sections

7 Discussion

The stability parameter Ψ_{RS} that is proposed in this thesis includes the following forces on the stones:

- The quasi-steady forces (i.e. the mean velocity and the velocities that reach the bed);
- The forces due to the pressure gradient in advective acceleration;
- A resisting force (i.e. the weight of the stone);
- A correction for sloped beds.

There already exist stability parameters that are developed to include the effects of turbulence properly in non-uniform flow (Jongeling et al. [2003], Hofland [2005] and Hoan [2008]). Also some effort has been made to include the effects of acceleration on stone stability based on depth-averaged flow quantities(Dessens [2004], Tromp [2004] and Huijsmans [2006]).

The proposed stability parameter Ψ_{RS} is the first stability parameter that includes both of the effects into one stability parameter. The stability parameter uses flow properties from whole water column and can be applied to non-uniform flow.

The existing stability parameters are all derived for one specific situation. The range of application for these stability parameters is therefore not very large. The relation of the stability parameter Ψ_{RS} and the dimensionless entrainment rate Φ_E is derived with a large variety of flow conditions. In total 209 simultaneous measurements of flow characteristics and bed response are used to derive the relation. The proposed stability parameter can therefore be applied in a much larger range of flow conditions than the existing stability parameters. The inclusion of the effect of acceleration leads to a increase of the correlation from $R^2 = 0.27$ to $R^2 = 0.80$.

7.1 Causes of the remaining scatter

The raw measurement data is used and processed in exactly the same way for all data sets to minimize the error. However, there is still scatter of the data points present when Ψ_{RS} is used. Below a number of reasons for the scatter is given.

Turbulent wall pressures are not included
A force generating mechanism that is not included in Ψ_{RS}. Hofland [2005] states that the turbulent wall pressures cause the stone to lift up a little, after which the stone is transported by the quasi-steady forces. The turbulent wall pressures thus cause an increased probability that stones transported. This effect is still not included in the stability parameter.

Measurement errors
The stability parameter is derived using measurement data. Measurements always contain errors. Different measurement instruments have different accuracies. For example an LDS measures more accurately and with a larger frequency than an EMS. Measurement errors can also arise because of an error or the person that is measuring.

Modelling errors
The acceleration for two configurations is determined with the output of a numerical model. The output can contain errors. The source of errors in numerical models are for example the mesh and boundary condition set-up or the used numerical schemes.

Errors in data processing
The data processing is done as consistent as possible. However, not all of the data sets are equal. Some data sets contained less data points than the others. Therefore, not all of the

processed data is equally accurate.

The determination of the acceleration force
In this thesis the advective acceleration at a certain height above the bed was used to calculate the force due to acceleration. The advective acceleration is used as approximation for the pressure gradient over the length of the stone. This approximation is based on assumptions that are not entirely true and thus introduces errors.

7.2 Limitations

The proposed stability parameter has the following limitations:

Only applicable for advective acceleration
The proposed stability parameter and the relation with the bed response are derived only for advective acceleration. The effect of time-dependent acceleration is not included in this way. In bed protections in an environment with waves, like around a breakwater, these effects can be of importance. Acceleration in time is associated with other mechanisms like a change in boundary layer over time. In this thesis, the turbulence is added by an approximation of the standard deviation of the mean velocity. This is basically equal to an extreme event caused by turbulence that has a certain probability to occur within a time interval. If this time interval is very short, it is not known whether this method of including the turbulence is still applicable.

Only the ratio between C_b and C_m is known
In this thesis not the exact values of C_b and C_m is found. Instead of that the ratio between the two, $C_{m:b}$, is determined. For the relation with the bed response this has no influence. To say something about the actual forces that are exerted on the stones, the actual values of these constants have to be known. This could not be done with the information in this thesis.

The value of $C_{m:b}$ and α for low transport
At low transport, the turbulence has a larger influence on the transport than at high transport. At low transport the extremes caused by turbulence are required to even get movement of stones. All of the transport is caused by extreme events. At high transport, movement of stones already occurred because of the velocities and the accelerations. Extreme events of turbulence cause some extra movement once in a while, but the influence is relatively much lower in this case. At low transport, the value of $C_{m:b}$ and α is probably different than the ones found in this thesis.

7.3 Practical relevance

The proposed stability parameter can be used in the design of bed protections. The incorporation of the effects of acceleration and the increased range of application lead to a more accurate estimation method for the stability of bed protection.

In an example of the use of the new stability parameter, it is shown that the effect of acceleration has a considerable influence on the required stone size. The new stability assessment method can be used to recognize the areas where larger stones are required in the design of a bed protection under non-uniform flows. This can lead to more efficient design where large stones are only applied at locations where this is necessary.

Both the effects of turbulence and the effects of acceleration are now included into one stability parameter. In civil engineering practice acceleration followed by decelerations (with extra turbulence) is a quite common situation. When water flows around, through or over structures this is almost always the case. The new stability assessment method can be applied to these situ-

ations.

In practice often scale models are used to design granular bed protections. Although the proposed stability parameter reduces the scatter considerably, scale models are probably still necessary. However, the new stability assessment method is one step closer to the design purely based on computer models.

In this thesis the stability parameter calculated based on measurements is compared to the stability parameter based on a numerical model. It is concluded that the new stability assessment method predicts the entrainment rate reasonably well, provided that the numerical model is accurate. Next to the scatter described before, part of the uncertainties in the method are due to the errors in numerical modelling. Computational power grows very fast and numerical methods get more and more efficient, so in the future this problem will be of less importance. For now, using the new stability assessment method requires accurate computation models. Special care should be taken to the mesh and boundary set-up.

8 Conclusions and Recommendations

This thesis started with the formulation of the following research questions:

Q1 What are the forces that are exerted on the stones by the flow?
   a. Which mechanisms cause forces on the stones?
   b. Which expressions can be used to describe the flow forces?
   c. Which flow variables are needed to calculate the flow forces?

Q2 Which data sets that contain simultaneous measurements of the required flow variables and the bed response are available?

Q3 Which flow forces can be included in the stability parameter?

Q4 Can the missing data be reconstructed with the use of numerical models?

Q5 Which methods are available to describe the bed response of granular bed protections?

Q6 What mathematical description can be used for the relation between a stability parameter and the bed response?

Q7 What is the relation between the derived stability parameter and the bed response?

Q8 What is the practical relevance of the stability relation and what uncertainties remain in the prediction of the bed response?

Section 8.1 gives the most important conclusions of this thesis. The chapter is concluded with recommendations for further research that can be done to improve the method of stone stability assessment in section 8.2.

8.1 Conclusions

The stability of stones in bed protections is influenced by the quasi-steady forces, turbulent wall pressures and pressure gradients due to acceleration. Existing stability assessment methods do not incorporate all of these forces and are usually derived only one of these forces. The methods are only applicable in the range for which they are derived, which usually is a limited number of flow conditions and geometries.

This thesis proposes ads the force due to acceleration to the existing parameter of Hofland [2005], that was derived to incorporate the turbulence properly. The stability parameter is given by:

$$\Psi_{RS} \equiv \frac{\left(\max\left[\left\langle \overline{u} + \alpha\sqrt{k}\right\rangle_{Lm} \frac{L_m}{z}\right]^2\right) + C_{m:b}\left(\overline{u}\frac{\partial \overline{u}}{\partial x}\right)_{h_a} d}{K(\beta)\cdot \Delta g d}$$

With:

α = 3.75 [-]
$C_{m:b}$ = 23.0 [-]
h_a $9.0 \cdot d_{n50}$ [m]

Measurements in a wide range of flow conditions and geometries are used to find the constants in the proposed stability parameter. Missing data on velocity profiles and acceleration is reconstructed by means of a computational model in the software package OpenFOAM. Because of 3D effects in the measurements, the turbulence properties show large deviations with the measurements. The velocity profiles are reconstructed good enough to use for the calculation of the acceleration.

A correlation analysis based on measurements and model output in flow over a flat bed, over different types of sills, through a contraction and through an expansion leads to the values of the constants. The coefficient of determination for the correlation with the dimensionless entrainment rate is $R^2 = 0.80$ for these constants. Compared to the stability parameter of Hofland [2005] (with $\alpha = 3.0$), that results in a R^2 of 0.27, this is an improvement in R^2 of 0.53. Including the effects of acceleration to the stability parameter leads to a significant improvement in the prediction of the bed damage.

The relation of the stability parameter and the entrainment rate is given by:

$$\Phi_E \equiv 3.95 \cdot 10^{-9} \Psi_{RS}^{5.89} \qquad \text{for } 0.9 < \Psi_{RS} < 4.3 \tag{8-1}$$

The figure below shows the stability relation, together with the data points.

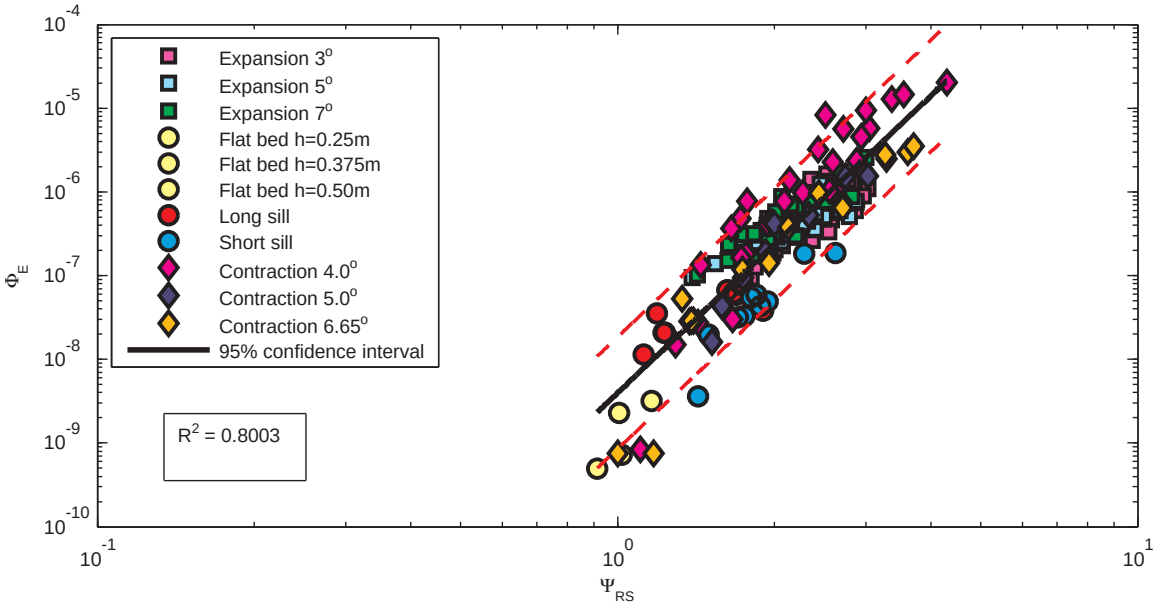

The performance of several existing stability parameters was checked for the entire data set that was used in this thesis. The Shields parameter Ψ_S determines the bed damage in uniform flow cases correctly. In accelerating flow, the Shields parameter shows the right trend. However, this is because in accelerating flow the velocity near the bed, and thus the bed shear stress, is larger. The effect of the actual pressure gradient due to acceleration is not incorporated by the Shields parameter. The Shields parameter does not show the right behaviour at all for flows with a lot of turbulence. In decelerating flow (i.e. the bed shear stress decreases), the Shields parameter predicts smaller entrainment. In reality larger entrainment is observed, due to the increased turbulence.

The Dessens parameter Ψ_{MS} performs reasonably for situations with relatively small turbulence. The behaviour of the forces due to acceleration is incorporated correctly in the parameter. For situations with high turbulence, however, Ψ_{MS} does not predict the measurement correctly. Dessens [2004] gives an equation for the relative turbulence in the contraction. For the other configurations there are no such relations and thus is the effect of turbulence not incorporated correctly.

The Hofland stability parameter Ψ_{Lm} incorporates the behaviour of turbulence correctly. In situ-

ations with large accelerations, the entrainment rate is underestimated. This difference is attributed to the force due to acceleration.

The proposed stability parameter Ψ_{RS} shows the right behaviour for accelerating as well as for decelerating flow. In accelerating flow an extra destabilizing force is exerted on the stones, due to the negative pressure gradient. In decelerating flow the positive pressure gradient causes a stabilizing force in the opposite direction of the flow.

The values of α and $C_{m:b}$ are within the range of values that are derived earlier. The value of α is somewhat higher than in theory. This can be explained by the fact that the situations with the highest decelerations often also have the highest turbulence. The situations with high turbulence are influenced more by the deceleration that the situations with low turbulence. The increased value of the relative turbulence α counteracts this effect.

The force due to acceleration is determined by the advective acceleration at a height h_a above the bed. This height depends on the stone diameter d_{n50}. A height of $h_a/d_{n50} = 9.0$ leads to the highest correlation according to the correlation analysis. This is the height above the bed above which the advective acceleration becomes constant and where the absolute value is approximately equal to the pressure gradient. This indicates that the pressure gradient might also be an appropriate measure for the force due to acceleration.

The stability parameter Ψ_{RS} can be used in the design of bed protections to recognize the areas of where larger stones are required. This can result in more efficient design. The Ψ_{RS} leads to a larger required stone size than Ψ_{Lm} in accelerating flow.

An important uncertainty in the model are the flow properties that are used as input for the stability calculations. For this a computational model is required. It is concluded that the stability relation derived in this thesis predicts the entrainment reasonably well, but that the input in the stability parameter has to be accurate. Boundary conditions and mesh set-up are very important for an accurate solution. The outcome of the stability calculations is very sensitive to errors in the computational model.

8.2 Recommendations

This thesis leads to the following recommendation to improve the method of stability assessment.

Test the performance of the proposed relation in a validation case
In this thesis, all of the available data sets have been used to derive the relation with. The performance of the stability assessment method should be tested on a case in which the bed response is known. By modelling the case numerically and applying the new method, it could be checked whether the method gives useful results.

Include the effect of time dependent accelerations
The effect of acceleration in time due to for example waves has not been investigated in this thesis. To make the stability parameter more general, this effect could also be included. In time dependent acceleration, certain flow conditions are working only temporarily. The turbulence in this method was incorporated by adding an approximation of the standard deviation of the velocity to the mean velocity, which basically is equal to an extreme event caused by turbulence that happens a certain number of times within a time interval. If this time interval is very short (like in waves) it is not known whether this method of including the turbulence is still applicable.

Including the effects TWP
The turbulent wall pressures that were discussed in section 2.3 have not been included in this thesis because it would require too much measurement data on micro scale. However, in Hof-

land [2005] it is mentioned that these forces could be of importance in the entrainment mechanism. The TWP cause a stone to be lifted for a moment. At that moment the quasi-steady forces caused by the combination of velocity and turbulence can cause transport of stone. This causes an increased probability of transport of stones that is not included in the current stability parameter. If the frequency is known at which the combination of TWP and maximum QSF occurs, these effects can be added to the stability parameter. Hofland [2005] suggest the method described in Uittenbogaard et al. [1998].

Determine the force on a stone with the pressure gradient

The height where the advective acceleration is determined, is found by means of a correlation analysis. In most of the cases this was at the height where value of the advective acceleration was approximately equal to the absolute value of the pressure gradient. This indicates that the pressure gradient might also be an appropriate measure for the force due to acceleration. To do this the configurations should all be modelled numerically.

Investigating the values of the constants for (very) low transport

At low transport, the value of α and $C_{m:b}$ might be different. At very low transport the effect of the turbulence on the transport is larger because this is the only force that causes movement. Including this effects leads to more accurate predictions of the damage at low transport.

Improved numerical modelling

Because the numerical modelling in this thesis was not the main objective, not too much time was spend in optimizing the model results. To obtain a more accurate relation the model results should be improved. The main reason for the deviations of the model output compared to the measurements were the 3D effects in the flume. To obtain more realistic results the configurations have to be modelled in 3D. This probably also will lead to a solution that is less influenced by the inflow boundary. Since the method of using numerical models complementary to measurements has proved to give reasonable results, one could also choose to model the contraction cases numerically.

List of Symbols

Symbol	Description	Units
$\frac{Du}{Dt}$	material derivative	[m s^{-2}]
α	empirical factor	[-]
δ	relative density $\rho_s - \rho_w)/\rho_w$	[-]
γ	relative depth z/h	[-]
κ	von Karmann constant $\kappa \approx 0.41$	[-]
μ	dynamic viscosity	[kg m^{-1} s^{-2}]
∇	nabla operator	[-]
ν	kinematic viscosity	[m^2 s^{-1}]
ν_t	turbulent viscosity	[m^2 s^{-1}]
ω	large scale turbulent frequency	[s^{-1}]
$\overline{a}$	mean part of the acceleration	[m s^{-2}]
$\overline{u}$	mean part of the velocity	[m s^{-1}]
ϕ	angle of repose	[$^\circ$]
Φ_E	dimensionless entrainment rate	[-]
Φ_q	dimensionless bed load transport rate	[-]
Ψ_{Lm}	Hofland stability parameter	[-]
Ψ_{RS}	Proposed stability parameter	[-]
$\Psi_{u-\sigma(u)}$	Hoan stability parameter	[-]
Ψ_{WL}	Jongeling stability parameter	[-]
Ψ_S	Shields stability parameter	[-]
ρ	denisity	[kg m^{-3}]
σ	standard deviation	
τ	viscous shear stress	[N m^{-2}]
τ_b	bed stress	[N m^{-2}]
$\tilde{a}$	acceleration projected on the bed	[m s^{-2}]
$\tilde{u}$	velocity projected on the bed	[m s^{-1}]
A	surface area	[m^2]
a'	fluctuating part of the acceleration	[m s^{-2}]
B	width	[m]
C_μ	constant from the $k-\omega$ SST model	[-]
C_b	bulk coefficient	[-]
C_D	drag coefficient	[-]
C_k	drag coefficient	[-]
C_L	lift coefficient	[-]
C_m	added mass coefficient	[-]
C_s	roughness constant	[-]
d	stone diameter	[m]
d_{n50}	nominal stone diameter	[m]
E	entrainment rate	[m s^{-1}]
F_D	drag force	[N]
F_L	lift force	[N]
Fr	Froude number	[-]
g	the gravitational acceleration	[m s^{-2}]
h	water depth	[m]
h_a	acceleration depth	[m]

i	energy slope	[m/m]
k	turbulent kinetic energy	[m^2 s^{-2}]
k	OpenFOAM turbulent kinetic energy	[m^2 s^{-2}]
K	correction factors	[-]
k_s	Nikuradse roughness	[m]
l_m	mixing length	[m]
n	number of moved stones	[-]
p	the pressure	[N m^{-2}]
q_s	bed load transport	[m s^{-2}]
Re	Reynolds number	[-]
SSE	sum of errors squared	[-]
T	time	[s]
TSS	total of errors squared	[-]
U	velocity vector [u_x u_y u_z]	[m s^{-1}]
U	OpenFOAM velocity	[m s^{-1}]
u'	fluctuating part of the velocity	[m s^{-1}]
u_τ	friction velocity	[m s^{-1}]
u_b	velocity along the bed	[m s^{-1}]
u_x	velocity in x direction	[m s^{-1}]
u_y	velocity in y direction	[m s^{-1}]
u_z	velocity in z direction	[m s^{-1}]
V	volume	[m^3]
x	horizontal dominant flow direction	[m]
y	transversal direction	[m]
z	vertical direction	[m]
z_0	equivalent roughness height	[m]

Appendices

A Turbulence

A.1 Turbulence in general

Flows in civil engineering are almost always turbulent. This means that the fluid motion is highly random, unsteady and three-dimensional (Rodi [1980]). Reynolds [1883] was the first one to make a distinction between laminar or turbulent flow regimes in 1883. He found from experiments that whether flow was laminar or turbulent depends on the Reynolds number. The Reynolds number can be defined as the ratio between inertial forces and viscous forces, and is given by:

$$Re = \frac{UL}{\nu} = \frac{UL}{\nu} \tag{A-1}$$

When $Re > 4000$, the flow is turbulent (which is the case in the majority of the cases within the field of civil engineering). A definition of turbulence according to Hinze [1975] is: "Turbulent fluid motion is an irregular motion, but statistically distinct average values can be discerned and can be described by laws of probability". Some key features of turbulence by Tennekes and Lumley [1972] are:

- Irregularity;
- Diffustivity;
- Large Reynolds numbers;
- Three-dimensional vorticity fluctuations;
- Dissipation;
- Continuum;
- Turbulent flows are flows;

A.2 Energy equations

When looking at the energy equations (see Uijttewaal [2011]), it can be seen that the energy that is lost from the mean motion is gained by the turbulent fluctuations. In this turbulent motion, distinction can be made between macrostructures and microstructures. Macrostructures are characterized by large-scale eddies. The kinetic energy from the mean motion is entrained into the turbulent motion at macro-scale by the work done by the Reynolds stresses, which means there is a loss of kinetic energy from the mean motion. In a stationary flow this should be balanced by the work done by external forces. At the macro scale, the energy losses due to the work done by the Reynolds stresses are much larger than the viscous effects.

The turbulent kinetic energy is dissipated (transferred into heat) at the smallest scales of turbulence, the Kolmogorov micro scales. At these scales, the viscous effects dominate the dynamics. It can be said that the energy that enters the turbulent motions on a scale where viscosity does not play a role is continuously transferred to smaller scales until viscosity starts to become dominant. This process is called the energy cascade and is sketched in figure A-1.

The dissipation rate on the macro scales can be estimated by stating that the energy from the mean flow U^2 is dissipated in a time L/U, with U the velocity and L the length scale. The dissipation rate can then be estimated by $\varepsilon = U^3/L$. The flux of energy that enters the turbulent motions at the large-scale side must be the same as that associated with viscous dissipation. Therefore, the dominant dissipative scale should be scalable with the dissipation and viscosity.

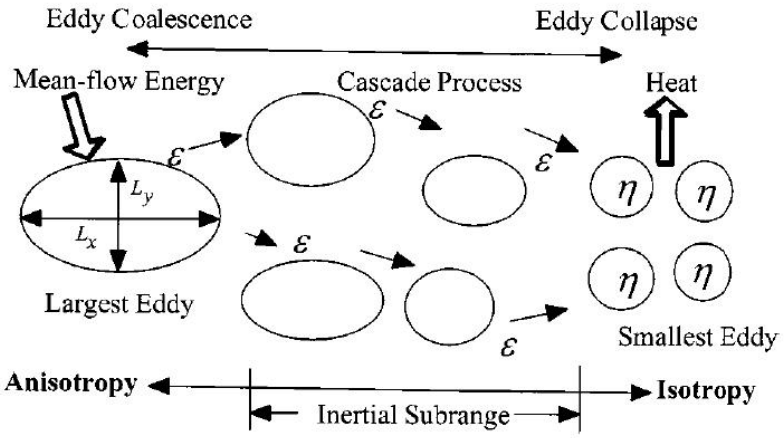

Figure A-1 Sketch of the energy cascade process

Dimensions analysis gives the Kolmogorov scales (λ_{kolm}, τ_{kolm} and υ_{kolm} for respectively length, time and velocity):

$$\lambda_{kolm} = \left(\frac{\nu^3}{\varepsilon}\right)^{\frac{1}{4}} \qquad \tau_{kolm} = \left(\frac{\nu}{\varepsilon}\right)^{\frac{1}{2}} \qquad \upsilon_{kolm} = (\nu\varepsilon)^{\frac{1}{4}} \qquad Re = \frac{\upsilon\lambda}{\nu} = 1 \tag{A-2}$$

The Reynolds number that can be calculated with the above Kolmogorov scales is 1. This is also the value below which the viscosity becomes dominant.

Via a spectral analysis, the distribution of the turbulent kinetic energy over the different length scales can be obtained. A rough sketch of such a distribution is given in figure A-2. The macro structure contains most of the energy in the form of large eddies, with a length scale of the order of the geometry. The mean motion always has a preferred direction, causing that the largest anisotropy is found in this region. At the dissipating end of the spectrum, the smallest (Kolmogorov) scales are found, which are isotropic.

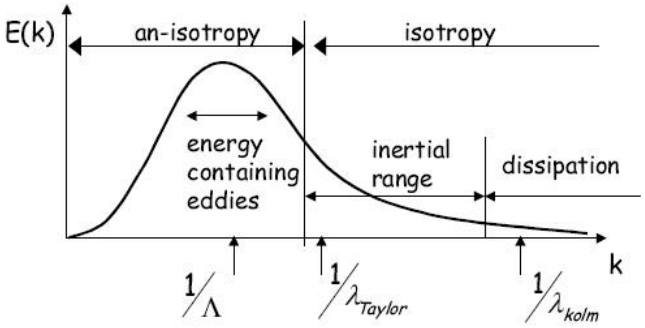

Figure A-2 The distribution of the turbulent kinetic energy over a range of length scales(from Uijttewaal [2011])

A.3 Taylor's hypothesis

When observing turbulence phenomena, visually clear eddying motions and whirls are visible. This would mean that turbulence has, next to a certain time scale, also has a certain extension in space. The Taylor hypothesis describes that an eddy does not change during the passage of some point. In this way, turbulence can be seen as a field in which the eddies are frozen and

passes with a certain constant velocity. Although definitely not always true, Taylor's hypothesis is very useful to make interpretations for measurements at a single point.

B Acceleration Force

This appendix gives the derivation from Dessens [2004] of the description of the force on a stone due to acceleration. In figure 2-7 a simplified representation was given. This figure is repeated below.

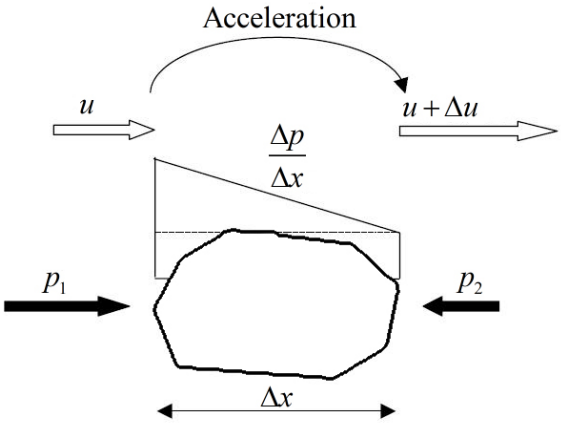

Figure B-1 The pressure difference due to acceleration from Dessens [2004]

When the stone is assumed to be very small compared to the variations in the flow, the pressure at each side of the stone can be approximated by the first two terms in a Taylor series expansion. The pressure $p_1 = p$ and the pressure $p_2 = p + \Delta p$. The pressure difference Δp is approximated by:

$$\Delta p = \frac{\Delta p}{\Delta x} dx \tag{B-1}$$

The force on a stone caused by this pressure difference can be expressed as $A\Delta p$ with A the surface area $\Delta y \Delta z$ of the stone. Integrated over the surface area of the stone, the force on the stone remains. In this equation V is the volume of the stone and the force is positive in x direction:

$$F = \iiint \frac{\Delta p}{\Delta x} \Delta x \Delta y \Delta z = -V \frac{\Delta p}{\Delta x} \tag{B-2}$$

When only pressure forces are considered, conservation of momentum leads to the Euler equation (for inviscid flow, see Battjes [2002]):

$$\rho \frac{Du}{Dt} = -\nabla p + \rho g \tag{B-3}$$

For the dominant flow velocity u_x this equation can be written as:

$$\rho \frac{Du_x}{Dt} = \rho \left(\frac{du_x}{dt} + u_x \frac{\partial u_x}{\partial x} + u_y \frac{\partial u_x}{\partial y} + u_z \frac{\partial u_x}{\partial z} \right) = -\frac{\partial p}{\partial x} \tag{B-4}$$

Combining equations B-4 and B-2 leads to equation B-5:

$$F_a = -V\frac{\partial p}{\partial x} = \rho V\left(\frac{\partial u_x}{\partial t} + u_x\frac{\partial u_x}{\partial x} + u_y\frac{\partial u_x}{\partial y} + u_z\frac{\partial u_x}{\partial z}\right) \tag{B-5}$$

In this thesis only advective acceleration is considered and the velocity and velocity gradient in lateral direction are assumed to be small. This reduces equation B-5 to equation B-6.

$$F_a = -V\frac{\partial p}{\partial x} = \rho V\left(u_x\frac{\partial u_x}{\partial x} + u_z\frac{\partial u_x}{\partial z}\right) \tag{B-6}$$

C OpenFOAM

Figure C-1 shows the general case structure for a model in OpenFOAM. In this appendix the files that are needed for a OpenFOAM computatioin are discussed.

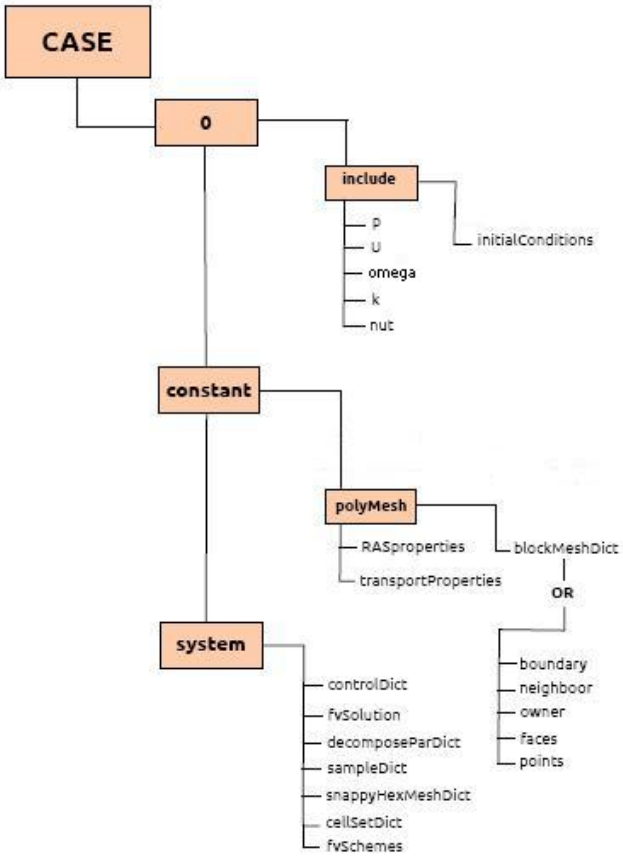

Figure C-1 Case structure in OpenFOAM (adapted from Martinez [2011])

C.1 The '0' directory

In this directory the initial and boundary conditions for each of the governing variables are specified in separate files. The files are named like the variables itself, e.g. `p`, `U`, `k`, `omega` and `nut` (stands for ν_t). In each of these files, a type of patch is specified for each boundary (see also Martinez [2011] and OpenFOAM Foundation [2012]). OpenFOAM distinguishes a base patch type (which is specified somewhere else and will be discussed later) and a primitive or derived patch types. The latter is the one specified in the files in the '0' directory. Examples of the patch types that are used in this thesis are shown in table C-1. Some of the patch types also require an initial condition.

Patch type	Description	Data to specify
`fixedValue`	The value of the variable is specified	`value`
`fixedGradient`	The normal gradient of the variable is specified	`gradient`
`zeroGradient`	The normal gradient of the variable is zero	-
`slip`	normal component of the variable is fixedValue zero and tangential components are zeroGradient	-
`nutRoughWallFunction`	Wall function for ν_t as described in equation 3-19	`ks`, `Cs`
`omegaWallFunction`	Wall function for ω as described in equation 3-21c	-

Table C-1 Primitive and derived patch types (from OpenFOAM Foundation [2012])

C.2 The 'constant' directory

The 'constant' directory contains information regarding the mesh, the turbulence model and model constants. The directory contains one folder containing information on the mesh (the polyMesh folder) and 3 files containing information on model constants and turbulence (*transportProperties*, *RASProperties* and *turbulenceProperties*, respectively).

The 'polyMesh' folder contains information on the mesh. In this thesis the mesh are all generated using the *blockMesh* utility of OpenFOAM (see OpenFOAM Foundation [2012] for a description of the *blockMesh* utility). A file called *blockMeshDict* should be included in the polyMesh folder. This file contains all of the information on the mesh that has to be used. Using the *blockMesh* utility additional files are generated containing the geometry of the mesh (*boundary*, *neighbour*, *faces*, *points* and *owner*). In the *blockMeshDict* file the basic patch types are specified, examples are given in table C-2.

Patch type	Description
patch	Generic patch without information about geometric or topological information about the mesh (with exception of the wall patch)
symmetryPlane	Plane of symmetry
empty	Front and back planes for 2D geometries
cyclic	Cyclic plane where the patches are treated as if they are physically connected
wall	Wall boundary used for wall functions

Table C-2 Basic patch types (from OpenFOAM Foundation [2012])

In the *transportProperties* file information on transport model constants is given (e.g. a Newtonian transport model or the value of the molecular viscosity nu). In the *turbulenceProperties* the method of turbulent closure (e.g. `laminar`, `LESModel` or `RASModel`) is specified and in the *RASProperties* file the used turbulence model is entered (e.g. `kEpsilon`, `kOmega` and `kOmegaSST`).

C.3 The 'system' directory

The last directory that is required is the 'system' directory. This directory contains the files associated with the solution procedure, additional files that are related to post-processing and files for parallel computations. All the files are discussed below together with an example of the file.

controlDict

The *controlDict* file contains information on the used solver, start and end times, time steps and writing intervals.

In this thesis, the `pimpleFoam` solver is used. The `pimpleFoam` solver is defined in OpenFOAM Foundation [2012] as a large time-step transient solver for incompressible flow using the PIMPLE (merged PISO-SIMPLE) algorithm for the velocity-pressure coupling. The PIMPLE approach combines the SIMPLE and PISO loops. In Jodar et al. [2012] the PIMPLE is described as follows:

1. Starting a new time step;
2. Solve the continuity equation;
3. Momentum predictor: here the velocity equation is defined, implicitly under relaxed and solved;
4. Inner loop: a predefined number of iterative pressure equation and momentum corrector loops;
5. Solve turbulent equations;
6. Outer loop: repeat steps 2 - 5 a predefined number of times

The flowchart of the PIMPLE algorithm is given in figure C-2. In this thesis, this information is considered sufficient and for more details one is referred to Ferziger and Peric [1999].

A typical *controlDict* file is shown in table C-3.

fvSchemes

In the *fvSchemes* file, the numerical schemes for the different terms of the equations can be specified. The following terms are given in OpenFOAM Foundation [2012]:

Term	Description
`ddtSchemes`	First and second time derivatives $\partial/\partial t$ and $\partial^2/\partial t^2$
`gradSchemes`	Gradient ∇
`divSchemes`	Divergence $\cdot\nabla$
`laplacianSchemes`	Laplacian ∇^2
`interpolationSchemes`	Point to point interpolations of values
`snGradSchemes`	Component of gradient normal to a cell face
`fluxRequired`	Fields which require the generation of a flux

In OpenFOAM, a number of different schemes are available for each term. For an overview of these schemes one is referred to OpenFOAM Foundation [2012]. OpenFOAM gives complete freedom in the schemes that are used and they can be specified in the way the user wants. In table C-4, the fvSchemes file that is used in this thesis is given.

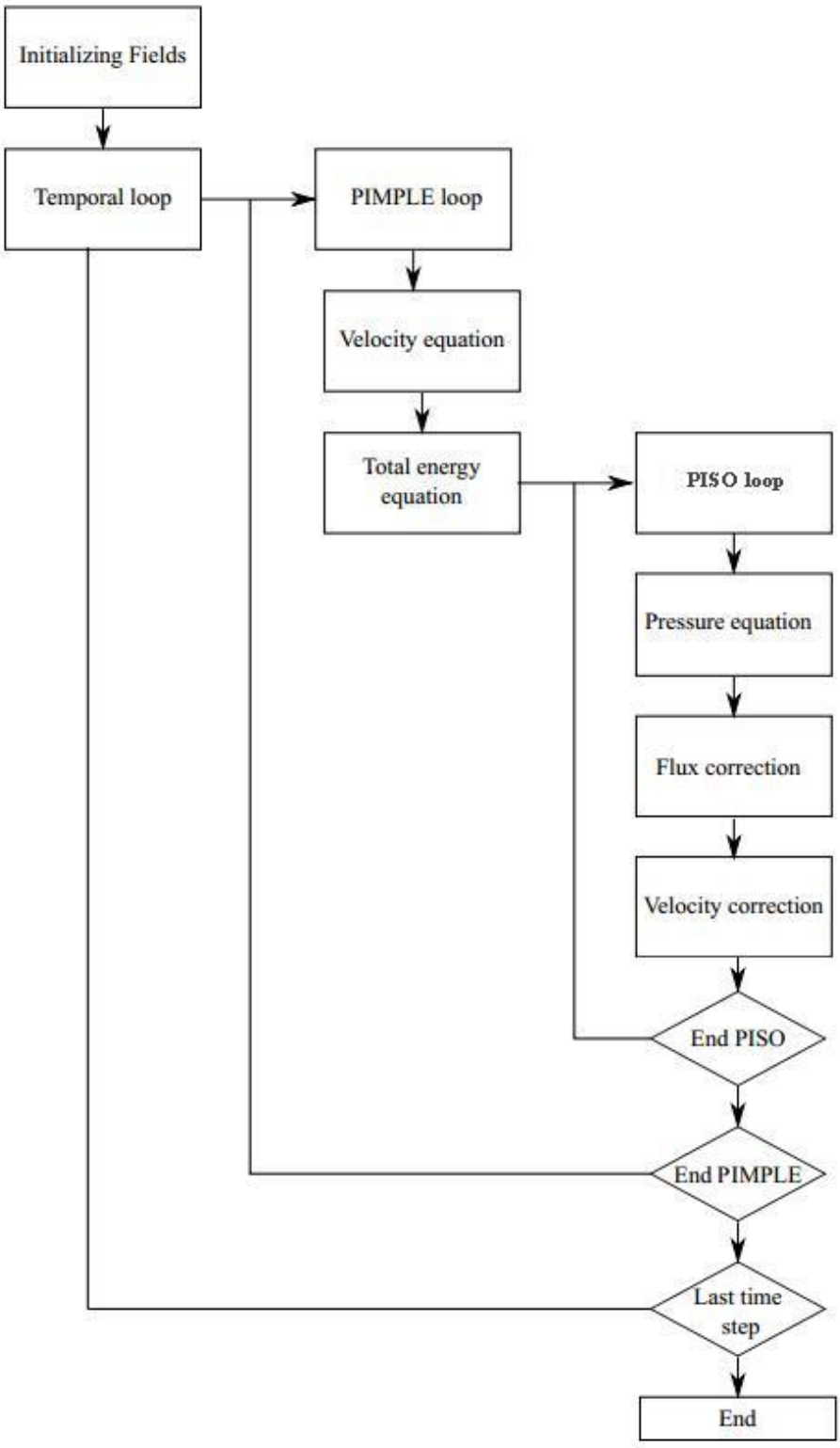

Figure C-2 Flowchart of the PIMPLE algorithm (from Aguerre et al. [2013])

```
application         pimpleFoam;

startFrom           startTime;

startTime           0;

stopAt              endTime;

endTime             200;

deltaT              0.0001;

writeControl        adjustableRunTime;

writeInterval       1;

purgeWrite          0;

writeFormat         ascii;

writePrecision      6;

writeCompression    uncompressed;

timeFormat          general;

timePrecision       6;

runTimeModifiable   yes;

adjustTimeStep      yes;

maxCo               0.5;
```

Table C-3 Example of a controlDict file used in this thesis

```
    ddtSchemes
{
    default                         Euler;
}

    gradSchemes
{
    default                         Gauss linear;
    grad(p)                         Gauss linear;
    grad(U)                         Gauss linear;
}

    divSchemes
{
    default                         none;
    div(phi,U)                      Gauss limitedLinearV 1;
    div(phi,k)                      Gauss linear;
    div(phi,omega)                  Gauss linear;
    div(phi,R)                      Gauss limitedLinear 1;
    div(R)                          Gauss linear;
    div(phi,nuTilda)                Gauss limitedLinear 1;
    div((nuEff*dev(grad(U).T())))   Gauss linear;
}

    laplacianSchemes
{
    default                         none;
    laplacian(nuEff,U)              Gauss linear corrected;
    laplacian((1|A(U)),p)           Gauss linear corrected;
    laplacian(DkEff,k)              Gauss linear corrected;
    laplacian(DomegaEff,omega)      Gauss linear corrected;
    laplacian(DREff,R)              Gauss linear corrected;
    laplacian(DnuTildaEff,nuTilda)  Gauss linear corrected;
}

    interpolationSchemes
{
    default                         linear;
    interpolate(U)                  linear;
}

    snGradSchemes
{
    default                         corrected;
}

    fluxRequired
{
    default                         no;
    p                               ;
}
```

Table C-4 Example of a fvSchemes file used in this thesis

fvSolutions

In the *fvSolutions* file, the solvers and tolerances are set for each variable (Martinez [2011]). The used *fvSolutions* file is given in table C-5.

In the file three main parts can be distinguished, i.e. `solvers`, `PIMPLE` and `relaxationFactors`. The solvers part specifies the method that is used for each dicretized equation, here `p`, `pFinal`, `U`, `UFinal`, `k` and `omega`. The available methods are shown in table C-6, in which the `PCG` method is used for symmetric matrices and the`PBiCG` for asymmetric matrices. The numerical methods will not be discussed in this thesis, they are merely mentioned in order to show that different methods are available. The preconditioner and smoother options can also be found in OpenFOAM Foundation [2012].

In OpenFOAM, the residual error is evaluated by substituting the current solution into the equation and taking the magnitude of the difference between the left and right hand sides (OpenFOAM Foundation [2012]). As already mentioned before, the solving of the equations is an iterative process and after each iteration the residual error is re-evaluated. In the *fvSolutions* file the tolerance and the relative tolerance are specified. The solvers stops if either of the following conditions are reaches:

- the residual error falls below the solver tolerance, `tolerance`;
- the ratio of the current to initial residuals falls below the solver relative tolerance, `relTol`;
- the number of iterations exceeds a maximum number of iterations

As mentioned before, the PIMPLE algorithm is based on evaluating some initial solutions and then correcting them. The number of corrections that are made are specified within the PIMPLE part of the *fvSolutions* file. The number of corrections of the inner and outer loops can be set with `nCorrectors` and `nOuterCorrectors` respectively. the `nNonOrthogonalCorrectors` keyword is used to correct for the influence of a non-orthogonal mesh. The values for `pRefValue` is used to specify the relative pressure at some point `pRefCell`. However the relative pressure is set to zero here.

The `relaxationFactors` part controls the under-relaxation. Under-relaxation is a technique that is used for improving the stability of computations (particularly in steady-state problems). This technique limits the amount which a variable can change in one iteration step. An under-relaxation factor is specified, which can vary from 0 (strong relaxation) to 1 (no relaxation). In this thesis no relaxation is used.

```
solvers
{
    p
    {
            solver                      GAMG;
            tolerance                   1e-06;
            relTol                      0.01;
            smoother                    GaussSeide1;
            cacheAgglomeration          true;
            nCellsInCoarsestLevel       10;
            agglomerator                faceAreaPair;
            mergeLevels                 1; }
    pFinal
    {
            solver                      GAMG;
            tolerance                   1e-06;
            relTol                      0;
            smoother                    GaussSeidel;
            cacheAgglomeration          true;
            nCellsInCoarsestLevel       10;
            agglomerator                faceAreaPair;
            mergeLevels                 1; }
    U
    {
            solver                      PBiCG;
            preconditioner              DILU;
            tolerance                   1e-05;
            relTol                      0.1; }
    UFinal
    {
            solver                      PBiCG;
            preconditioner              DILU;
            tolerance                   1e-05;
            relTol                      0; }
    k
    {
            solver                      PBiCG;
            preconditioner              DILU;
            tolerance                   1e-05;
            relTol                      0; }
    omega
    {
            solver                      PBiCG;
            preconditioner              DILU;
            tolerance                   1e-05;
            relTol                      0; }
}
PIMPLE
{
            nOuterCorrectors            3;
            nCorrectors                 3;
            nNonOrthogonalCorrectors    0;
            pRefCell                    0;
            pRefValue                   0; }
relaxationFactors
{
            U                           1;
            k                           1;
            omega                       1; }
```

Table C-5 Example of a fvSchemes file used in this thesis

Keyword OpenFOAM	Description
`PCG / PBiCG`	Preconditioned (bi-)conjugate gradient
`smoothSolver`	Solver using a smoother
`GAMG`	Generalised geometric-algebraic multi-grid
`diagonal`	Diagonal solver for explicit systems

Table C-6 Methods that can be specified under solvers in the fvSolutions file (from OpenFOAM Foundation [2012])

D Boundary Condition Set-up

In this appendix the set-up of the boundary conditions is explained. Fist, the numerical model with cyclic boundary conditions used to compare the equilibrium model conditions to the velocity and turbulence values specifically for the flume in which the measurements were performed. Running the OpenFOAM model with cyclic boundaries lead to the equilibrium solution for a large enough simulation time) . The model output for velocity, turbulent kinetic energy, turbulent viscosity and specific dissipation rate is be compared with both theoretical values as well as measurements.

Velocity

In figure D-1 the velocity profile obtained from a run of the flat model is shown. Also, the measurement points are plotted, together with the theoretical velocity profile (using the law of the wall from section 2.1).

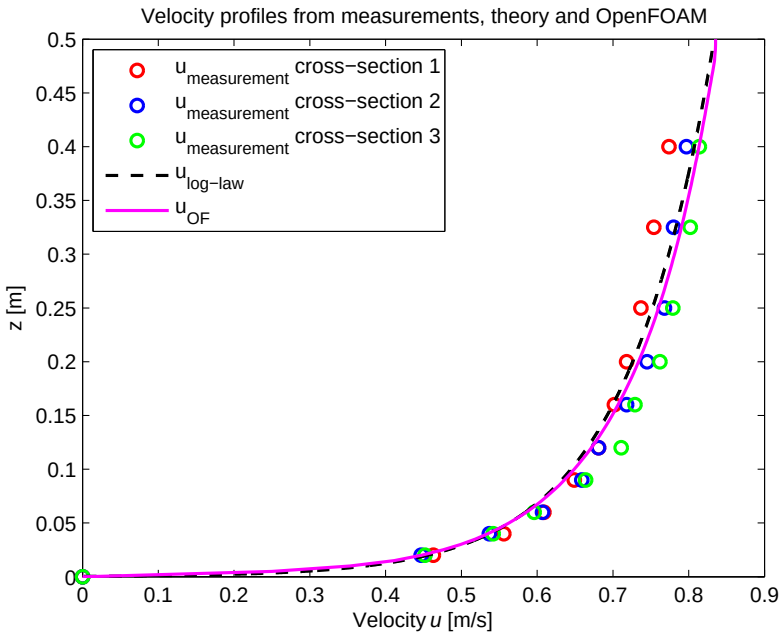

Figure D-1 Velocity from measurements (Jongeling et al. [2003]), the log-law and the cyclic OpenFOAM simulation

The velocity profile from OpenFOAM shows clear similarities with both the measurements as well as the theoretical velocity profile. The fact that the measured velocity profiles are different in each cross-section indicates that the flow might not be fully uniform in the flume. In Jongeling et al. [2003] it was stated that in the flume 3D effects were not totally negligible. The OpenFOAM model was in 2DV and therefore these effects are not included. This can explain the difference between the OpenFOAM equilibrium velocity and some of the measurements.

Turbulence properties

The turbulence is described in the output by the turbulent kinetic energy k, the specific dissipation rate ω and the turbulent viscosity ν_t and. In figure D-2 to D-4 the values of these quantities are shown. The two latter are only compared to the theory, since these were not measured. The theoretical profiles of the turbulent kinetic energy and the turbulent viscosity are obtained by using the relations for flow in equilibrium that were given in section 2.1. The specific dissipation

rate is subsequently derived by dividing k by ν_t ($\omega = k/\nu_t$, see Menter [1994]).

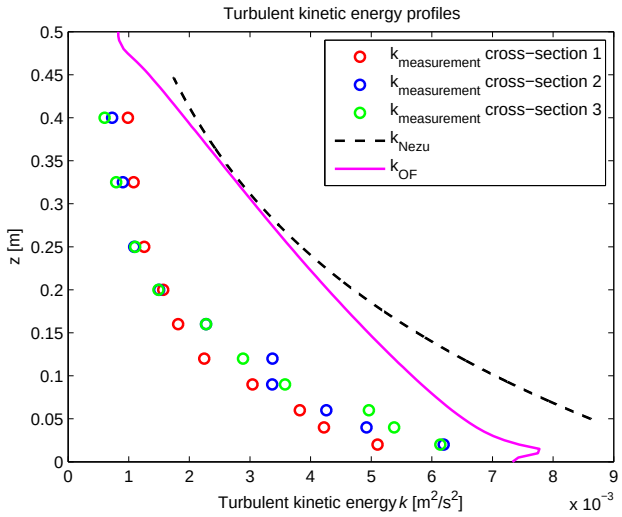

Figure D-2 Turbulent kinetic energy from measurements (Jongeling et al. [2003]), the empirical profile by Nezu [2005] and the cyclic OpenFOAM simulation

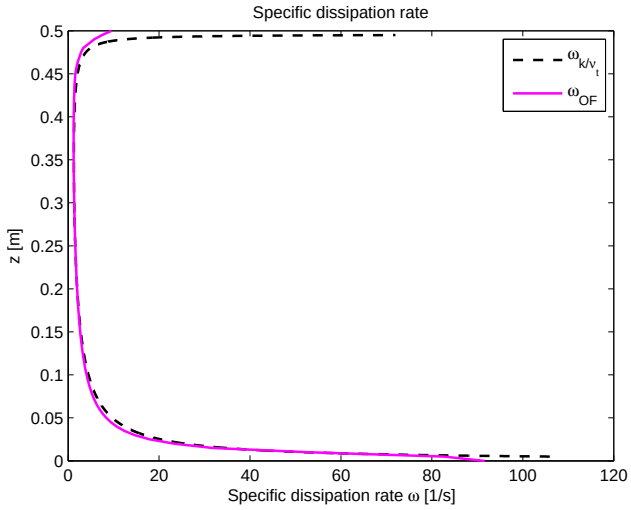

Figure D-3 Specific dissipation rate derived from k/ν_t and the cyclic OpenFOAM simulation

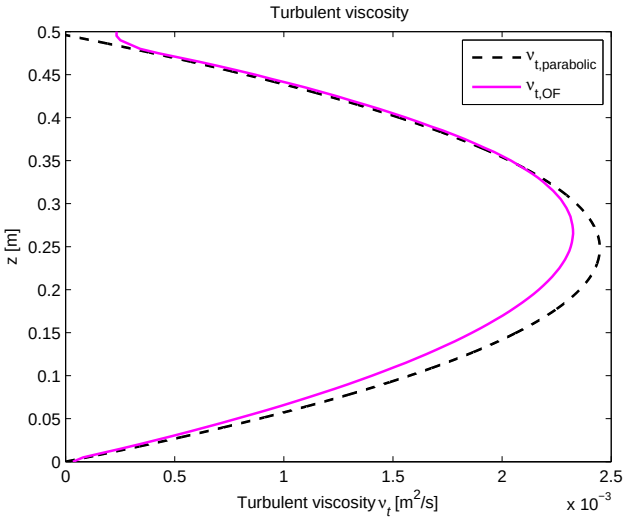

Figure D-4 Turbulent viscosity from the theoretical parabolic function and the cyclic OpenFOAM simulation

In the figures, it is clearly observable that the OpenFOAM output looks quite similar to the theoretical profiles. The turbulent kinetic energy measurements, however, deviates significantly from both OpenFOAM and theory. Again, the 3D effects can be identified as the cause of the deviation of the turbulent kinetic energy in the flume. This is also confirmed in Nezu [2005], in which it is stated that the 3D effects can occur in a channel when $B/h < 5$ which was the case in the measurements. Next to 3D effects, the flow can also just not be developed yet. In figure D-5 the development of the turbulent kinetic energy profile is given. It can be seen that the measured profile is not equal to any of the development stages. However, the steep gradient of the profile near the bottom looks like the more developed part, while the upper parts of the vertical more look like a more undeveloped part of the flow.

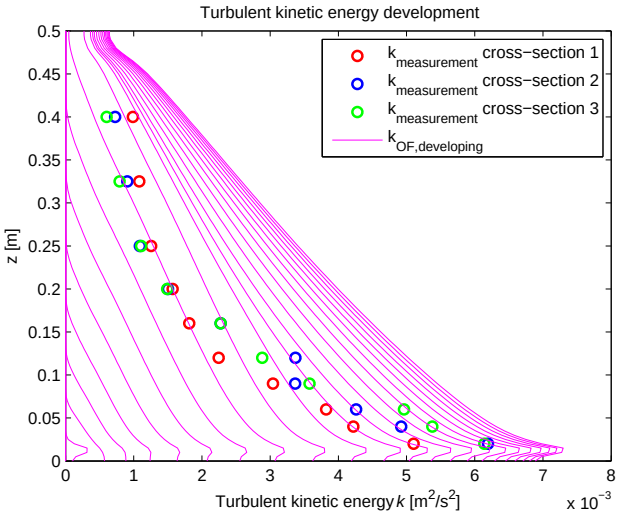

Figure D-5 Turbulent kinetic energy from measurements compared to the development in time from OpenFOAM

Instead of using the cyclic calculations as a boundary conditions, it is chosen to impose the measured profiles at the inlet boundary (Blackmore et al. [2011]. For the flat bed case, the measured velocity and turbulent kinetic energy profiles are imposed at the inlet boundary. The specific dissipation rate ω is calculated using the measured k and the theoretical ν_t in $\omega = k/\nu_t$.

Contrary to the flat bed case, the short sill and long sill case did not have measurements available at a location in front of the sill. However, the discharges in these configurations were different compared to the the flat bed experiment. The velocities for the short and long sill were then determined by the theoretical profiles of the log-law belonging to the discharge. Iit is realized that the turbulent kinetic energy also changes when the discharge is changed. However, the turbulent kinetic energy profiles of the flat bed simulation were used because this led to sufficiently accurate results.

E Mesh Generation

The generation of the mesh that is used in the numerical modelling is discussed in this appendix. The solution of a numerical simulation has to be independent of the mesh that is used (see chapter 3). However, considering the requirement that is imposed on the smallest cell near the bed, the definition of mesh independence is altered slightly to independent of the mesh provided that the restrictive first cell requirements are fulfilled.

The following aspects are taken into account:

- **Convergence:** This requirement is fulfilled when the (steady state) solution satisfies the following conditions:
  1. The residual error has to be reduced to an acceptable value ("acceptable" differs per case and should be set at own judgement)
  2. A steady state solution has to be reached
  3. The imbalances (or spurious oscillations) in the domain should be less than 1%
- **Mesh independence:** The solution should be independent of the mesh provided that the restrictive first cell requirements are fulfilled
- **Height of the first cell center:** In section 3.1.3 it was already mentioned that the height of the first cell center has to fulfill $z > 0.2k_s$. Also, z^+ has to remain below 300 to stay within the log-law layer.
- **Cell height expansion factor:** To reduce computation times, the cell height can be gradually expanded. The ratio between two consecutive cell heights has to stay within certain limits, although there are no specific requirements for this.
- **Aspect ratio:** To reduce computation times, the length of the cell in streamwise direction can be increased (since in this direction the gradients are smaller). Martinez [2011] found in his thesis that the maximum aspect ratio at which his $k-\varepsilon$ model could still model the right solution was 2500. Jacobsen [2011] found that for his description of waves a surface aspect ratio of 1 was required.

The mesh will be generated using the `blockMesh` utility in OpenFOAM. First, the mesh for the flatbed simulation is generated since this is a theoretically well known scenario in which the results can be calculated beforehand analytically. The mesh will be generated by taking the following steps:

1. Calculate the minimal height of the first cell
2. Reduce the number of cells in the vertical using cell height expansions
3. Determine aspect ratio based on different surface aspect ratios

The height of the first cell has to fulfill the requirement that $z_{c.min} > 0.2 \cdot k_s$ and $z^+_{c.max} > 300$. In all of the experiments a d_{n50} of 0.0062 m was used. The value of k_s is usually taken as 1 to 3 times d_{n50} (Schiereck [2001]). For now, a value of $2 \cdot d_{n50}$ is applied. In table E-1 the governing calculated variables are given. Here, z_{1c} is the height of the cell center, while z_1 is used here as the height of the top of the first cells.

Variable	Value
$\langle \overline{u} \rangle_h$	0.718 m/s
d_{dn50}	0.0062 m
k_s	0.0124 m
u_*	0.0465 m/s
$z_{1c,min}$	0.00248
z_{min}	0.00496
$z_{1c,max}$	0.00645
z_{max}	0.01290

Table E-1 Calculation height of the first cell

Based on this values, the cell heights in table E-2 have been investigated.

Number of cells N	z_1
120	0.00410
100	0.00500
80	0.006250
60	0.00833
30	0.01667

Table E-2 Investigated number of cells in the z-direction

Using three meshes based on table E-2 and an aspect ratio of 1 at the surface, the simulations can be performed. The simulations were performed using the `pimpleBodyFoam` solver in OpenFOAM. This solver is identical to the `pimpleFoam` solver described in appendix C except that in the `pimpleBodyFoam` solver a body force is added to enable the use of cyclic boundary conditions by introducing a driving force. From equilibrium calculations it can be found that `bodyForce` = u_*^2/h, which in this case was 0.0045 m/s^2. The boundary conditions that where used for each of the domain boundaries are give in table E-3.

	Boundary Condition				
Boundary	`U`	`k`	`omega`	`p`	`nut`
Inlet	`Cyclic`	`Cyclic`	`Cyclic`	`Cyclic`	`Cyclic`
Outlet	`Cyclic`	`Cyclic`	`Cyclic`	`Cyclic`	`Cyclic`
Bed	`Uniform Value (0 0 0)`	`zeroGradient`	`omega-WallFunction`	`nutRough WallFunction Ks = 0.0124 Cs=0.5`	`zeroGradient`
Surface	`slip`	`zeroGradient`	`fixedValue 9.67`	`zeroGradient`	`zeroGradient`
Side Walls	`empty`	`empty`	`empty`	`empty`	`empty`

Table E-3 Boundary conditions for the flat bed case

To check for convergence the velocity at a height of 0.4 m above the bed is plotted against the time, which can be seen in figure E-1. It can be seen that most of the computations converge to the same value except for when $N = 120$ and $N = 30$ are used. In these cases the requirement of the first cell height is not fulfilled, resulting in an error in the reached velocity. Considering the above, and the computation times, it is chosen to use $N = 60$ and $z_1 = 0.00833$.

Because the cyclic boundaries are going to be replaced with inflow and outflow boundaries in a later stadium, the number of cells increases significantly. To reduce computation times, it is therefore chosen to let the cell height increase gradually in upward vertical direction. In the *blockMeshDict* file the number of cells and the expansion factor can be specified. The expansion

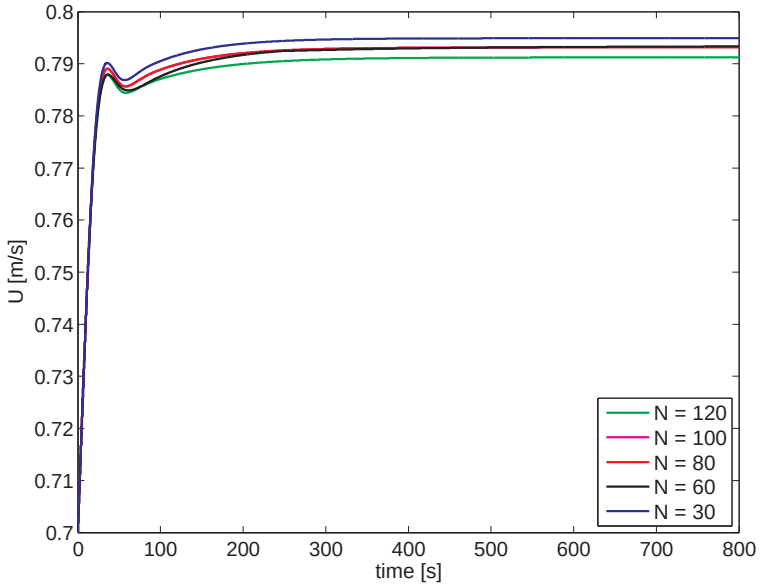

Figure E-1 The velocity u at a certain z-position plotted against the time

factor is the ratio between the first and last cell height $\Delta z_h/\Delta z_1$. The expressions used in OpenFOAM can be found in equation E-1

$$\mathrm{dz}(n) = e^{bn} \tag{E-1a}$$

$$\mathrm{dz}(1) = e^{b} \tag{E-1b}$$

$$a = \frac{d(1-e^{b})}{e^{b}-e^{(N+1)b}} \tag{E-1c}$$

$$b = \frac{\ln E}{(N-1)} \tag{E-1d}$$

with:

$dz(n)$	the cell height of cell n [m]
n	the number of the cell [-]
N	the total number of cells [-]
h	the water depth [m]

The simulations are executed using the number of cells given in table E-4. The output of `U` and `k` for the simulations are shown in figures E-2a and E-2b, respectively.

Height smallest cell [m] Δz [m]	water depth h [m]	Number of cells N	Expansion rate E
0.00833	0.495	50	1.424
0.00833	0.495	40	2.139
0.00833	0.495	30	3.487
0.00833	0.495	20	6.562

Table E-4 Expansion rate for a given number of cells

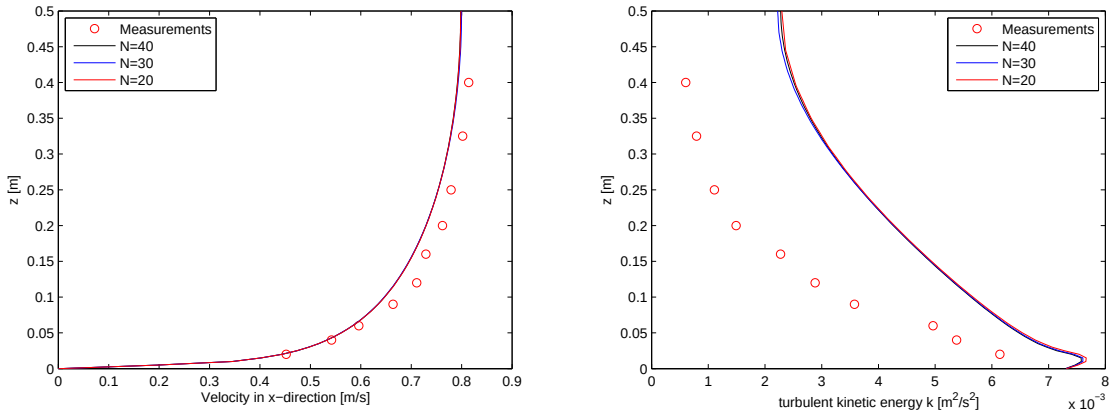

(a) Velocity *(b) Turbulent kinetic energy*

Figure E-2 Comparison OpenFOAM output for different number of cells N

The use the expansion of the mesh generates almost exactly the some solutions. It is chosen to use a 50 cell mesh with an expansion factor of 1.42. Now, the sensitivity of the aspect ratio will be investigated. The aspect ratio from Jacobsen [2011] of 1 will be increased to 10 and 100 respectively. The used values for Δx can be found in table E-5.The results are shown in figures E-3a and E-3b for U and k respectively.

Δx	Aspect ratio surface ($\Delta x/\Delta z$)	Aspect ratio bed ($\Delta x/\Delta z$)
0.029	1:1	3.487:1
0.29	10:1	34.87:1
2.9	100:1	348.7:1

Table E-5 Aspect ratios

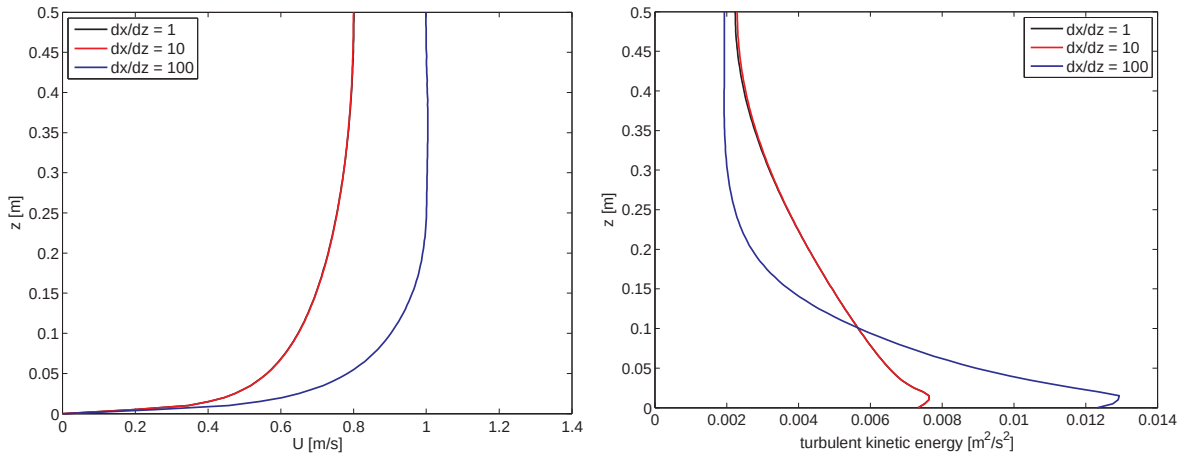

(a) Velocity *(b) Turbulent kinetic energy*

Figure E-3 Comparison OpenFOAM output for different aspect ratios

It is clear that the simulations with a surface aspect ratio of 1 and 10 show almost identical results. The surface aspect ratio of 100 does not give a correct solution at all. More test were executed and it was concluded that a surface aspect ratio up to approximately 40 still gave the same converged solutions. Summarized, the following settings are used in the mesh generation:

Variable	Value
z_1	0.0083 m
N	50
z_1/z_n	1.42
$(\Delta x/\Delta z)_{max}$	40

The mesh with the characteristics above is generated for the flat bed simulation. For the other geometries, the same values is used for the smallest first grid cell and the number of cells in the vertical. However, the surface aspect ratio is reduced from 10 away from the sill to 1 in the vicinity of the sill.

F Correlation Analysis

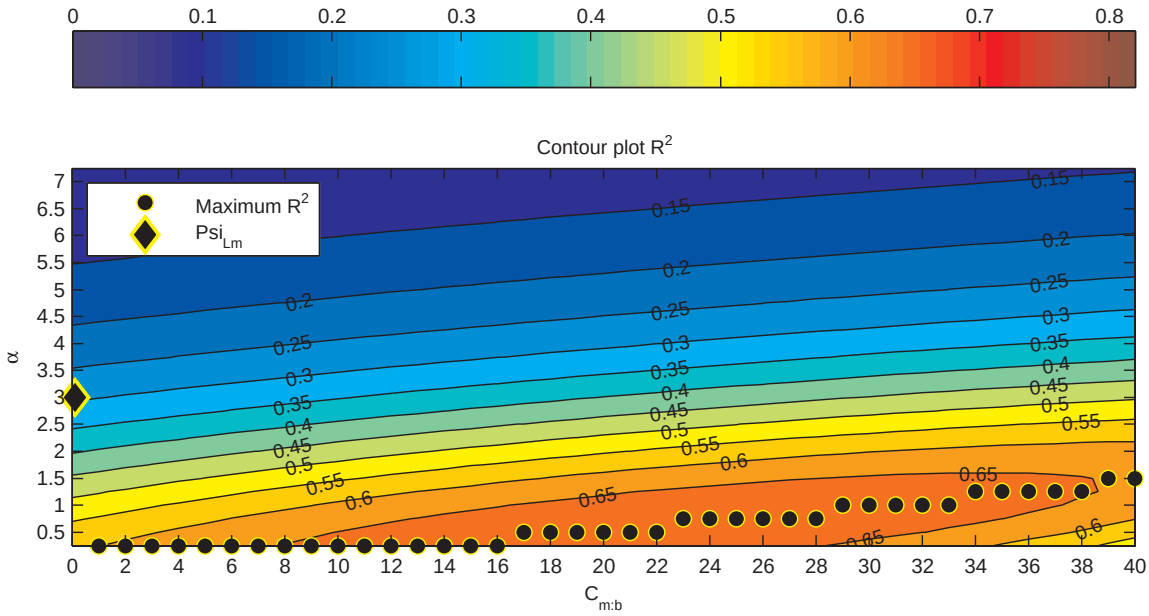

Figure F-1 $h_a = 1.0 \cdot d_{n50}$ *resulting in a maximum* $R^2 = 0.6856$ *for* $\alpha = 0.50$ *and* $C_{m:b} = 24.0$

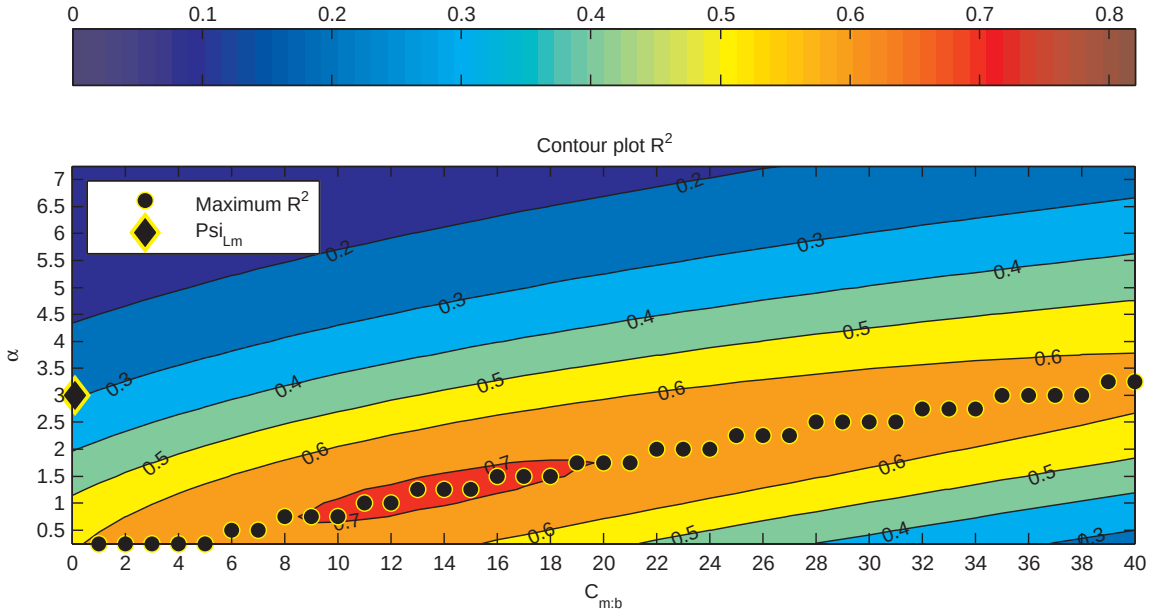

Figure F-2 $h_a = 2.0 \cdot d_{n50}$ *resulting in a maximum* $R^2 = 0.7093$ *for* $\alpha = 1.00$ *and* $C_{m:b} = 14.0$

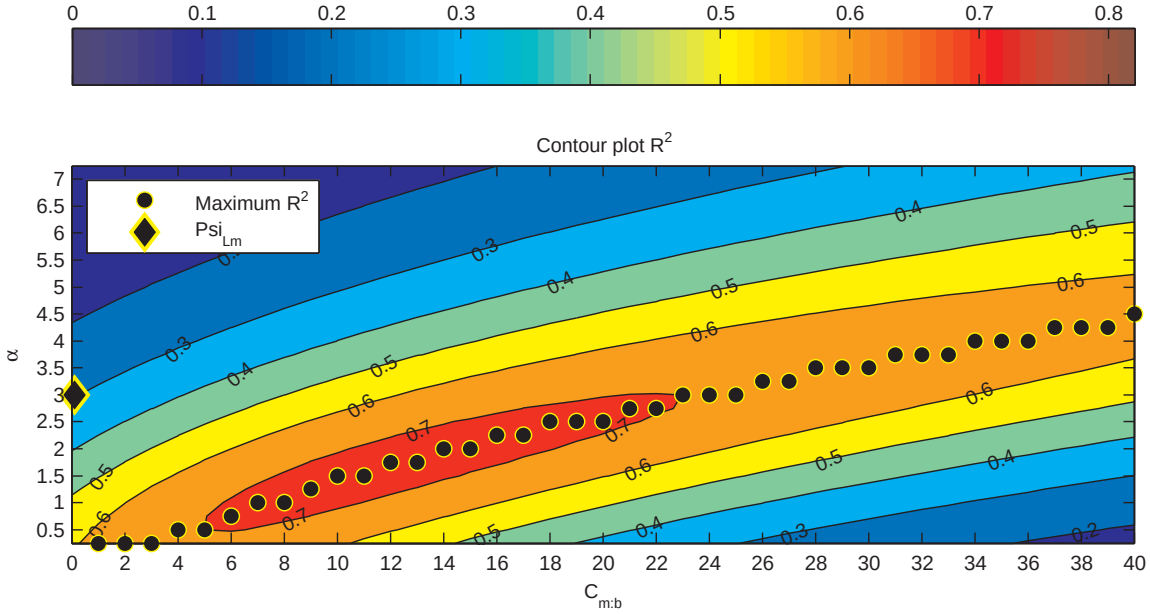

Figure F-3 $h_a = 3.0 \cdot d_{n50}$ *resulting in a maximum* $R^2 = 0.7274$ *for* $\alpha = 1.50$ *and* $C_{m:b} = 12.0$

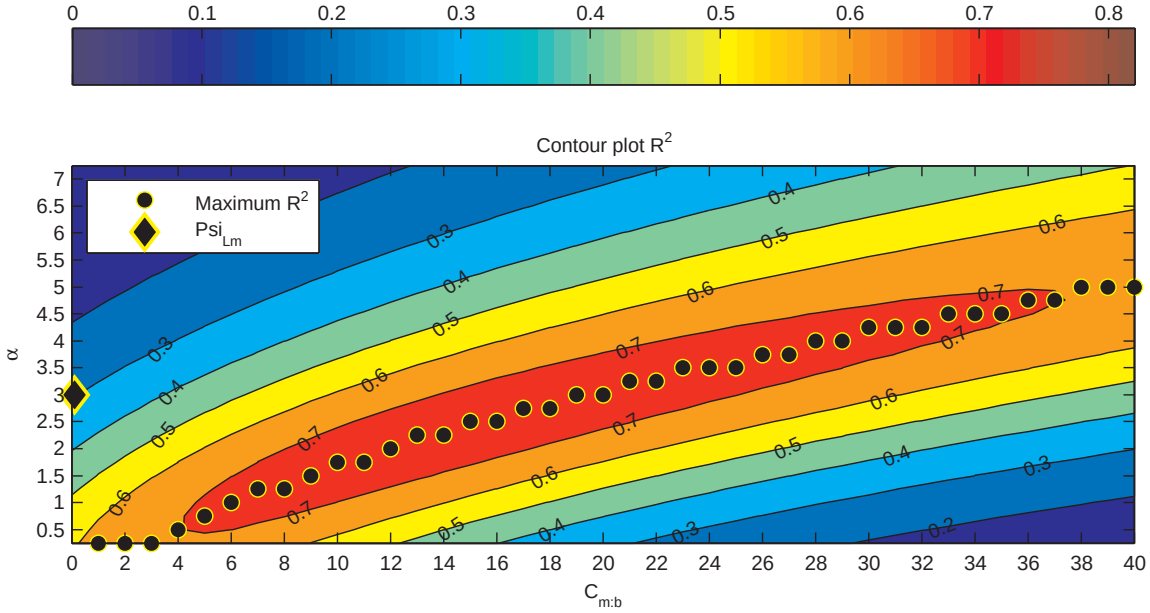

Figure F-4 $h_a = 4.0 \cdot d_{n50}$ *resulting in a maximum* $R^2 = 0.7537$ *for* $\alpha = 2.00$ *and* $C_{m:b} = 14.00$

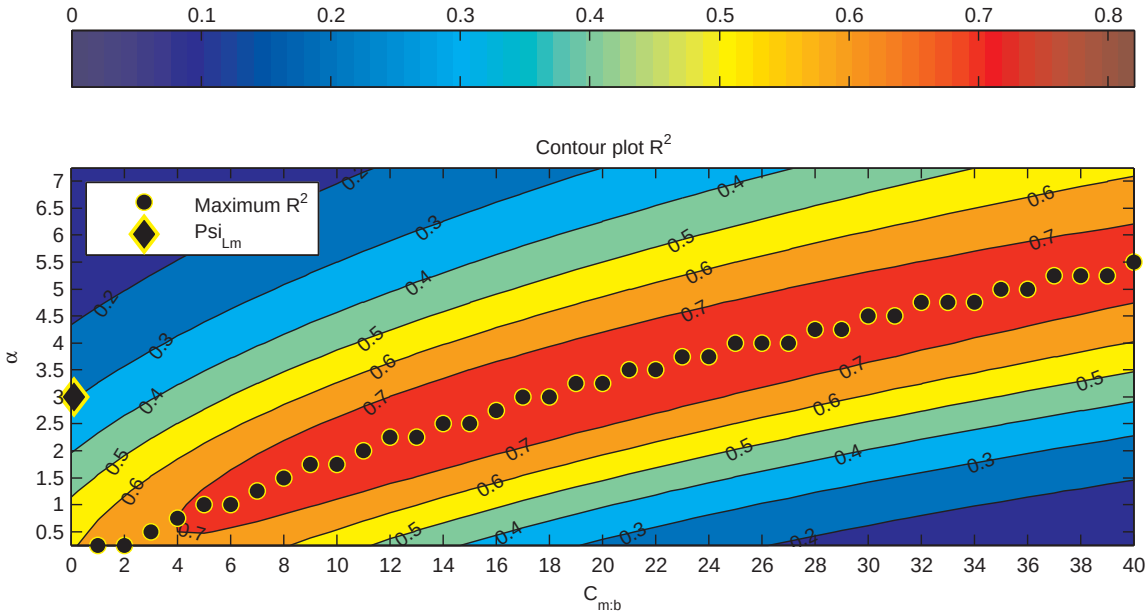

Figure F-5 $h_a = 5.0 \cdot d_{n50}$ *resulting in a maximum* $R^2 =$ *for* $\alpha = 2.75$ *and* $C_{m:b} = 18.0$

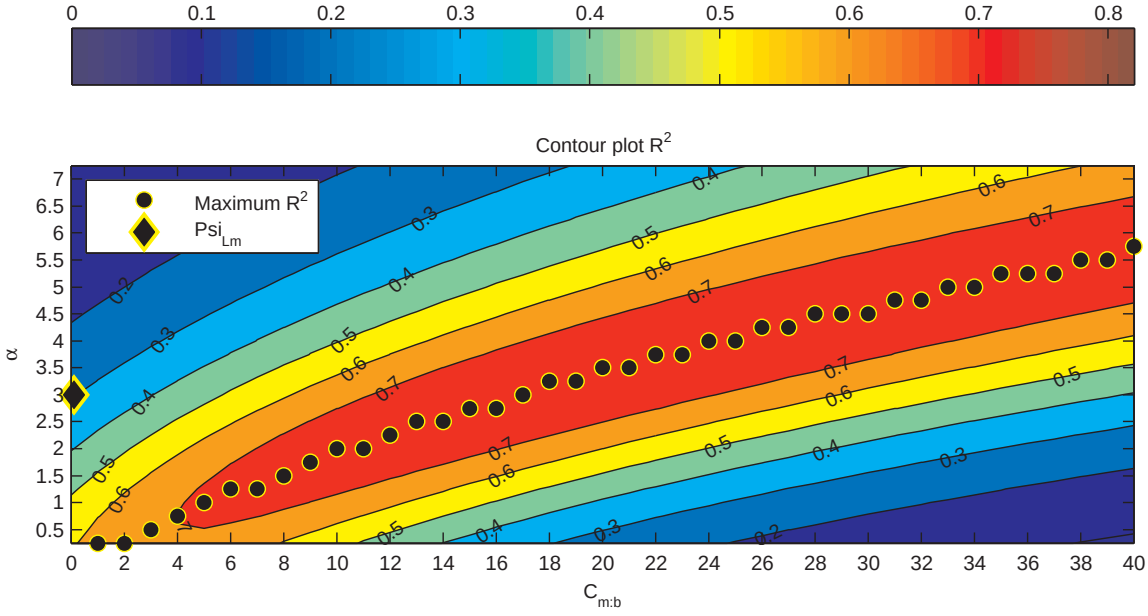

Figure F-6 $h_a = 6.0 \cdot d_{n50}$ *resulting in a maximum* $R^2 = 0.7886$ *for* $\alpha = 3.00$ *and* $C_{m:b} = 19.0$

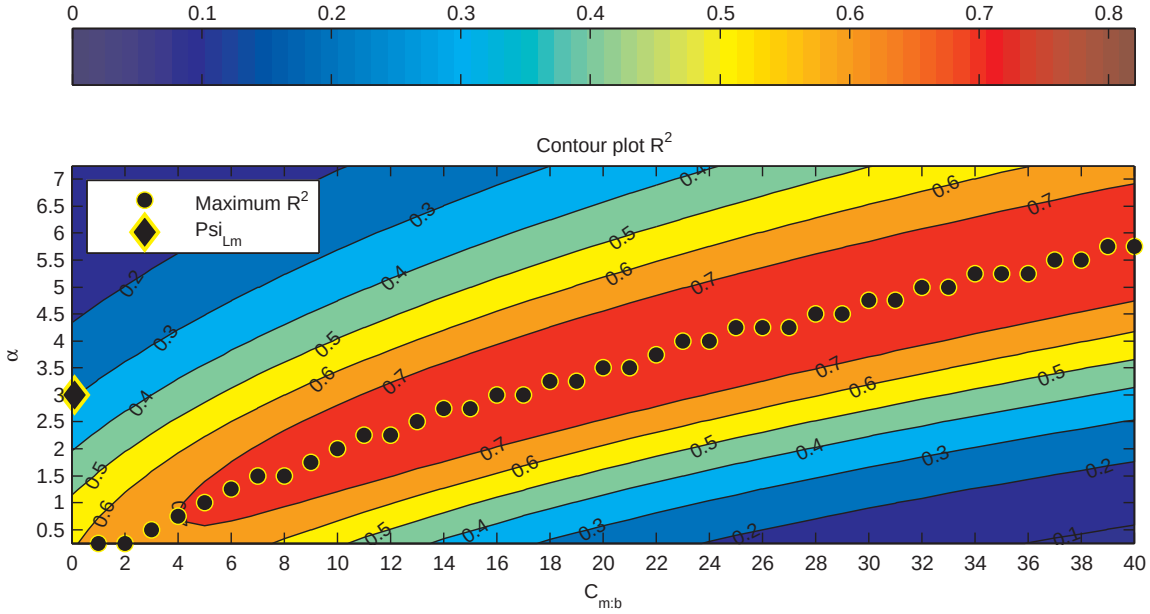

Figure F-7 $h_a = 7.0 \cdot d_{n50}$ *resulting in a maximum* $R^2 = 0.7967$ *for* $\alpha = 3.50$ *and* $C_{m:b} = 22.0$

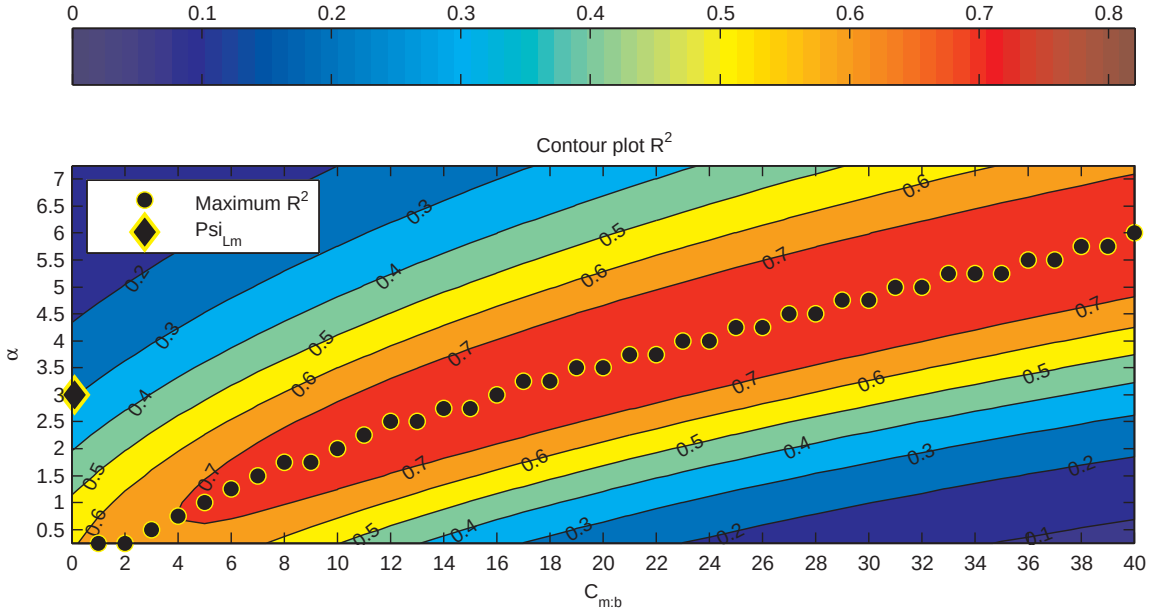

Figure F-8 $h_a = 8.0 \cdot d_{n50}$ *resulting in a maximum* $R^2 = 0.7998$ *for* $\alpha = 3.75$ *and* $C_{m:b} = 23.0$

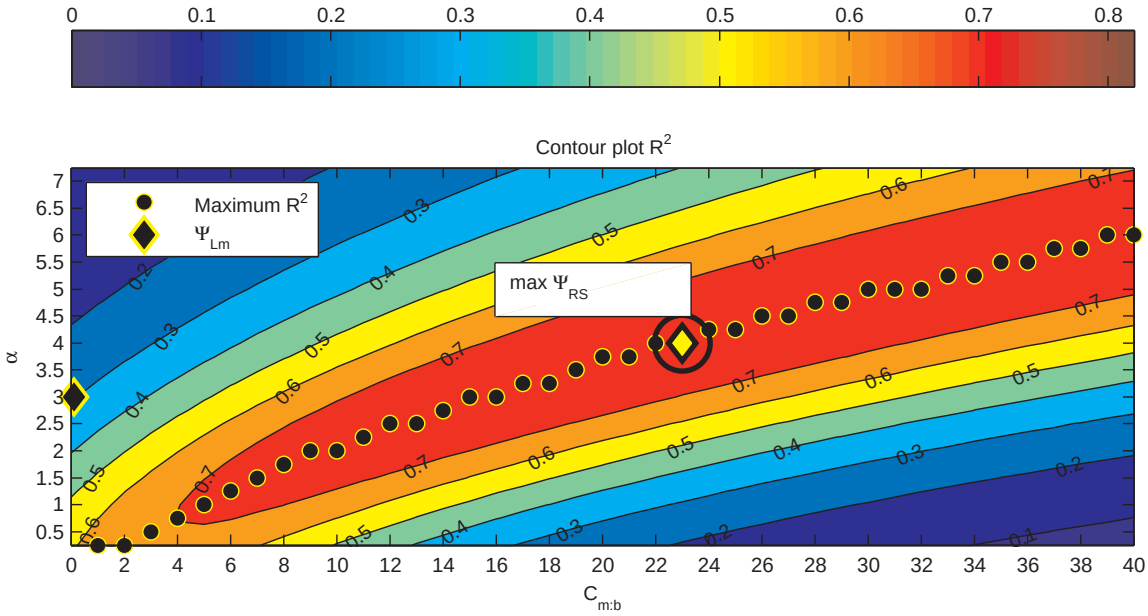

Figure F-9 $h_a = 9.0 \cdot d_{n50}$ *resulting in a maximum* $R^2 = 0.8003$ *for* $\alpha = 3.75$ *and* $C_{m:b} = 23.0$

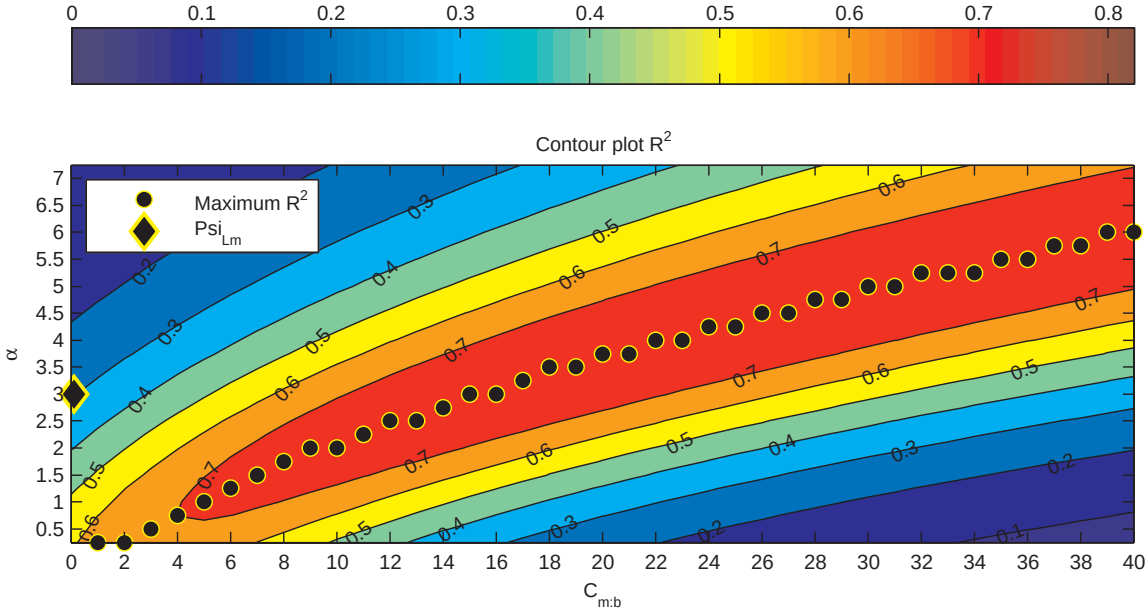

Figure F-10 $h_a = 10.0 \cdot d_{n50}$ *resulting in a maximum* $R^2 = 0.7969$ *for* $\alpha = 3.75$ *and* $C_{m:b} = 23.0$

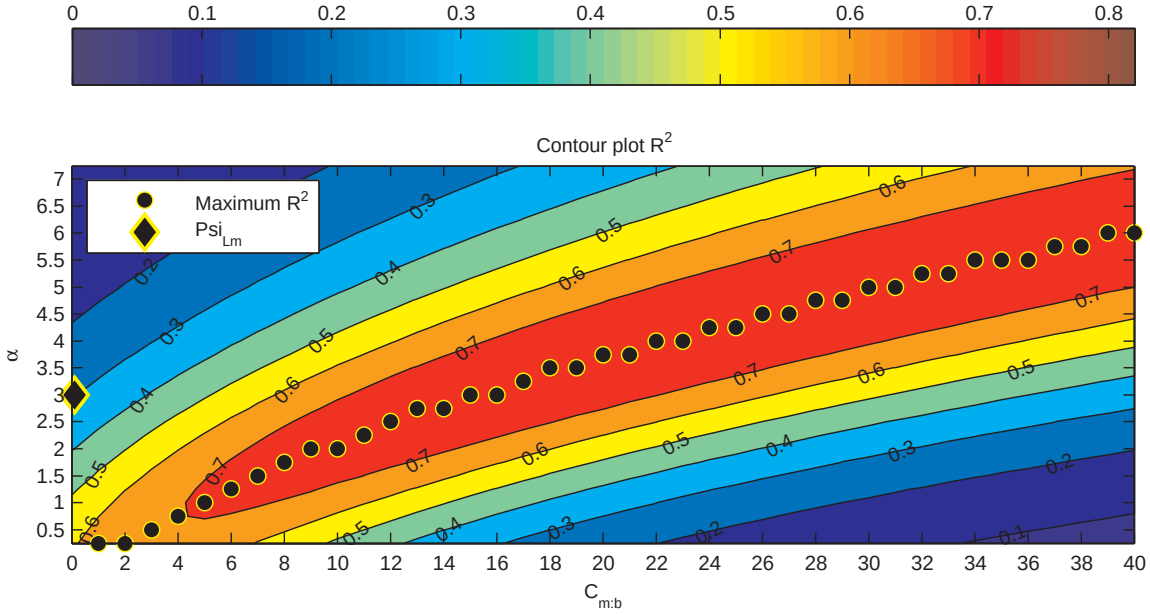

Figure F-11 $h_a = 30.0 \cdot d_{n50}$ *resulting in a maximum* $R^2 = 0.7905$ *for* $\alpha = 3.75$ *and* $C_{m;b} = 22.0$

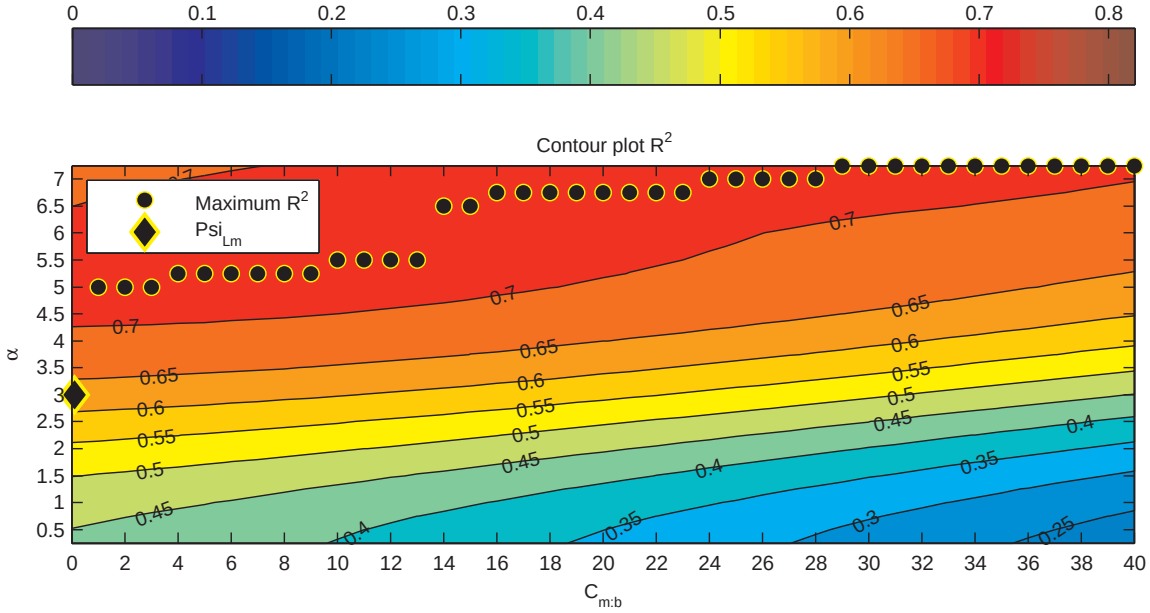

Figure F-12 $h_a = 30.0 \cdot d_{n50}$ *resulting in a maximum* $R^2 = 0.7127$ *for* $\alpha = 5.0$ *and* $C_{m;b} = 6.0$

List of Figures

List of Tables

Bibliography

Aguerre, H. J., Damian, S., Giminez, J. M., and Nigro, N. M. (2013). Modeling of compressible fluid problems with openfoam using dynamic mesh technology. *Mecánica Computacional*, 32:955 – 1011.

Alfrink, B. J. and van Rijn, L. C. (1983). Two-equation turbulence model for flow in trenches. *Journal of Hydraulic Division*, 109:941 – 958.

ANSYS, Inc. (2011). *ANSYS FLUENT User's Guide*. ANSYS, Inc., 275 Technology Drive, Canonsburg, PA 15317, 14.0 edition.

Bardina, J. E., Huang, P. G., and Coakley, T. (1997). Turbulence modelling validation. *AIAA Paper*, 97:2121.

Battjes, J. A. (2002). *Lecture notes CT3310: Open-Channel Flow*. Delft University of Technology.

Blackmore, T., Batten, W. M. J., Harrison, M. E., and Bahaj, A. S. (2011). The sensitivity of actuator-disc rans simulations to turbulence length scale assumptions. Proceedings Ninth European Wave and Tidal Energy Conference.

Buffin-Bélanger, T., Roy, A. G., and Kirkbride, A. D. (2000). On large-scale flow structures in a gravel-bed river. *Geomorphology*, 32:417–435.

Coles, D. (1956). The law of the wake in turbulent boundary layers. *J. Fluid Mech.*, 1:191–226.

De Gunst, M. (1999). Stone stability in a turbulent flow behind a step. Master's thesis, Delft University of Technology. In Dutch.

Dean, R. G. and Dalrymple, R. A. (1991.). *Water wave mechanics for engineers and scientist. .* Singapore: World Scientific Publishing Co. Pte. Ltd.

Dessens, M. (2004). The influence of flow acceleration on stone stability. Master's thesis, Delft University of Technology.

DHL (1969). Begin van beweging van bodemmateriaal. Technical report. report Q635.

Ferziger, J. and Peric, M. (1999). *Computational Methods for Fluid Dynamics*. Springer.

Grass, A. (1971). Structural features of turbulent flow over smooth and rough boundaries. *Journal of Fluid Mechanics*, 50(2):233–255.

Grotjans, H. and Menter, F. R. (1998). Wall functions for industrial applications. *Computational Fluid Dynamics*, 1:1112–1117. ECCOMAS, John Wiley & Sons.

Higuera, P., Lara, J. L., and Losada, I. (2013). Realistic wave generation and active wave absorption for navier-stokes models application to openfoamő. *Coastal Engineering*, 71:102 – 118.

Hinze, J. O. (1975). *Turbulence*. McGraw-Hill.

Hoan, N. T. (2008). *Stone Stability Under Non-uniform Flow*. PhD thesis, Delft Univerisity of Technology.

Hofland, B. (2005). *Rock & Roll; Turbulence-induced damage to granular bed protections*. PhD thesis, Delft University of Technology.

Hoohlo, C. (1994). *A Numerical and Experimental Study of Open-Channel Flow in a Pipe of Circular Cross-SectionW ith a Flat Bed*. PhD thesis, Newcastle University, Newcastle upon Tyne.

Huijsmans, M. A. (2006). The influence of flow acceleration on the stability of stones. Master's thesis, Delft University of Technology.

Izbash, S. V. (1935). Constructions of dams by dumping of stone in running water. Moscow, Leningrad.

Jacobsen, N. G. (2011). *A Full Hydro- and Morphodynamic Description of Breaker Bar Development*. PhD thesis, DTU Mechanical Engineering.

Jodar, L., Acedo, L., Cortés, J. C., and Pedroche, F. (2012). *Modelling for Engineering & Humar Behaviour*. Universidad Politecnica de Valencia.

Jongeling, T. H. G., Blom, A., Jagers, H. R. A., Stolker, C., and Verheij, H. J. (2003). Design method granular protections. Technical report, WL|Delft Hydraulics. In Dutch.

Jongeling, T. H. G., Jagers, H. R. A., and Stolker, C. (2006). Design of granular bed protections using a RANS 3D-flow model. ISSMGE Proc. 3rd Int. Conf. On Scour and Erosion, Amsterdam. 150-151.

Keulegan, G. H. (1938). Laws of turbulent flows in open channel flow. *Journal of Research of the National Bureau of Standards*, 21:707–741.

Liu, X. and Garcia, M. H. (2008). Three-dimensional numerical model with free water surface and mesh deformation for local sediment scour. *Journal of Waterway, Port, Coastal and Ocean Engineering*, 2003.

Martinez, B. (2011). Wind resource in complex terrain with openfoam. Master's thesis, Technical University of Denmark.

Maxey, M. R. and Riley, J. J. (1983). Equation of motion for a small rigid sphere in a nonuniform flow. *Physics of Fluids*, 26(4):203–207.

Menter, F. (1994). Two-equation eddy viscosity turbulence models for engineering applications. *AIAA Journal*, 32:1598–1605.

Menter, F. and Esch, T. (2001). Elements of industrial heat transfer predictions. *16th Brazilian Congress of Mechanical Engineering (COBEM)*, pages 26 – 30. Uberlandia, Brazil.

Meselhe, E. A. and Sotiropoulos, F. (2000). Three-dimensional numerical model for open-channels with free-surfaee variations. *Journal of Hydraulic Research*, 38(2):115 – 121.

Meyer-Peter, E. and Muller, R. (1948). Formulas for bed-load transport. In *Proceedings of the 2nd Meeting of the International Association for Hydraulic Structures Research*, pages 39–64. Int. Assoc. Hydraul. Res.

Morison, J. R., O'Brian, M. P., Johnson, J., and Schaaf, S. A. (1950). The forceexerted by surface waves on piles. *Petrol. Trans. AIME*, 189:149–154.

Mosselman, E. & Akkerman, G. J. (1998). Low-mobility transport of coursegrained material. technical report q2395.40. Technical report, WL|Delft Hydraulics.

Nezu, I. (1977). *Turbulent structures in open-channel flow*. PhD thesis, Kyoto University, Japan.

Nezu, I. (2005). Open-channel flow turbulence and its research prospect in the 21st century. *J. Hydraull. Eng*, 131:229–246.

Nezu, I. and Rodi, W. (1986). Open-channel measurements with a laser doppler anemometer. *J. Hydraull. Eng*, 112(5):335–355.

Nikuradse, J. (1933). Strömungsgesetze in rauhen rohren. Forschungsheft 361, Verein Deutscher Ingenieure.

OpenFOAM Foundation (2012). *OpenFOAM: The Open Source CFD Tool User Guide*, version 2.1.1 edition.

Paintal, A. S. (1971). Concept of critical shear stress in loose boundary open channels. *Journal of Hydraulic Research*, 9:91Ű113.

Parneix, S., Behnia, M., and Durbin, P. A. (1999). Predictions of turbulent heat transfer in an axisymmetric jet impinging on a heated pedestal. *Journal of Heat Transfer*, 121:43.

Pietrzak, J. (2011). *Reader for CT5317: An Introduction to Oceanography for Civil and Offshore Engineers*. Delft University of Technology.

Prandtl, L. (1925). Bericht über untersuchungen zur ausgebildeten turbulenz. *Zeitschrift für Angewandte Mathematik und Mechanik.*, 5(1):136–139.

Radecke, H. V. and Schulz-DuBois, E. O. (1988). Linear response of fluctuating forces to turbulent velocity components. *Applications of Laser Anemometry to Fluid Mechanics.*

Raupach, R. M. (1981). Conditional statistics of reynolds stress in rough-wall and smooth-wall turbulent boundary layers. *Journal of Fluid Mechanics*, 108:363–382.

Reynolds, O. (1883). An experimental investigation of the circumstances which determine whether the motion of water in parallel channels shall be direct or sinuous and of the law of resistance in parallel channels. *Philos. Trans. R. Soc*, 174:935Ű82.

Rodi, W. (1980). *Turbulence Models And Their Application in Hydraulics*. Balkema, Rotterdam, The Netherlands.

Schewe, G. (1983). On the structure and resolution of wall-pressure fluctuations associated with turbulent boundary-layer flow. *Journal of Fluid Mechanics*, 134:311–328.

Schiereck, G. J. (2001). *Introduction to bed, bank and shore protection*. VSSD, Delft.

Shi, J., Thomas, T. G., and Williams, J. J. R. (2000). Free-surface effects in open channel flow at moderate froude and reynold's numbers. *Journal of Hydraulic Research*, 38(6):465 – 474.

Shields, A. (1936). Anwendung der Aenhnlichkeitsmechanik und der Turbulenzforschung auf die Geschiebebewegung. Berlin, Germany.

Song, T. and Chiew, Y. M. (2001). Turbulence measurement in non-uniform open-channel flow using acoustic doppler velocimeter (adv). *Journal of Engineering Mechanics*, 127:219–232.

Tennekes, H. and Lumley, J. L. (1972). *A First Course in Turbulence*.

Tromp, M. (2004). The influence that fluid accelerations have on the threshold of motion. Master's thesis, Delft University of Technology.

TU Delft (2006). *Lecture Notes CIE4130: Probality in Civil Engineering*. TU Delft.

Uijttewaal, W. S. J. (2011). *Turbulence in Hydraulics*. TU Delft, Delft.

Uittenbogaard, R., Hoffmans, G., and Akkerman, G. (1998). Turbulence schematization for stone stability assessment. *Tech. rept. Q2395.30.* WL|Delft Hydraulics Delft.

Van den Bos, J. P. (2006). Design of granular near-bed structures in waves and currents. Master's thesis, Delft University of Technology.

Van Driest, E. R. (1956). On turbulent flow near a wall. *J. Aeronaut. Sci.*, 23(11):1007–1011.

van Rijn, L. C. (1984). Sediment transport, part i: bed load transport. *Journal of Hydaulic Engineering*, 110:1431Ű1456.

Villanueva, P. A. M. (2010). Toward the validation of depth-averaged, steady-state simulations of fluvial flows using three-dimensional steady-state, rans turbulence models. Master's thesis, Utah State University.

Vuik, C., van Beek, P., Vermolen, F., and van Kan, J. (2006). *Numerieke Methoden voor Differentiaalvergelijkingen*. VSSD, Leeghwaterstraat 42, 2826 CA Delft, The Netherlands, 1st edition.

Wilcox, D. (1993). *Turbulence Modeling for CFD*. DCW Industrics, Inc., La Canada, CA.

www.engwonders.byethost9.com. Reclaiming the zuiderzee.

Zijlema, M. (2012). *Computational modelling of flow and transport*. Delft University of Technology.